Statistical Muon Tracking: A Study of Cosmic Backgrounds in the PROSPECT Experiment

by

Austin Woolverton

A thesis
presented to the University of Waterloo
in fulfillment of the
thesis requirement for the degree of
Masters of Science
in
Physics (Quantum Information)

Waterloo, Ontario, Canada, 2021

Author's Declaration

This thesis consists of material all of which I authored or co-authored: see Statement of Contributions included in the thesis. This is a true copy of the thesis, including any required final revisions, as accepted by my examiners.

I understand that my thesis may be made electronically available to the public.

Statement of Contributions

This thesis was written by Austin Woolverton under the supervision of Dr. Dmitry Pushin at the University of Waterloo. Austin Woolverton was the sole author of chapters 5 and 7 as well as appendix B of this thesis. Chapters 1, 2, 3, and 7 were not intended for publication. This thesis, however, contains the published research of the PROSPECT collaboration including the collaborative effort of its previous members. It contains comparisons to analyses performed by other collaborators as well as researchers in similar disciplines. The exceptions to sole authorship are as follows:

Research presented in Chapter 1

Chapter 1 begins by summarizing the historical advances of neutrino physics that lead to the development of modern reactor experiments. It illustrates two experimental anomalies that the PROSPECT collaboration are attempting to resolve. The figure from the Daya Bay collaboration [1] describes the reactor flux anomaly, and the figures describing the spectrum anomaly were created by the RENO [2] and Daya Bay [3] collaborations.

Research presented in Chapter 2

The PROSPECT collaboration is a diverse group of researches from around the world that each contributed to the final spectrum result. The experiment operated from March to October of 2018, and the final spectrum and oscillation results are published in [4]. It was Austin Woolverton's responsibility to investigate possible cosmic background events that the vetoing and spectrum subtraction routines may have ignored. He used his muon tracking program to validate the background scaling performance during nonuniform experimental conditions.

Austin Woolverton wrote this chapter with the intention to succinctly describe the experiment. Its geometry was described to motivate the design and performance of his muon tracking program. This chapter contains a schematic of PROSPECT's inverse beta decay search strategy that was commissioned by Dr. David Jaffe for the 2018 APS conference [5]. The chemical composition of the scintillators, as well as the neutron capture properties, were taken from Andriamirado [6] and Adam Hansell's PhD dissertation [7]. This chapter also contains diagrams of the PROSPECT shielding, scintillators, and photomultiplying tubes taken from PROSPECT's instrumental publication [8]. This chapter concludes by summarizing the results of the primary spectrum analysis described in [4].

Research presented in Chapter 3

Chapter 3 contains a summary of the physical properties of the muon as they travel through the atmosphere. It also contains information about the different muon interaction mechanisms that might occur inside the PROSPECT detector. These details were provided by the Particle Data Group [9] as well as the report by Measday [10]. The figure describing the air shower was provided by the University of Adelaide [11].

This chapter also contains measurements of the muon rate and cosmic neutron yield from other experiments such as Daya Bay [12, 13], Double Chooz [14], and the China JinPing underground Laboratory [15]. Austin Woolverton used these results to hypothesize the muon neutron yield that should be observed at Earth's surface. He validated this hypothesis in chapter 6. The neutron yield produced through muon radioisotope decays, hypothesized by Dr. David Jaffe [16], could not be verified.

Research presented in Chapter 4

Chapter 4 contains a discussion of the simulation pipeline developed by the PROSPECT collaboration [17]. The simulation package is derived from GEANT4 [18] and relies on optimized geometrical modeling. The PROSPECT geometry model and detector response was developed by a team of internal collaborators. The simulation generated a distribution of cosmic events using the Cosmic Ray Generator [19] as well as a distribution of cosmic neutrons. The neutron generator was developed by Dr. Michael Mendenhall from fist principals.

Using this program, Austin Woolverton's used these simulations to isolate the desired events from other backgrounds. Furthermore, he tested the validity of the cosmic ray

generator against theoretical models. Lastly, Austin Woolverton created a method to identify the species of each simulated particle event after the detector response was applied.

Research Presented In Chapter 6

Under the supervision of Dr. Dmitry Pushin and Dr. H. Pieter Mumm, the atmospheric variation study was conducted by Austin Woolverton at the University of Waterloo. It was his responsibility to select muon candidates with well-defined trajectories and compare them to the temperature data. The atmospheric temperature averaging method was taken from de Mendonça [20], and the temperature data was provided by the Integrated Global Radiosonde Archive from the National Centers for Environmental Information [21]. Using this data, Olga Kyzylova performed the necessary averaging and pressure scaling [22].

Chapter 6 also contains the measured rate of muons and their secondaries observed in PROSPECT. The neutron lifetime and capture fraction were previously measured by Adam Hansell at Temple University [7]. Austin Woolverton measured correlated muon-induced events and compared his measured capture time to previous measurements.

Research presented in Appendix A

Appendix A was written by Austin Woolverton at the University of Waterloo under the supervision of Dr. Dmitry Pushin and Dr. H. Pieter Mumm. This section describes the methods used to remove anomalous measurements within the PROSPECT data. It was Austin Woolverton's responsibility to select efficient computational methods and implement them into the PROSPECT framework using C++ and the ROOT analysis package. He implemented and optimized a random sampling consensus method using maximum likelihood [23] and expectation maximization [24]. These methods were originally designed by Torr and Zisserman and modified by Feng and Hung. Austin Woolverton also implemented and optimized a 6-dimensional Kalman filter for the purposes of tracking muons through the PROSPECT detector. This method, was adopted from Zheng [25] where a 6-dimensional filter was used to track gamma events. The equations and method were taken from Frühwirth [26].

Abstract

The Precision Reactor Oscillation and Spectrum Experiment (PROSPECT) has successfully demonstrated novel particle identification strategies with minimal protection from cosmic events. Located at the High Flux Isotope Reactor at Oak Ridge National Laboratories, PROSPECT was developed to investigate the fundamental physics of reactor neutrinos produced through the fission of ^{235}U. Since it is located on Earth's surface, the detector experiences an enormous flux of cosmic backgrounds. These events are removed in the primary spectrum analysis by vetoing events after a muon. Additionally, the spectrum of background events is subtracted from the primary energy distribution. Many cosmic events may accidentally pass these subtractions.

The work presented in this thesis attempts to characterize the cosmic background events observed in PROSPECT while exploring new muon trajectory reconstruction techniques. Due to the segmented design and location, the muon track reconstruction differs from more common likelihood methods used in Cherenkov detectors. Instead, a 4-dimensional principal component analysis strategy is implemented. This method has been extensively tested against Monte Carlo simulations and is used to predict the average track length of through-going muons. In addition, due to the limitations of the PROSPECT detector, more complex tracking routines are suggested.

In addition, the PROSPECT experiment experiences low-energy cosmic events that are typically immeasurable by underground experiments. By exploiting its efficient pulse shaped discrimination strategy, correlations between muons and their secondary events are investigated. This thesis presents a new measurement of the neutron yield taken at ground level. Due to inconsistencies in modeling strategies, as well as its dependence on the total muon flux, the average amount of neutrons produced by cosmic events is widely debated within the low background physics community. An efficient measurement of the neutron yield at Earth's surface may, however, provide supplementary insight to the discussion.

Acknowledgements

The work presented in this thesis would not have been possible without the support and collaboration of many incredible and hard working individuals. I would first like to thank my supervisor, Dr. Dmitry Pushin for awarding me this incredible opportunity and for showing me what it takes to be a physicist. Together, we traveled down a rough and rocky path, but that's how I know it was meaningful. Thank you for your patience during the 2020 global pandemic, and thank you for seeing something in me that I never did.

I would also like to thank the members of the Precision Oscillation and Spectrum Experiment for collaborating in this analysis. Most notably, I would like to thank Dr. H. Pieter Mumm for his incredible guidance and support. Without it, this thesis would not be possible. I would also like to thank Dr. Tom Langford, Dr. Bryce Littlejohn, Dr. David Jaffe, and Dr. Michael Mendenhall for their incredible understanding of particle physics and data analysis techniques.

From the very beginning, and from for when I was feeling at my lowest, I've had the incredible support of my family. To my parents, I could not ask for better people to teach me what's really important in life. To my sister, Naomi, I would like to extend my deepest thanks. Despite being on opposite sides of the country through the majority of my studies, you were always at my side. Thank you for accompanying me on this adventure, and I cannot wait for our next one.

Dedication

This thesis is dedicated to my friends and family.

Table of Contents

List of Figures

List of Tables

Chapter 1

Introduction

Since the beginning of the century, observations from reactor neutrino experiments have prompted for deeper investigations into fundamental physics beyond the Standard Model. At the foreground of these new investigations resides the Precision Reactor Oscillation and Spectrum Experiment (PROSPECT). Located at the High Flux Isotope Reactor at Oak Ridge National Laboratories, its segmented design and proximity to the reactor allows for a unique investigation into neutrino flavour oscillations at short baselines [8]. Furthermore, the collaboration has successfully implemented complex background suppression strategies to purify the reactor signal. In fact, these strategies have awarded PROSPECT one of the highest signal-to-background ratios for its generation of reactor antineutrino detectors [4]. Since their central physics program investigates the flux of reactor anti-electron neutrinos, the distribution of cosmic backgrounds removed by PROSPECT's vetoing strategies have gone mostly unexplored.

The work outlined in this thesis attempts to characterize the interaction of cosmic events observed in PROSPECT. Due to its location on Earth's surface, the antineutrino detector is exposed to a large flux of cosmic events. In particular, the low-energy interactions, such as the decay and capture muons inside the detector, is of particular interest. These interactions are often unobserved by similar experiments deep underground.

In order to characterize cosmic muons through the detector, data analysis techniques were borrowed from computer vision and machine learning. Statistical anomalies caused by measurement reconstruction errors and correlated events demanded for a more sophisticated particle tracking approach, yet the angular dependence of the muon flux was successfully resolved. This tracking program was extensively tested against Monte Carlo simulations before its application on measured data. Lastly, the tracking program helped

quantify the average number of neutrons produced through muon interactions. The neutron yield is often difficult to predict due to conflicting modeling strategies [27, 28] and varying contributions from different interaction mechanisms. In addition, measurements rarely agree because of varying muon spectra observed at different depths underground [13, 29–33]. Consequentially, the cosmic neutron yield is a controversial topic among the low background particle physics community.

1.1 An Introduction to Neutrino Physics

The remainder of this chapter introduces the motivations behind reactor neutrino experiments. It begins by outlining major historical developments that culminated in the modern generation of neutrino detectors, and it concludes by describing some unsolved questions arising from observations throughout the community.

1.1.1 History of Neutrino Experiments

On December 4th of 1930, Wolfgang Pauli hypothesised the existence of a seemingly undetectable neutrally charged particle [39]. During this time, the theoretical physics community was troubled by the continuous spectrum observed from nuclear beta decay. Since this process was believed to be a two-body system, the accepted theories predicated a monoenergetic spectrum. This apparent violation of energy conservation was dismissed by Neils Bohr who asserted that a continuous spectrum is only valid statistically. The produced daughter nuclei, however, were observed with the same or fractional spin as their parent. His dismissal did not address this violation of angular momentum conservation.

In an open letter addressed to *"Radioactive Ladies and Gentlemen"*, Pauli introduced his invention to a conference of experimental physicists in Tübingen, Germany. Concerned that experiments may never be able to detect his particle, which he called the neutron, his idea was never published. The discovery of the neutron was reported on May of 1932 by James Chadwick; however, it was too heavy to be Pauli's neutron. In 1934, the first theory of weak interactions and beta decay was formulated by Enrico Fermi [40]. This theory encapsulated this mysterious particle and named it the neutrino.

$$n \rightarrow e^{-} + p + \overline{\nu}_{e} \tag{1.1}$$

The first experimental evidence that directly supported this particle was presented by C.L. Cowan and F. Reines [41]. At the Savannah River power station, they exploited the

underlying physics of the inverse reaction. The inverse beta decay (IBD) reaction cannot be measured directly; therefore, they searched for correlated prompt beta and delayed neutron events.

$$\overline{\nu}_e + p \rightarrow e^+ + n \tag{1.2}$$

Using two large water tanks filled with aqueous $CdCl_2$, they successfully measured the desired signal. First, a distinctive energy signature was identified from the positron annihilation. Within 10 μs of this event, a coincident neutron event was observed to capture on cadmium. This prompt and delayed coincidence technique is still widely used for similar investigations.

It is now accepted that there are 3 flavours of neutrinos corresponding to the leptonic component of their interactions. This was first demonstrated in 1962 by Lederman, Schwartz, and Steinberger [42] where they successfully distinguished between the electron and muon neutrino. For this discovery, they became the 1988 recipients of the Nobel Prize in physics. The τ leptonic flavour was postulated in the late 1970s.

Early solar neutrinos studies attempted to validate to Standard Solar Model by estimating the number of particles produced through proton fusion chains within the Sun. The Standard Solar Model is a mathematical treatment of astronomical bodies, and it is capable of predicting stellar evolution. Solar neutrinos propagate towards Earth and scarcely interact through gravity and the weak nuclear force. Consequentially, the active volume of early experiments were extraordinarily large.

Lead by Raymond Davis, the Homestake experiment was constructed in 1965 [43]. Its purpose was to count the flux of solar neutrinos incident to a 100,000-gallon active volume deep underground. The active volume was filled with perchloroethylene[1], and the neutrino interactions on chlorine were investigated by counting the number of produced argon atoms.

$$\nu_e + {}^{37}\mathrm{Cl} \rightarrow {}^{37}\mathrm{Ar} + e^- \tag{1.3}$$

At the end of each week, tens of argon atoms were accumulated in a helium bubble chamber. Unfortunately, approximately one-third of the predicted argon atoms were observed. This suggested that either the predictive capabilities of the Standard Solar Model were accidental, or the Davis experiment was faulty. Beginning in 1970, the deficit was consistently measured until the Homestake experiment retired in 1999. During this time, no major revisions to the model were proposed. This disagreement between observed and predicted neutrino flux became known as the Solar Neutrino Problem.

[1]Perchloroethylene is primarily used for dry-cleaning fabrics.

It is now known that the Davis experiment was only sensitive to the electron type neutrino. Experiments such as Kamiokande, and its later upgrades, were sensitive to both the muon and electron-type neutrino. As a result, the Super-Kamiokande collaboration found evidence for neutrino oscillations [44]. Neutrinos are hypothesized to change their flavours through the quantum mechanical superposition of the flavours and their 3 masses eigenstates. The probability that a particular flavour of neutrino is measured varies sinusoidally with energy and distance from its source. In 1998, after they observed inconsistencies between the predicted solar ν_μ zenith dependence with their observations, the Super-Kamiokande collaboration placed constraints on the oscillation parameters. The Sudbury Neutrino Observatory is sensitive to all three lepton flavours, and it is capable of measuring the flux of solar neutrinos from all directions. Their initial results were published in 2001 [45], and they confirmed the observations from Super-Kamiokande. Raymond Davis received a Nobel Prize in 2002 for his contribution to solar neutrinos.

Currently, a variety of collaborations throughout the world work diligently to construct a coherent image of neutrino mixing and flavour changes. The new generation of reactor experiments have significantly more control over the incident neutrino energy and travel distance than previous solar neutrino studies; however, anomalous measurements suggest that the current understanding of reactor neutrino physics is incomplete. Thus, modern reactor experiments, such as Daya Bay [1], RENO [2], Double Chooz [46] and PROSPECT [4], attempt to resolve the remaining unsolved mysteries of neutrino physics.

1.1.2 The Reactor Spectrum and Flux Anomaly

Reactor neutrino experiments indirectly measure the neutrino spectrum by unfolding the visible energy observed in the IBD signals.This is done using the energy and momentum transferred to the beta. The theoretical spectrum, on the other hand, is derived using the nuclear physics of the time-evolving reactor composition. As a result, the theoretical beta spectrum must be converted to reflect the neutrino interactions.

One possible conversion method considers all possible β branch ratios for a given reactor source as well as its fission products [47]. Unfortunately, not all branch ratios are well understood; this has resulted to large systematic uncertainties in the predicted spectrum. An alternative method approximates the spectrum uses only 30 virtual branches [48]. The Huber-Mueller model is a combination of the two methods [49]. In fact, Mueller argues that this method leads to a 2.5% increase in detectable neutrinos. Regardless of which method is selected, current reactor neutrino measurements have yielded surprising results.

The first is the *reactor antineutrino anomaly*. As depicted in figure 1.1, an apparent neutrino flux deficit of $\sim 6\%$ is observed between predictions and measured data. The largest deviation from the predicted flux is reported by the Institut Laue-Langevin (ILL) experiment at 8.78 m from the neutrino source [50]. Although the origin of this deficit remains a mystery, it has lead to the hypothesis of a fourth sterile neutrino flavour [51] insensitive of the weak nuclear force. If a discovery was ever performed, it would have far reaching consequences throughout the theoretical physics community and potentially lead to revisions of fundamental particle physics.

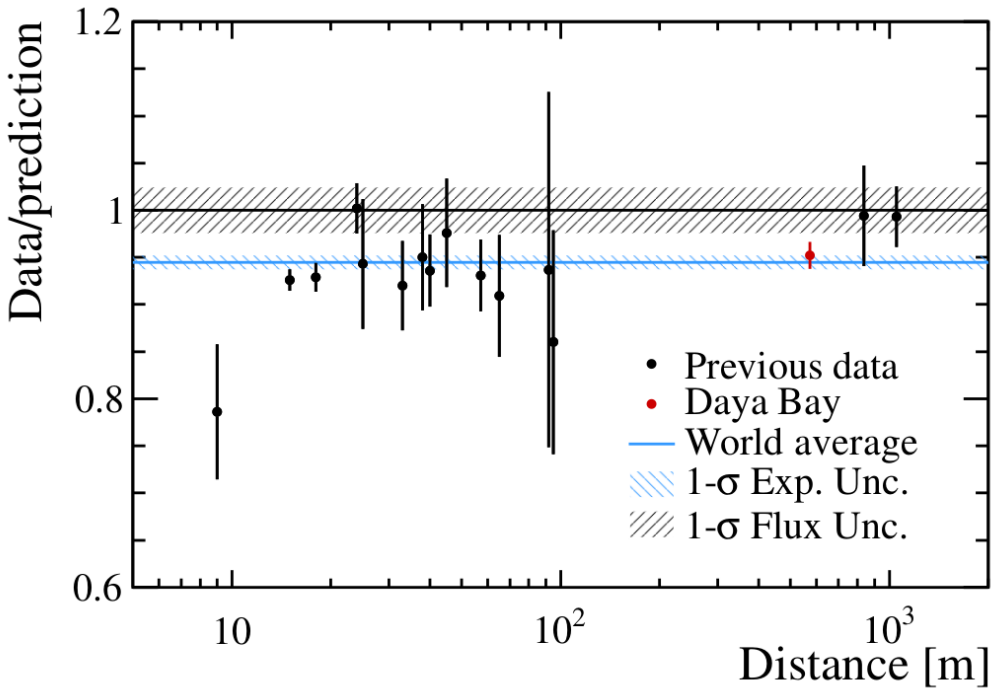

Figure 1.1: The measured flux of reactor antineutrinos is contrasted against predictions across many different baselines from the neutrino source [3].

The second is the *reactor spectrum anomaly*. The measured IBD spectrum is contrasted against the combined Huber-Mueller model [48, 49] or the older Vogel model [52]. A disagreement is, however, observed, between 4 and 6 MeV as illustrated in figure 1.2. This anomaly cannot be explained through neutrino oscillations, and is more likely a result of improper reactor modeling. This spectrum anomaly has been observed through many reactor experiment [1, 2, 4, 46], and its true origin remains a mystery.

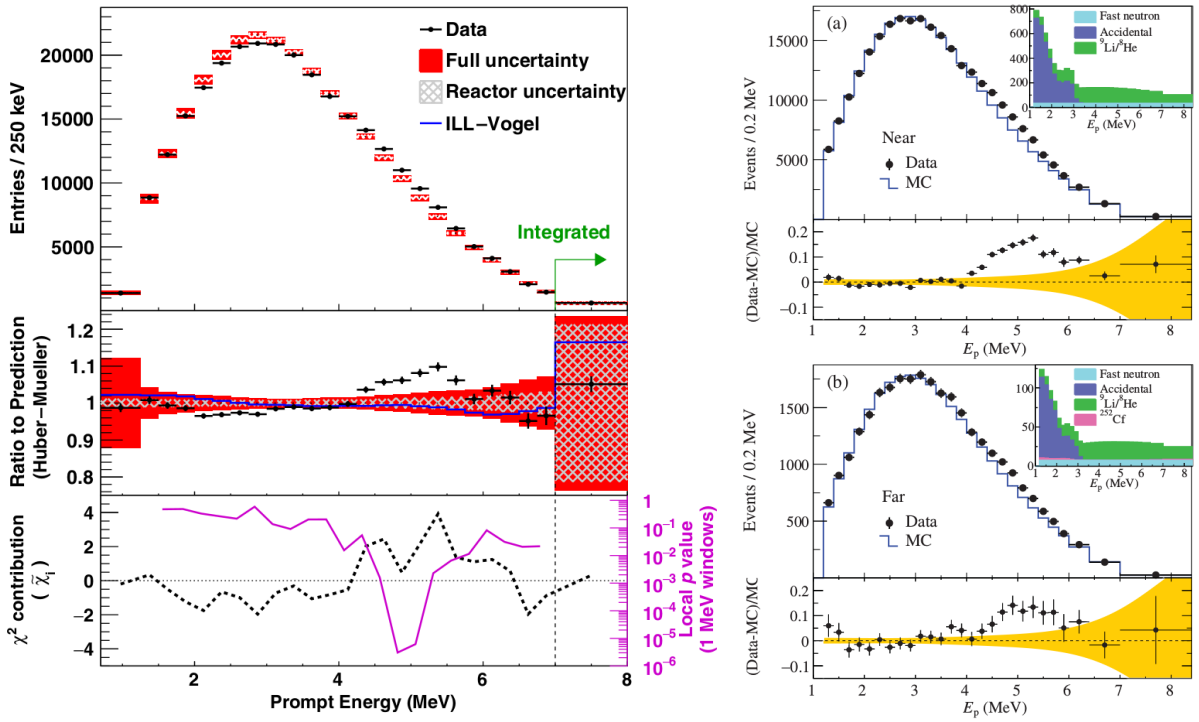

Figure 1.2: Taken from [1] and [2] respectively, the reactor IBD spectra measured by Daya Bay (a) and RENO (b) are illustrated. The results from RENO's near and far detectors are presented in the top and bottom panels respectively. Furthermore, their background components introduced through fast neutrons and the decay of rare isotopes arising through cosmic muon spallation are summarized. The statistical significance of Daya Bay's results are also displayed. Their χ^2 values where obtained through 1 MeV windows.

The new generation of neutrino detectors aim to resolve these anomalies by implementing novel design and background suppression strategies. If the ILL measurements are to be believed, a search for sterile neutrinos must be performed at very short baselines. This maximizes the flux of anti-electron neutrinos. Furthermore, a uniform and pure source of neutrinos may be employed in order to eliminate the atomic structure as a possible source for the reactor spectrum anomaly.

Chapter 2

The PROSPECT Experiment

In an effort to address both the reactor spectrum and flux anomalies, the Precision Reactor Oscillation and Spectrum Experiment (PROSPECT) probes the electron antineutrino spectrum produced by the neighbouring High Flux Isotope Reactor (HFIR). Due to its location at the surface, the PROSPECT antineutrino detector is constantly exposed to cosmic showering events. Many collaborations, such as Daya Bay [1] and Double Chooz [46], address the constant flux of cosmic backgrounds by building their experiments deep underground. The surrounding rock provides ample shielding from external signals that would otherwise contaminate the experiment. The PROSPECT detector, on the other hand, possesses minimal overburden against cosmic backgrounds. Regardless, through efficient design and precise calibrations, it produced a high quality short baseline spectrum and flux measurement by exploring correlations between particle events [4].

By probing the highly enriched ^{235}U core at the HFIR facility, PROSPECT is capable of extracting the neutrino spectrum from the associated IBD interactions. In addition, due to its segmented design, the spectrum is probed at different baselines. These important design features allowed the collaboration to investigate both the reactor spectrum and flux anomalies. A pure source of uranium allowed the collaboration to test its decay chain beta spectrum as a possible cause for the spectrum anomaly. Moreover, a baseline investigation between 7 and 9 meters permitted the search for sterile neutrinos.

This section will describe the design and performance of the detector. First, additional details about HFIR are provided. Following this discussion will be a brief introduction to the inner liquid scintillator array and the outer shielding components. A description of the data acquisition and processing routine is provided as well as an overview of the neutrino detection strategy.

2.1 The High Flux Isotope Reactor

The High Flux isotope Reactor (HFIR) is a research reactor facility located at Oak Ridge National Laboratories (ORNL). The laboratory's main research objectives are for medical and industrial applications. It also provides a steady source of neutrinos for reactor experiments. This location maximizes the total exposure across all baselines while maintaining a point-like neutrino source by allowing the detector to be in close proximity to the reactor.

The reactor core consists of highly enriched ^{235}U. The enrichment reaches approximately 93%; furthermore, over 99% of the nuclear fission reactions at HFIR are expected to arise from this isotope of uranium. A detailed description of the reactor model and evolution can be found in [53].

With a duty cycle between 20-30 days, the HFIR operational cycle is relatively short. The period where the reactor is in operation is referred to as *reactor-on*. Alternatively, The *reactor-off* periods occur after the fuel is spent. Routinely, the water level in the cooling chamber is reduced from its maximum height of 8 m to about 5 m. This gives technicians access to the reactor core to replace the fuel rods. The water level is, however, not reduced regularly. The entire operation typically last 2 or 3 days in order to maintain constant conditions through the experiment.

2.2 Neutrino Detection Strategy

Since its introduction in 1956, the Cowan–Reines method of prompt and delayed coincidence [41] has found widespread popularity within the neutrino oscillation community. Consequentially, the PROSPECT antineutrino detector borrows its IBD selection techniques from its predecessors. Unlike the original experiment, however, the PROSPECT collaboration was faced with strict health and safety regulations imposed by ORNL. Due to its close proximity to the reactor core and periodic maintenance routines, the chosen scintillating material must be non-flammable and have a low toxicity. Furthermore, due to the detector's compact design, the neutron capture signal must be topologically localized with a high light yield. Thus, antineutrinos were identified using the IBDs from ^{6}Li-loaded EJ-309 organic liquid scintillators [4, 6, 8].

A visual summary of PROSPECT's IBD detection strategy is presented in figure 2.1. The event is identified from a prompt positron signal and a delayed neutron capture event. The prompt beta loses energy through ionization before annihilating on the valence electrons of the organic scintillating element. The neutrino spectrum is determined using the ionization energy, and the electron-positron annihilation releases 2 gamma quanta.

$$e^+e^- \rightarrow 2\gamma. \tag{2.1}$$

The neutron thermalizes before capturing on either lithium or hydrogen. These interactions are summarized below in equation 2.2 and 2.3 respectively. The scintillating light detected from the capture on hydrogen (nH) and the trialing gamma collisions, is statistically distributed around the *hydrogen capture peak* (E=2.2 MeV).

$$n + {}^1\mathrm{H} \rightarrow {}^2\mathrm{H} + \gamma \tag{2.2}$$

$$n + {}^6\mathrm{Li} \rightarrow t + \alpha \tag{2.3}$$

On the other hand, the *lithium capture peak* (nLi) is the combined result of both the triton (E = 2.05 MeV) and the alpha particle (E = 2.73 MeV). The detected energy is, however, greatly reduced from the interactions of heavy particles through the liquid scintillator. The denser trails of ion de-excitations are less likely to excite the scintillating volume. As a result, the total energy is *quenched* from E= 4.78 MeV to $E_{vis} \approx 0.5$ MeV.

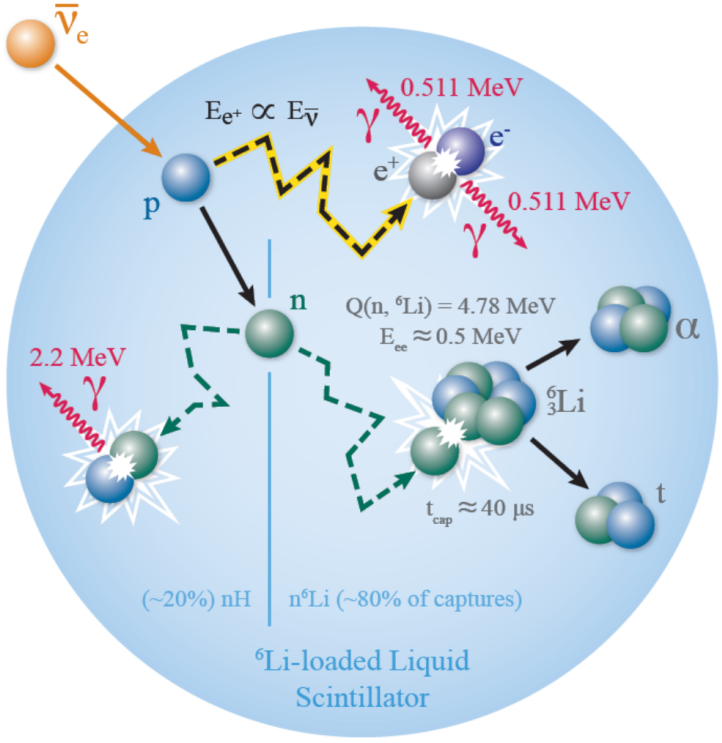

Figure 2.1: An illustration, taken from [5], representing the initial inverse beta decay and its secondary interactions within PROSPECT's ^{6}Li-loaded liquid scintillators.

Both the time required for the neutron to thermalize and the capture fraction between hydrogen and lithium have been validated [7]. These values are expected to deviate through the duration of the experiment due to the variability in the detector's optical properties. The neutron capture fraction was calculated using the number density of the capture target and its inclusive cross section. The resulting ^{6}Li capture fraction, and the selection efficiency, is summarized in table 2.1. The neutron selection criteria was methodically adjusted to maximise the amount of identified events. Further information about the selection of neutron capture on ^{6}Li, summarized in section 2.3.2, can be found in [4, 7]

Property	Value
nLi capture time	$49.83 \pm 0.05\,\mu$s
^{6}Li capture fraction	0.744 ± 0.007
^{6}Li capture selection efficiency	0.8914 ± 0.0003

Table 2.1: The different properties of the nLi capture events within PROSPECT's liquid scintillators are summarised. Values are taken from [7].

2.2.1 Inner Detector

The inner detector contains the entire active volume consisting of a 14×11 array of lithium loaded liquid scintillators (LiLS) and the photomultiplying tubes (PMTs) on the end of each segment. The outermost segments are typically removed from the analysis, resulting in a fiducialized inner mass of 2581 kg. It also contains the 3D-printed pinwheel support tabs and the optical components responsible for capturing scintillating light and optically isolating each segment. These support tabs tilt each segment by $\sim 5.5°$ to allow access to each segment for calibration.

The LiLS was developed by an internal subgroup by modifying a commercially available EJ-309 liquid scintillator [6]. Conducted at NIST and Brookheaven National Labs, an aqueous solution of LiCl was added to form a thermodynamically stable microemulsion, and the targeted concentration of lithium was 0.1% by mass. The chemical composition is summarised in table 2.2, and the final ^{6}Li doping fraction by mass is $0.082 \pm 0.001\%$.

Figure 2.2 illustrates a typical scintillator segment. Reflective panels direct the scintillating light toward the PMTs located at either end of the segment. Excluding the PMTs, each segment is 117.6 cm long with a cross section of 14.5 cm^2. Thus, the total active volume is 1.176 m wide $\times$ 2.045 m long $\times$ 1.607 m tall.

	Concentration (by Mass)
H	$84.34 \pm 0.11\%$
O	$9.69 \pm 0.21\%$
C	$5.97 \pm 0.24\%$
Density (g/mL)	0.9781 ± 0.0008

Table 2.2: The chemical composition of the PROSPECT LiLS is taken from [6].

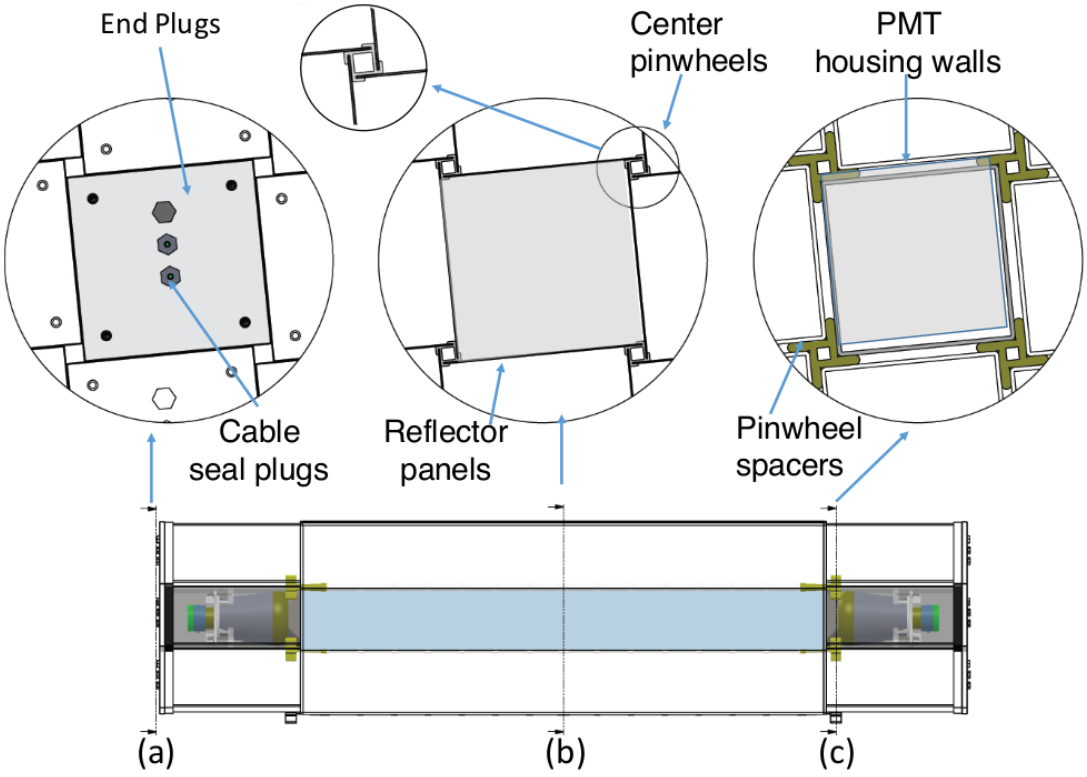

Figure 2.2: This diagram, taken from [8], depicts a single liquid scintillator segment and its support rods. Each cross section illustrates different regions of the segment. (a) illustrates the cable output required to connect the PMTs the the remaining data acquisition network, (b) illustrates the center pinwheels and optical separators, and (c) illustrates the connection between the active volume and the PMT tube housing.

Each segment is capped with a PMT on each end of the segment. The PMTs are enclosed in liquid-tight rectilinear acrylic housing filled with optical grade mineral oil. Figure 2.3 represents a typical PMT. A 13 mm thick window resides between the PMT and the scintillator where conical reflectors help guide the scintillating light into the optical element. The back plug, and the electrical components, exit the segment at the opposite end.

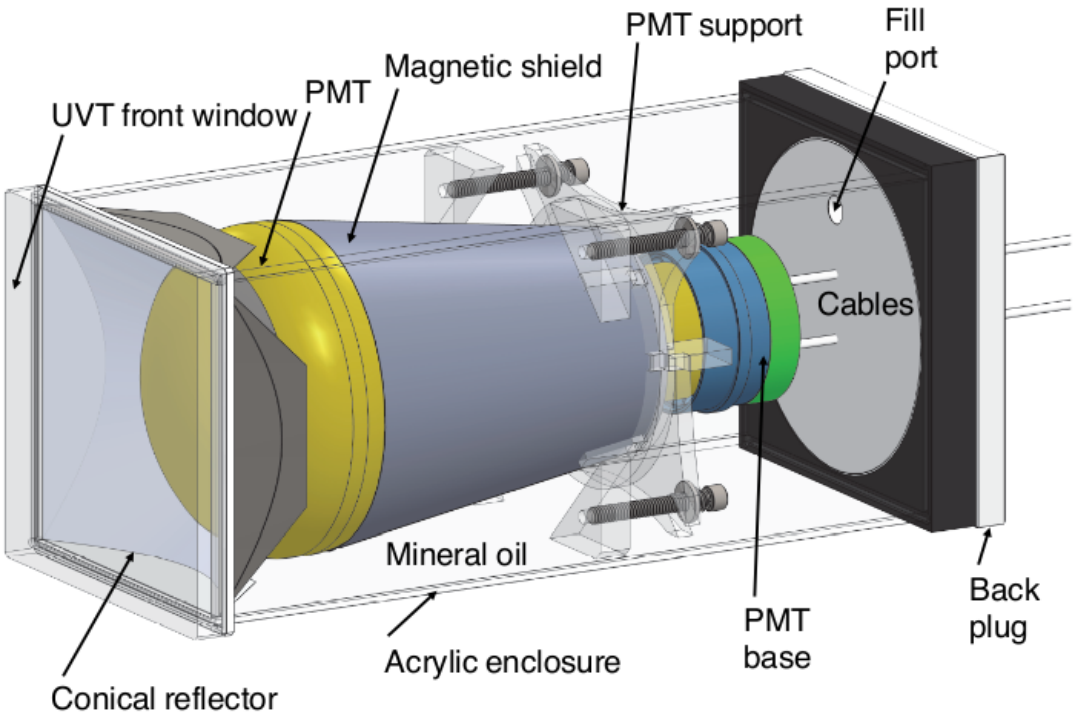

Figure 2.3: This diagram represents the PMT housing and is taken from [8].

2.2.2 Outer Detector

Intended to reduce signals from external neutron and gamma sources, the outer detector is composed of several enclosing shielding layers. The development of PROSPECT's shielding network was motivated by local background events observed at HFIR as well as the performance of early prototypes [8]. It consists of several interlocking layers of lead and 5% borated polyethylene (BPE) enclosing the active volume.

Figure 2.4 illustrates the shielding layers encasing the inner array of segments. An inner acrylic and outer aluminum containment vessel is installed to prevent the inner LiLS from leaking. BPE or water is placed between these vessels to reduces the stress on the acrylic. The outer aluminum vessel is encased in lead shielding and plastic lumbar support structures, and bricks of demineralized water are placed at the top of the detector to attenuate the flux of downward cosmic neutrons. Additional information about the different detector components, and their installation, is found in [8].

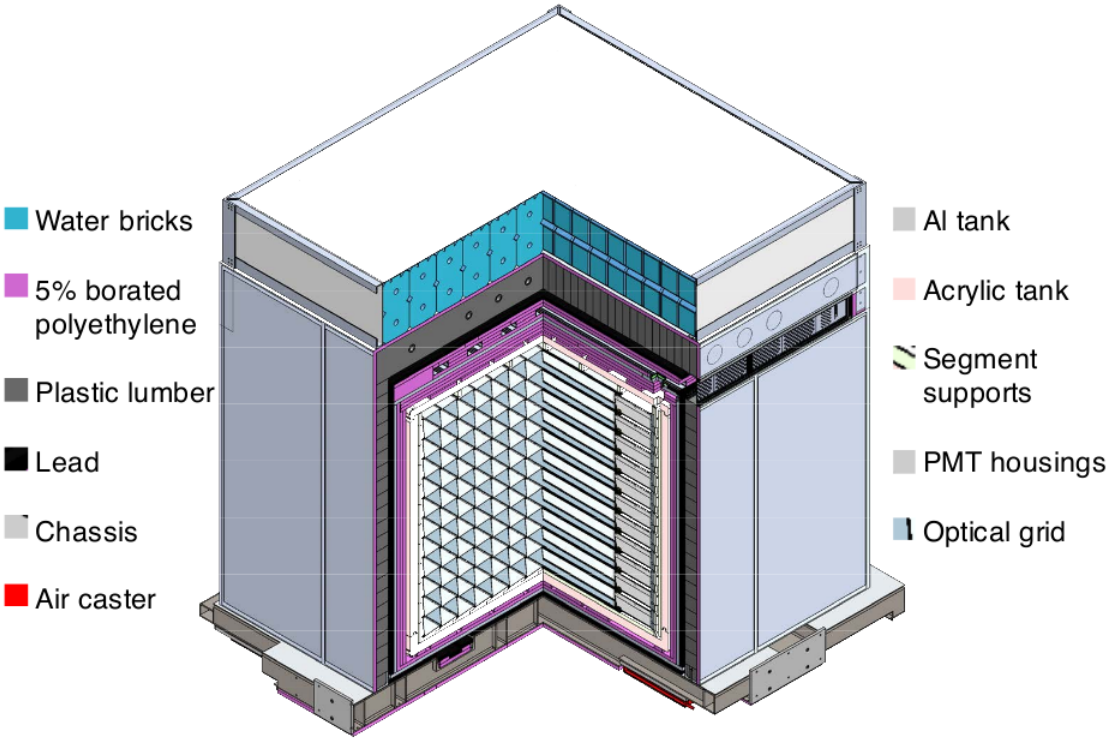

Figure 2.4: This diagram, taken from [8], depicts the different components of the PROSPECT detector. The active volume and PMT housing is enclosed by an acrylic containment vessel (rose). A layer of BPE (violet) is enclosed by an outer aluminum containment vessel (light grey) and lead shielding (black).

The shielding, coupled with powerful particle identification techniques and background subtraction strategies, sufficiently remove the background spectrum in the primary oscillation and spectrum analysis. The shielding does not, however, sufficiently attenuate the flux of cosmic muons. These events, and there associated secondaries, may introduce additional

false IBD candidates into the experiment. Correlated muon-induced events are the subject of this thesis, and are difficult to remove through vetoing and background scaling alone.

2.3 Data Processing

Data collection occurred between March and October of 2018. During this time, many PMT segments experienced a performance quality degradation. Of the 154 detector segments, 64 PMTs experienced electrical current instabilities. 36 of these segments were within the inner fiducial volume. These segments were excluded from the final analysis.

The events, measured by the remaining active segments, underwent a vigorous calibration and analysis pipeline. If both PMTs register an event above a predefined energy threshold, the event is collected for later reconstruction and analyses. Events observed by PMTs in the same segment are referred to as *pulses*. These events, relevant for low-energy correlation studies, contain calibrated position, time, and energy measurements. High-energy events, however, may include multiple segments. In this case, if they occur within 20 ns of each other, pulses are grouped together into *clusters*. The total cluster energy is used for a variety of physical analyses including isolating reactor signals from cosmic backgrounds. The position of the event is, for non-localized events, measured using the pulse with the highest energy. Additional information about the event calibration and classification, as well as the cosmic vetoing procedure, can be found in [4].

This section will describe how pulsed events are processed before they are used in higher level analyses. It will begin by describing how the converted signal is used to determine the arrival time, energy, and particle species. It will also describe how the delay between the two PMTs is used to measure the event's position along the length of the segment. This section will conclude by briefly describing how these measurements are influenced at high pulse energy.

2.3.1 Arrival Time Reconstruction

When the PMTs receive a signal, the associated waveform digitizer records approximately 592 ns of analog-to-digital channel (ADC) samples. The ~ 200 ns before the signal is used for background scaling. Each sample corresponds to about 5 photoelectrons within the respective PMT, and the total waveform contains $\sim$ 148 samples. The pulse's arrival time is, therefore, interpolated by scanning backwards from the maximum ADC sample.

The arrival time is interpolated to the first level crossing at 50% of the maximum; this is depicted by the dashed vertical line in figure 2.5.

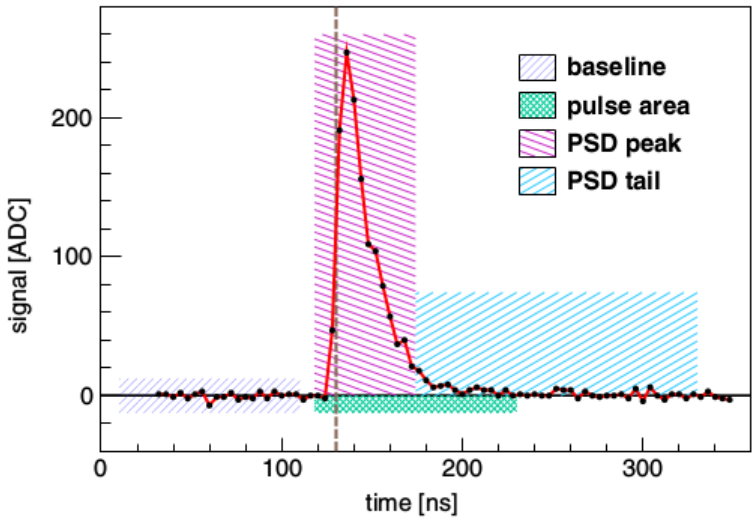

Figure 2.5: An example of a small electron signal is taken from [4]. The dashed line represents the half height from the leading edge, and the different highlighted regions are used for baseline subtractions as well determining the pulse shape metric, and the deposited energy of the event.

2.3.2 Pulse Shape Discrimination

The PROSPECT collaboration is able to distinguish between different particle species using the distribution of the waveform. This pulse shape discrimination (PSD) technique arises from the light transportation properties of liquid scintillators. Specifically, charged particles will lose energy as they travel through the scintillator, and the amount of kinetic energy converted to scintillating energy is dependant on the particle species. The scintillating light is guided down the length of the LiLS segment and read by the PMTs on either end. The final pulse shape parameter is determined by integrating the total current $Q(t)$.

$$PSD = \frac{Q_{tail}}{Q_{full}} = \frac{\int_{\text{tail}} Q(t)dt}{\int_{\text{total}} Q(t)dt} \tag{2.4}$$

The limits of integration were selected to maximize the discriminating capabilities between neutron captures and other γ-ray interactions at similar energies. According to figure 2.5, the tail region is between 11 and 50 ADC signals after the leading edge of the pulse. The total signal, on the other hand, begins approximately 3 ADC samples before the leading edge. The resulting PSD parameter is capable of distinguishing electron recoil events from nuclear recoils due to differences in deposited energy dE/dX. This is illustrated in figure 2.6. Thus, electron events are identified if they fall within 2.5σ of the electronic recoil band, and nLi events are identified if they fall within 1.8σ of the nuclear recoil band with an energy within 3σ of the lithium capture peak (0.55 MeV).

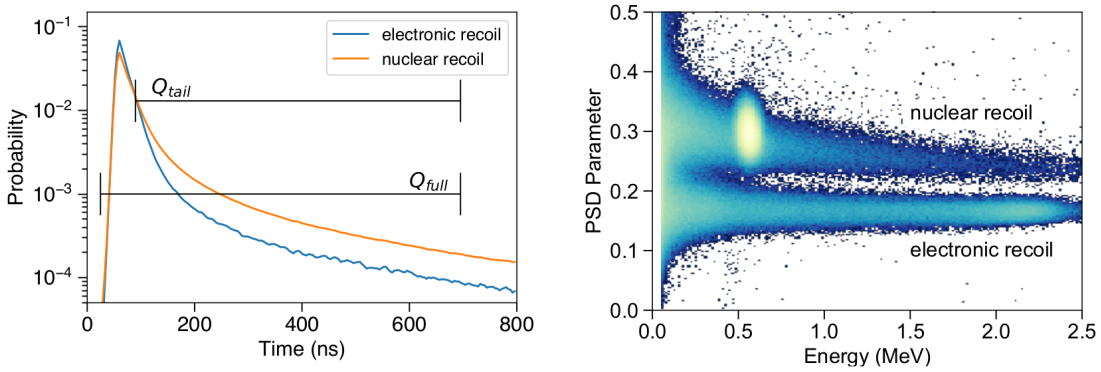

Figure 2.6: An example of the waveform template from the early prototype (left). Due to the larger tail fraction, the nuclear recoil event has a larger PSD figure of merit than the electron recoil event. The resulting nuclear and electronic bands are also displayed (right). Furthermore, the lithium capture peak is visible in the nuclear band near 0.55 MeV. These figures were taken from [6].

2.3.3 Energy Reconstruction

The non-linear dependence between the energy deposited in a segment and the visible energy measured by the PMTs is corrected through neutron source calibrations. Furthermore, the visible energy is also dependant on the position relative to the optical device. An event near a PMT may appear to have a larger energy than farther events. As a result, the calibration is separated into two steps. A consistent measure of the visible energy E_{vis} is obtained before PMT nonlinear effects are introduced. Then, nonlinear PMT effects are removed by applying a detector response function generated through Monte Carlo simulation methods.

According to [4], the visible energy is calculated by adding the measured photoelectrons measured by both PMTs, and divide out a position-dependent light collection factor. This is expressed in equation 2.5. The visible energy is dependent on the integrated signal S_i at each PMT and the reconstructed position along the segment z_{rec}. This quantity is described in detail in section 2.3.4. The remaining parameters are estimated using events near the center of the segment. The gain stability constants g_i represent the pulse area signal at the center of the segment, n_i is the expected number of photoelectrons collected from events at the center, and η_i is the position-dependent light transport efficiency for the i^{th} PMT.

$$E_{vis} = \frac{S_0 n_0/g_0 + S_1 n_1/g_1}{n_0\eta_0 z_{rec} + n_1\eta_1 z_{rec}} \tag{2.5}$$

The energy reconstruction was calibrated using cosmic neutron events [4]. Neutron capture on ^{6}Li is a mono-energetic signal that is easily separated from gamma backgrounds. The gain stabilizing constants are determined for each PMT across 1 hour exposure periods, and n_i is calibrated using the width of the lithium capture peak. Using several intervals of accumulated neutron capture measurements, the light transport efficiency curves were determined for every 2 weeks of data. The large exposure time was necessary to generate the appropriate statistics for accurate data fitting. The determined parameters are stored in the appropriate calibration database.

2.3.4 Position Reconstruction

Due to the differences in the signal at each end, the double ended segments allow for position resolution along the length of the segment. The other coordinates are limited by the segmentation of the detector; therefore, the x and y coordinates are approximated by the central axis of the segment.

The z coordinate, measured along the length of the segment, is determined using the overall light yield and the differences in arrival times Δt at the PMTs. Two fits are needed to reconstruct the position. The log ratio of pulse signals $R = \log(S_1/S_0)$, as well as the position, are fit to their respective distributions.

$$z(\Delta t) = a\Delta t + b(\Delta t)^3 \tag{2.6}$$

$$R(\Delta t) = a + b\Delta t + c(\Delta t)^3 \tag{2.7}$$

A uniform signal with known periodicity was needed for calibration. Corner clipping muon events provided a large and uniform calibration sample with well defined positions

within the segments[4]. Since these events traverse the pinwheel support rods, the sampled light transport contains distortions in both magnitude and time. This results in a minor oscillation in the position distribution with a spacial period consistent with the average distance between the support tabs. This is colloquially referred to as the tiger striping or *Hobbes* effect. This calibration was carried out a total of 11 times throughout the experiment to account for the evolving optical characteristics of the detector.

2.3.5 Reconstruction Errors at High Energies

Thus far, the reconstructed arrival time, position, energy, and PSD figure of merit have been discussed. These reconstructions, and their respective calibrations, are performed using well behaved ADC triggers. If, however, an event deposits a large amount of fluorescence into the segment, the waveform digitizers will overstate. The highest ADC samples will not register, and the waveform will appear trimmed near the top. This effects the reconstructions in a variety of detrimental ways.

1. The waveform's tail region Q_{tail} is typically unaffected; however, the total integrated charge Q_{total} is reduced. The resulting PSD figure of merit, calculated as the tail over total ratio, is artificially increased.

2. The maximum ADC sample cannot be determined; therefore, it is taken as the leading cutoff edge. As a result, the first level crossing at half the maximum, and the interpolated arrival time, are shifted away from their true values.

3. After E_{vis} is calculated, the energy scaling factor must be determined through simulations. The appropriate waveform template, however, cannot determined accurately.

The clipping effect introduces non-Gaussian errors into the measurements. Fortunately, the neutrino oscillation and IBD spectrum analysis are largely uninfluenced by this. Investigations into high-energy cosmic backgrounds, however, are at the mercy of clipped signals. The influence of clipping is discussed in more detail in later sections. Section 4.4.1 illustrates how the clipped waveforms are replicated through simulations. With regards to isolating muon samples, section 5.1 illustrates the different anomalous measurements that contaminate the sample. Many of these are caused by clipped waveforms.

2.4 PROSPECT Spectrum Results

The PROSPECT-I detector was in operation from March to October of 2018. During this time, the collaboration was able to observe the production of over 500 000 IBD candidates. Furthermore, the results outlined in [4] demonstrate one of the strongest limits on the eV-scale sterile neutrino oscillation parameters as well as a precises measurement of the spectrum from ^{235}U.

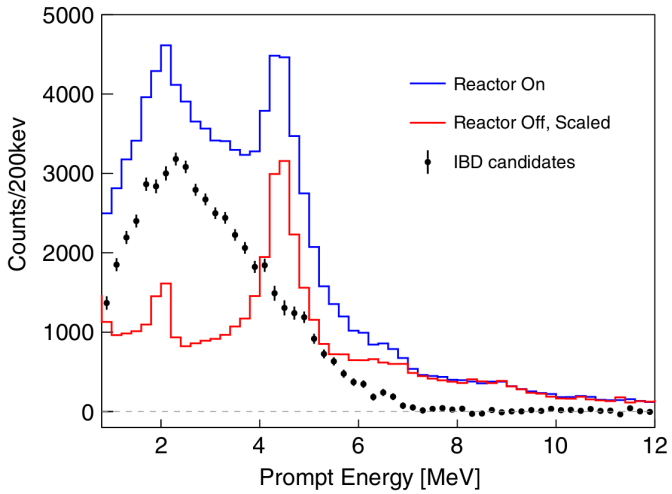

Figure 2.7: The background-subtracted spectrum of IBD prompt events is taken form [4]. The correlated events from the reactor-off period (red) is scaled to match the exposure time of the reactor-on measurements (blue).

Figure 2.7 displays the spectrum of IBD prompt signals measured throughout the experiments total exposure time [4]. The events located around the hydrogen capture peak (2.2 MeV) and the first excited state of carbon-12 (4.43 MeV), are accidental events that mimic the desired IBD signal. These are subtracted from the measurement using IBD-like cosmic backgrounds identified during the reactor-off period. A background subtractions strategy, such as the one performed by PROSPECT, is only valid if all events during the reactor-off period scale uniformly with time. Concerns arose involving the backgrounds introduced during the reactor maintenance periods when the water level in the HFIR cooling pool was reduced. It was determined that these backgrounds do not contribute significantly to the overall count rate of false IBD candidates. This was validated by inspecting the muons that travel through the reactor cooling pool before depositing energy into the active volume. This study is described in appendix B.

Figure 2.8 contrasts the measured IBD spectrum against the Huber Model. In order to contrast the spectrum results against other experiments, specifically within the 4 to 6 MeV region, a Guassian peak centered at 5.678 MeV and standard deviation of 0.562 MeV was introduced to the HFIR model before the detector response was applied. The Guassian parameters were taken from the Daya Bay spectrum results [3]. According to [4], the spectrum measurement performed by the PROSPECT collaboration is consistent with other neutrino oscillation studies such as Daya Bay; however, the hypothesis that ^{235}U is entirely responsible for the spectral distortion was disfavoured with a confidence level of 2.44σ. Furthermore, the data disfavours a null hypothesis of no observed distortion by approximately 2.17σ.

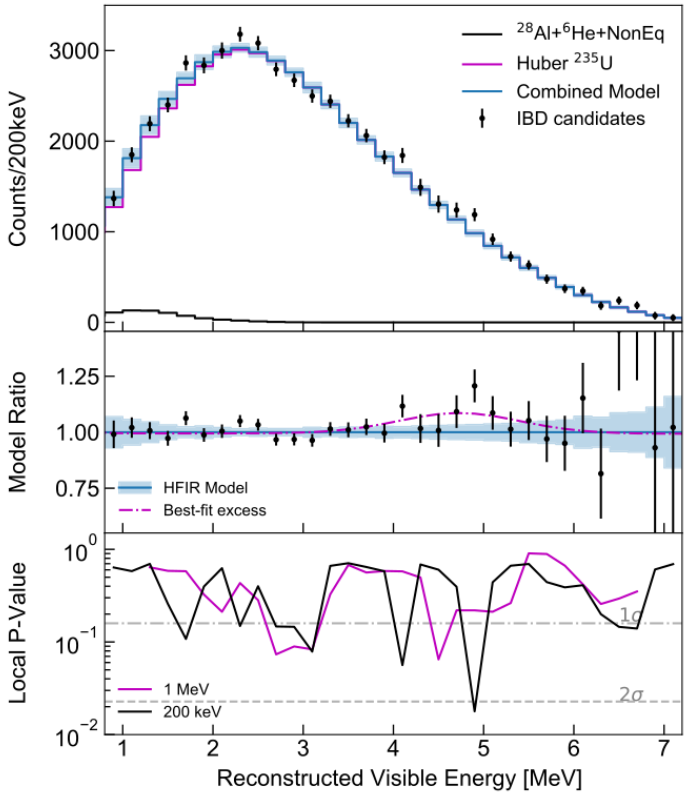

Figure 2.8: The spectrum results from PROSPECT are taken from [4]. The top panel illustrates the background subtracted IBD spectrum in comparison to the reactor model, and the middle panel illustrates the ratio between the measured and predicted rate across different energies. The statistical significance is illustrated in the bottom panel where the local p-values were obtained across 200 keV and 1 MeV energy windows.

Chapter 3

Muon-Induced Cosmic Backgrounds

Neutrino oscillation experiments, as well as other studies that probe for rare particle interactions, are susceptible to a variety of unwanted particle signatures. These backgrounds may overlap the desired search window and contaminate the desired spectrum. In the search for neutrino oscillations, the desired outcome is a prompt beta signature followed by a delayed neutron capture signature.

Backgrounds contain two events that overlap the IBD signal. These can be characterised into two different groups. Accidental backgrounds occur if 2 uncorrelated events randomly pass the specified selection requirements and occur within the desired time window. These are removed by applying the appropriate accidental subtractions and vetoing procedures. Correlated backgrounds, however, occur when a single source creates both a mimicking prompt and delayed signal. These backgrounds are more difficult to remove. This section will outline the different backgrounds that arise from cosmic muons as well as their origin with atmospheric showers.

3.1 Composition of the Atmospheric Shower

After interacting with the atmosphere, an incident cosmic ray may create a cascade of particle events. The composition of the cascade, typically referred to as an air shower, is the primary subject for many above-ground experiments. A typical cascade is illustrated in figure 3.1. If the initial scattering event involves an incident photon, electron, or positron, the shower will have a large electromagnetic component. Alternatively, if the primary event involves a heavier nuclear interaction, a hadronic and muonic component is expected. The

muonic component is deeply penetrating and detectable far underground. As a result, local muon-induced hadron events, specifically cosmic ray induced neutrons, are prevalent backgrounds in antineutrino experiments [38, 54].

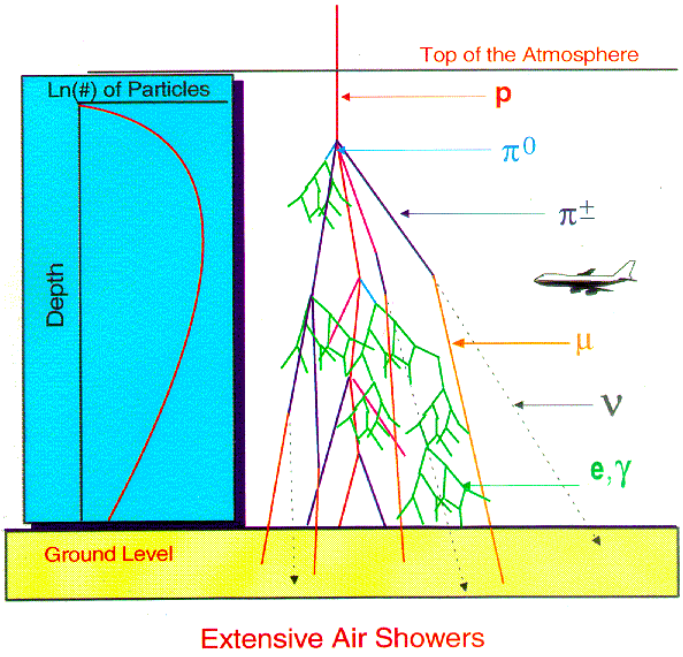

Figure 3.1: The air shower's composition is illustrated. Additionally, the relative number of particles L_n in the cascade is contrasted against the atmospheric depth. This image was adapted from the archives of the university of Adelaide [11].

3.1.1 The Electromagnetic Component

The electromagnetic component arises when a high-energy electron, positron, or photon interacts with matter. High-energy photons, typically on the order of MeV, predominantly lose energy through matter/anti-matter pair production. Below this energy range, Compton scattering and photoelectric interactions dominate. The electron and composite positron lose energy as Cherenkov radiation and additional gamma particles are generated through bremsstrahlung. These gammas, if given sufficient energy, may contribute to additional showers. As a result, the electromagnetic component alternates between pair production and bremsstrahlung until the energy falls below the interaction threshold.

3.1.2 The Hadronic Component

The hadronic component is generated when prompt protons, neutrons, or pions interacting with atmospheric molecules. Their scattering products may contribute to other components within the shower, or induce additional hadron interactions. For example, the decay of neutral pions ($\pi^0 \to \gamma\gamma$) contributes to the electromagnetic component. Alternatively, the scattering products may interact with neighbouring molecules and produce additional showering events.

The probability that a particle decays or interacts with atmospheric nuclei depends on both the particle's energy and the atmospheric density. This energy dependence arises from the relativistic Lorentz factor. For example, a 1 GeV muon will have a Lorentz factor of $\gamma = E_\mu/m_\mu c \sim 10$. This corresponds to a decay length of about $d_\mu = \gamma\tau_\mu c \sim 6\,\text{km}$. Alternatively, if the atmosphere is less dense, the hadron (or muon) is less likely to interact with neighbouring molecules, and the probability for decay increases.

3.1.3 The Muonic Component

Parent mesons, either pions or kaons, may decay into high-energy muons. This typically occurs approximately 15 km above the ground. The meson decay channels that significantly contribute to the overall background spectrum, and their respective decay probabilities, are summarized below.

$$\pi^\pm \to \mu^\pm \nu_\mu, \;\; \sim 100\%$$
$$K^\pm \to \mu^\pm \nu_\mu, \;\; \sim 63.5\%$$

Additional contributions arise from higher-order kaon interactions. These interactions typically do not contribute significantly to observations performed deep underground; however, they contribute to the muon flux observed at Earth's surface [37].

$$K^+ \to \mu^+ + \pi^0$$
$$K^0 \to \pi^+ + \pi^-$$

The muonic component of the shower is deeply penetrating and represents a major backgrounds for experiments deep underground. At the surface, the muon has less opportunities to generate additional hadron showers through spallation; however, the arising cosmic neutrons are detectable at the surface. In fact, cosmic neutrons represent the majority of background events observed in PROSPECT [4]. Muon-induced cosmic neutrons are the primary focus of this work, and are discussed in more detail in section 3.4.

3.2 Muons Through Matter

Much like other charged particles, muons lose energy through bremsstrahlung, radiative processes, and ionization. The dominant interaction is, however, determined by the kinetic energy of the incident particle and the size of the target [9]. For relativistic particles, excluding electrons, the energy loss interactions are ionization and atomic excitations. Moreover, Groom and Klien argue that, for charged particles, radiative effects dominate at high energies [9]. In fact, radiative effects dominate the interactions of cosmic rays.

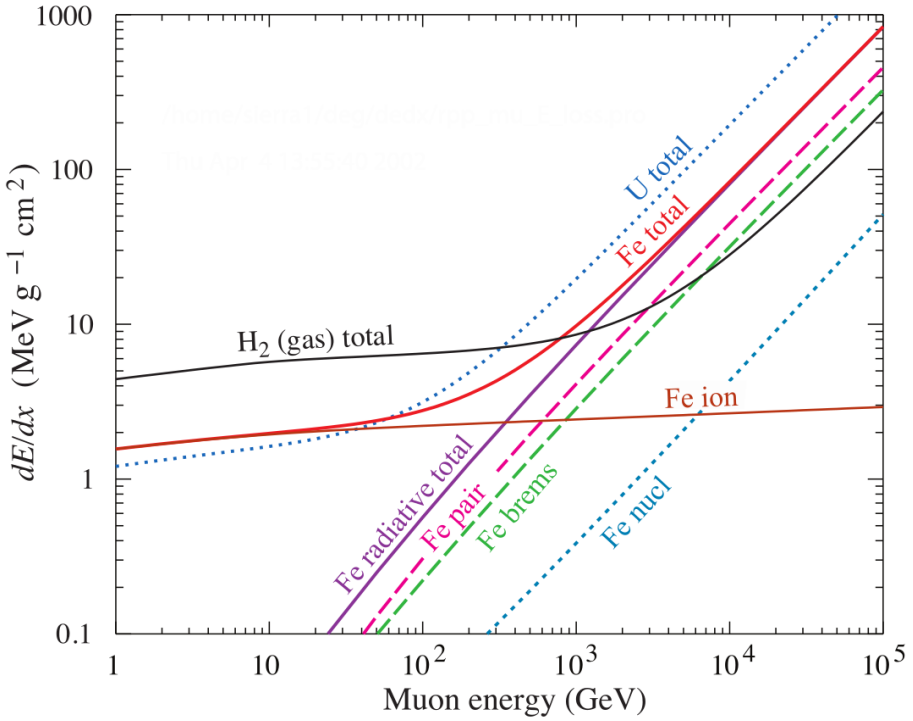

Figure 3.2: The muon energy loss per unit length is depicted for hydrogen gas, uranium and iron. This figure, taken from [9], also includes $e^- e^+$ pair production, bremsstrahlung, and nuclear interactions.

Figure 3.2 depicts the energy lost by a muon through different materials. Radiative effects dominate at larger energies beyond 1 TeV in hydrogen and at lower energies for materials with higher electron densities. In general, the average energy loss of a minimum ionizing muon through the liquid scintillator is approximately 2.5 MeV $g^{-1}cm^2$. Thus, muons are easily identified in liquid scintillators as trails of high-energy ion de-excitations.

The Bethe-Bloch formula, given in equation 3.1, describes the expected energy loss of heavy charged particles as they traverse a material. The maximum recoil energy transferred to an electron is denoted by W_{max} and is defined in 3.2. At large energies, this parameter introduces a minor dependence on incident particle mass M; however, the Bethe-Bloch equation is mostly dependant on the relativistic parameter β and charge number z.

$$-\left\langle \frac{dE}{dX} \right\rangle = \frac{Z}{A}\frac{Kz^2}{\beta^2}\left[\frac{1}{2}\ln\frac{2m_e c^2\beta^2\gamma^2 W_{max}}{I^2} - \beta^2 - \frac{\delta}{2}\right] \tag{3.1}$$

The constant K has a value of $0.307075\,\mathrm{MeV\,cm^2\,mol^{-1}}$ and I is the mean excitation energy. Additional information about the density correction term δ, inclusions of multiple Coulomb scattering, and the Bragg summation for mixtures and compounds can be found in [9].

$$W_{max} = \frac{2m_e c^2\beta^2\gamma^2}{1 + 2m_e/M\gamma + (m_e/M)^2} \tag{3.2}$$

Underground experimenters are often insensitive to the dominant cosmic interaction mechanisms observed at the surface. The average muon rate observed at Earth's surface is reported as $\sim 1/\mathrm{cm^2/s}$ with an average energy of ~ 4 GeV. Ignoring atmospheric and geographic variations, experiment located at Earth's surface experience additional low-energy components of the cosmogenic flux than underground detectors. At large depths underground, low-energy muon interactions become less important.

Experiment	Depth (m.w.e)	Average Muon Rate ($\mathrm{m^{-2}s^{-1}}$)	Average Muon Energy (GeV)
(-)	0	1.0×10^{-4}	4
Double Chooz [36]	~ 120	3.64 ± 0.04	22.3 ± 4.8
	~ 300	0.700 ± 0.005	46.0 ± 10.0
Daya Bay EH1 [12]	~ 250	1.16 ± 0.11	37 ± 3
Daya Bay EH2 [12]	~ 265	0.86 ± 0.09	41 ± 3
Daya Bay EH3 [12]	~ 860	0.054 ± 0.006	143 ± 10
CJPL [15]	~ 6720	$(2.0 \pm 0.4) \times 10^{-6}$	(-)

Table 3.1: The average muon rate and energy observed at different depths is summarized. The data was taken from Double Chooz near and far detector [36], the three observation sites at Daya Bay [12], and the China JinPing underground Laboratory [15].

Table 3.1 summarizes the observed muon rate from different underground detectors including the Double Chooz [36], Daya Bay [12], and the China JinPing underground Lab-

oratory [15]. The experimental depth is traditionally described in terms of water equivalent meters (m.w.e) where an experiment residing at 1000 m.w.e underground experiences the same shielding from cosmic events as an experiment submerged by 1000 m of water. The CJPL experiment, for example, resides 2400 m underground and is considered one of the deepest underground laboratory in operation. As a result, they experience an average muon count rate of 61.7 ± 11.7 muon events $/\mathrm{m}^2/\mathrm{year}$.

3.3 Muon Decay

Muon decay in free flight is often cited as a probe into fundamental physics. The interaction is free of any hadronic components; therefore, it may be used to determine leptonic coupling within weak interactions [10]. Muon decay is described by the purely leptonic interaction in equation 3.3 along with its conjugate.

$$\begin{aligned} \mu^+ &\rightarrow e^+ + \nu_e + \overline{\nu}_\mu \\ \mu^- &\rightarrow e^- + \overline{\nu}_e + \nu_\mu \end{aligned} \tag{3.3}$$

The decay rate follows an exponential probability with a known decay time of $\tau_{\mu^+} = 2197.03\,\mathrm{ns}$ taken from TRIUMF [55]. This is typically considered the most accurate measurement of the muon lifetime in free flight. Furthermore, from relativistic kinematics, the decay products has a known energy range. Michel electrons are relatively easy to identify in the liquid scintillator due to their distinctive energy range and PSD parameter.

$$0.511\ \mathrm{MeV} \leq E_{michel} \leq 52.8\ \mathrm{MeV}$$

The decay of negatively charged muons is more complicated. If a negative muon loses enegy within a material, it may decay during its flight or become intertwined with the attractive Coulomb potential of a target nucleus. Estimating the number of muonic atoms formed in this manner is nontrivial in mixtures due to possible impurities. The X-rays released as the muon cascades to the 1s ground state are detectable; however, they may excite neighbouring Auger electrons before the muon decays in orbit. These occurs within a few nanoseconds of each other; however, due to the limiting time scale of most counting experiments, these processes cannot be resolved and are observed simultaneously.

Due to the overlap between the muon and the valence electrons, the lifetime of the muon is modulated. The decay rate in orbit slows due to the energy loss of the bound muon; however, the decay probability increases because the produced electron experiences

the same binding interaction as its parent [56]. The overall deference between the decay rate arises from the time dilation experienced through the motion of bound muons. For known nuclear potentials, the muon lifetime can be calculated by evaluating the overlap between the radial wavefunctions of the muon and electron bound in the 1s ground state [56, 57].

3.4 Muon-Induced Neutrons

Although the total neutron yield from cosmic events has been measured by a variety of experiments [13, 29–33], different muon rates and energies give rise to disagreements in the literature. Furthermore, the theoretical yield [27, 28] is derived using varying spectrum assumptions; therefore, the limited experimental measurements of the neutron spectrum are scarcely reproduced through calculations. As a result, the cosmic neutron yield, energy spectrum, and multiplicity remains controversial within the low background particle physics community. The following section will describe how the cosmic neutron yield is calculated as well as outline the neutron production mechanisms that occur within PROSPECT.

3.4.1 Muon Capture

After cascading to the ground state, the muon orbital radius becomes comparable with the nuclear radius. Furthermore, negatively charged muons may become trapped within the nucleus under the attractive Coulomb potential. The nucleon interaction that governs this process is given in equation 3.4. This processes may result in excited isotopes releasing additional neutrons into the active volume. The muon capture excitation energy is between 10 and 20 MeV; however, the binding energy of a nucleon is approximately 8 MeV.

$$\begin{aligned} \mu^- + p &\rightarrow n + \nu_\mu \\ \mu^- + (A, Z) &\rightarrow (A, Z-1) + \nu_\mu \end{aligned} \tag{3.4}$$

Since the lifetime of the negative muon is coupled between decay and capture, the effective rate is the sum of the two reactions. Since these effects are difficult to uncouple, the effective lifetimes is typically reported by experiments. Table 3.2 list the muon lifetimes observed on isotopes present within the PROSPECT antineutrino detector.

$$\Gamma_{tot} = \Gamma_{decay^-} + \Gamma_{cap} \tag{3.5}$$

$$\frac{1}{\tau_{tot}} = \frac{1}{\tau_{decay^-}} + \frac{1}{\tau_{cap}} \tag{3.6}$$

The fraction of decays verses captures depends on the size of the atomic nucleus due to the large mass of the muon. Within the 1s state, the muon mean square orbital radius is approximately equal to the nuclear radius [10]. The decay fraction is proportional to the overlap between the muon and the nucleon, and the probability of finding a muon in the nucleus increase with atomic number Z. This results in a Z^4 dependence.

Z	Element	Mean Lifetime (ns)	$\Gamma_{tot} \times 10^3$ (s^{-1})
	μ^+	2197.03(4)	455.16
1	^{1}H	2194.90(7)	0.450(20)
	^{2}H	2194.53(11)	0.470(29)
3	^{6}Li	2175.3(4)	4.68(12)
6	^{12}C	2028(2)	37.9(5)
7	^{14}N	1919(15)	66(4)
8	^{16}O	1796(3)	102.5(10)
	^{18}O	1844(5)	88.0(14)
82	Pb	74.8(4)	12985(70)

Table 3.2: The mean muon lifetime and total capture rate for target nuclei relevant to the PROSPECT active volume and shielding are summarized. The results are taken from [10] and their respective references.

Muon lifetime experiments are rightly performed on pure targets because determining the total lifetime of a muon in an impure mixture is nontrivial [10]. In this case, with a fixed ratio of positive and negative muons, experiments must be validated by comparing results from other analyses.

3.4.2 Neutron Spallation

Spallation, defined as the exchange of a virtual photon between the muon and a target nucleus, is one of the least understood cosmic-induced neutron production mechanisms [58]. Consequentially, it is the source of computational discrepancies in the neutron spectrum and multiplicity.

$$\sigma_{\mu N} = \int \frac{n_\gamma(\nu)\sigma_{\gamma N}^{virt}(\nu)}{\nu} d\nu \tag{3.7}$$

A nucleus may enter an excited state through the exchange of a virtual photon. The delayed de-excitation may free a neutron from it's bound state. Taken from [27] and [58], the cross section used to quantify this interaction is given in equation 3.7 with the associated Feynman diagram in figure 3.3.

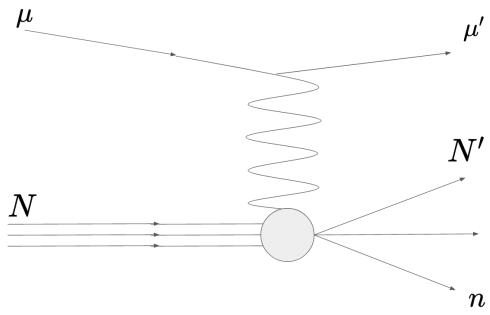

Figure 3.3: The Feynman diagram of muon spallation is illustrated.

The virtual photon spectrum $n_\gamma(\nu)$ depends on the energy lost by the muon ν. Furthermore, the interaction cross section $\sigma_{\gamma N}^{virt}(\nu)$ is approximated using the similarities between high-energy field excitations and real particles. This equivalent photon approximation, sometimes referred to as the Weizsäcker-Williams approximation, is only valid above 300 MeV when the energy of the virtual photon becomes comparable with the momentum of the muon. If the differential cross section is known, the spectrum of the virtual photon may be derived by integrating across the solid angles.

$$\int d\Omega \times \frac{d\sigma_{\mu N}}{d\Omega dE} = \frac{n_\gamma(\nu)\sigma_{\gamma N}^{virt}(\nu)}{\nu} \tag{3.8}$$

The virtual photon spectrum introduces a major discrepancy between experiments because of its dependence on the average energy of the muon. This, in turn, depends on the depth of the detector from the surface. The spectrum, taken from [27], is given in equation 3.9. For a muon of mass m, the quantities $E(E')$ and $P(P')$ describe the energy and momentum before and after the collision, and α is the fine structure constant.

$$n_\gamma(\nu) = \frac{\alpha}{\pi}\left[\frac{E^2+E'^2}{P^2}\ln\frac{EE'+PP'-m^2}{m\nu} - \frac{(E+E')^2}{2P}\ln\frac{(P+P')^2}{(E+E')^2\nu} - \frac{P'}{P}\right] \tag{3.9}$$

3.4.3 Fast Neutrons

Fast neutrons occur when a spallation event carries away an abundance of kinetic energy after the interaction. The resulting neutron thermalizes through sequential collisions before capturing. Fast neutrons may be produced as a result of photo-nuclear reactions from muon-induced electromagnetic showers, elastic scattering between the muon and nuclei, or any trialing neutron secondary events after these processes [27].

The proton recoil events may occur within a time scale of 10 ns from the prompt muon. For the purposes of most counting experiments, this is instantaneous with respect to the incident muon. The prompt recoil and delayed capture events overlap the IBD selection chriteria and mimic the desired signal. The initial recoil is, however, easily removed from the primary oscillation and spectrum analysis by vetoing events observed after the prompt muon. At PROSPECT, if the primary muon is detected, trailing events up to 200 μs are ignored [4]. This cosmic ray veto also removes most delayed capture events.

For many experiments, including PROSPECT, vetoing will not remove all fast neutrons. The secondary neutron may traverse several meters before thermalizing. This is particularly problematic if the primary muon does not deposit energy within the active volume. It is this reason that many underground detectors such as Double Chooz [46] and Daya Bay [1], incorporate external muon systems for their veto's. For example, Daya Bay identifies muons using large Cerenkov radiation detectors outside of their active volume. If the muon is successfully identified, the veto is applied. PROSPECT, however, is at the full mercy of cosmic interactions through the entire range of possible energies and momenta. The cosmic background observed in PROSPECT is dominated by fast neutrons arising from the hadron component of the air shower.

3.4.4 Cosmogenic βn - Emitters

Beyond the initial fast neutrons produced by cosmic muon spallation, a far more interesting background arises if the target nucleus survives the collision. the remaining nucleus may become unstable and decay several seconds later. These isotopes may contribute to the overall accidental background rate.

The isotopes ^{9}Li and ^{8}He are particularly nefarious because they produce both a prompt beta and delayed neutron capture signature. Consequentially, these events are often referred to as βn-emitters, and their decay chains are summarized in figure 3.4. With a probability of 49.2%, the isotope ^{9}Li decays to the ground state of ^{9}Be. The remaining

50.8% of the decays arrive at an excited state. With a half-life of $\tau_{Li} = 178\,\text{ms}$, the expected endpoint of this decay series is a Q-value of 13.61 MeV. ^{8}He, on the other hand, has a half life of $\tau_{He} = 117.5\,\text{ms}$ and a Q-value of 10.65 MeV.

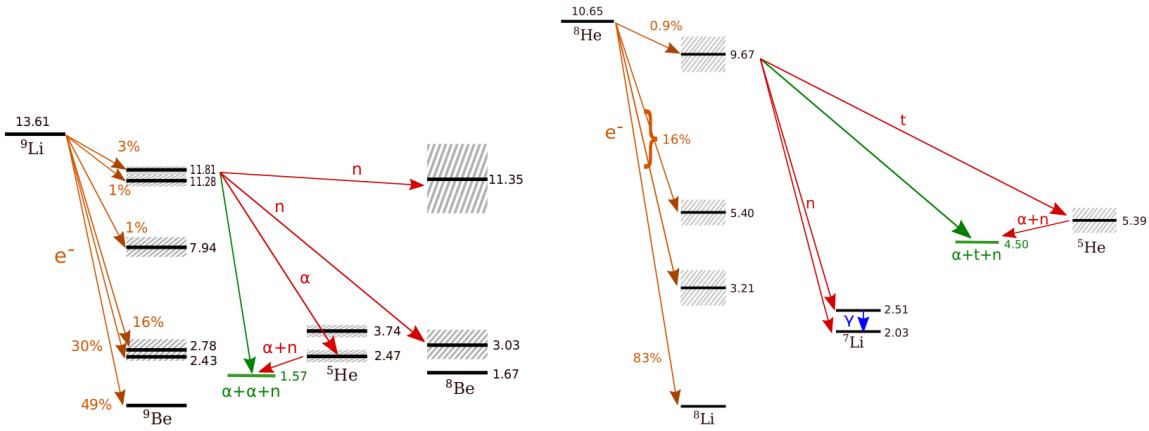

Figure 3.4: The decay chains for the βn-emitters ^{9}Li (left) and ^{8}He (right) into their respective daughter nuclei are visualized above. This figure was taken from [14].

These events are, however, notoriously difficult to measure within surface detectors. The subset of high-energy spallating muons must be sufficiently isolated from the remaining sample; however, the delayed neutron capture event is indistinguishable from other neutron backgrounds. Underground detectors, such as KamLAND [32] exploit the unique Cherenkov radiation signature of the incident muon to isolate their measurements. Other experiments, such as Double Chooz [14], apply a Bayesian hypothesis test to each of their IBD candidates to determine if it is likely caused by a correlated background.

PROSPECT is not as luxurious. The incident muon candidate should contain both the muon track and one or more proton recoil events. Unfortunately, this unique signature is too difficult to isolate using the current statistical algorithms and tracking routine described in section 5. In addition, an abundance of overlaping signals were observed within the relatively large time coincidence. Thus, the neutron background from muon-induced radioisotopes is largely excluded from this analysis. The expected neutron yield from ^{9}Li is, however, easy to estimate. An internal collaborator within the PROSPECT collaboration [16] extrapolated the measured yield from the 20 ton EH1 detector at Daya Bay [1] to the appropriate active volume within PROSPECT. From the decay of ^{9}Li, PROSPECT expects approximately 8.6 neutron events per day.

3.4.5 Total Neutron Yield

As mentioned previously, the total cosmic-induced neutron yield Y_n is an area of contention within the low background particle physics community. Defined as the average number of neutrons produced per muon per material thickness, inconsistencies in models [27, 28] and disagreements between measurements [13, 29–33] have arisen.

One of the earliest theoretical neutron yield predictions was performed by Wang [27]. In their studies, an exponential dependant behavior on muon energy was found to be in good agreement with measured data. This relation was confirmed by Kudryavtsev [28]. In their work, however, a 10 to 15% deficit was found between the data and the neutrons produced by their FLUKA simulations. The neutron yield is, therefore, still a conundrum, yet additional measurements may aid in unravelling its secrets.

The discrepancies between experiments are caused by variations in muon rate and threshold energies, and the discrepancies in simulations are primarily caused by the different physical models describing the muon transport through rock. Consequentially, a measurement of the neutron yield performed at the Earth's surface may provide some clarity. The pulse shape and energy resolution techniques described in section 2.3 give PROSPECT its unique ability to distinguish particle events in spite of its minimalist overburden. Furthermore, since it resides on Earth's surface, backgrounds from surrounding radioactive sources, during a reactor-off period, are negligible.

The neutron yield is intrinsically related to the total muon-nucleon interaction cross section and the travel distance of the muon. Equation 3.10 describes the total number of neutrons in terms of the muon path length ℓ and neutron multiplicity f. Here, n_T is the number density of the material traversed by the muon, and A is its atomic mass. Together, they represents the number of target nuclei per unit length within the active volume.

$$\overline{N}_n = \ell n_T \langle f \sigma_{\mu N} \rangle = \ell \frac{\rho N_A}{A} \langle f \sigma_{\mu N} \rangle \tag{3.10}$$

Experimentally, the neutron yield represents the average number of neutrons produced per muon interaction, and it can be determined if the distance traversed by each muon is known.

$$Y_n = \frac{\overline{N}_n}{\ell \rho} = \frac{N_n}{L \rho} \tag{3.11}$$

Here, N_n represents the total number of neutrons produced by cosmic interactions, and L represents the total path length summed over every muon. This quantity, however introduces a large systematic uncertainty due to the detector's geometrical limitations and

from the inclusion of stopped muons. A detailed tracking routine, like the precision tracking routine suggested in appendix A, may resolve these issues. In its current state, however, the precision tracking routing over predicts the number of stopped muons by a factor 2. Instead, if the angular distribution of cosmic events is well understood, and the majority of cosmic neutrons are produced by high-energy through going muons, this quantity can be approximated by the average muon travel distance and total muon rate.

$$Y_n = \frac{1}{\overline{L}\rho}\frac{N_n}{N_\mu} \tag{3.12}$$

Since both N_μ and N_n represent the expected muon and neutron rates under ideal conditions, the measured rates must be scaled by their respective selection efficiencies $\epsilon_{\mu(n)}$. The efficiency is defined as the ratio of observed events to the total for a given particle species; therefore, it is largely dependent on how the candidate is selected as well as any systematic effects from the detector that would otherwise contaminate the sample.

It is assumed that the neutron multiplicity of each muon-nucleon event is 1. Under this assumption the total muon-nucleon cross section can be defined. By combining equation 3.11 and 3.10, the total cross section is given in equation 3.13.

$$\langle \sigma_{\mu N} \rangle = Y_n \frac{A}{N_A} \tag{3.13}$$

Previous studies have demonstrated that the expected neutron yield follows a power-law dependence on the average muon energy [13, 27]. This relationship is illustrated in figure 3.5. This global fit, taken from the Daya Bay collaboration [13], contrasts their results against other underground experiments.

$$Y_n\left(\overline{E}_\mu\right) = a\overline{E}_\mu{}^b \tag{3.14}$$

Parameter	Value
a	$(4.0 \pm 0.6) \times 10^{-6}\ \mu^{-1}\mathrm{g}^{-1}\mathrm{cm}^2$
b	0.77 ± 0.03

Table 3.3: The parameters for the neutron yield calculation are taken from [13].

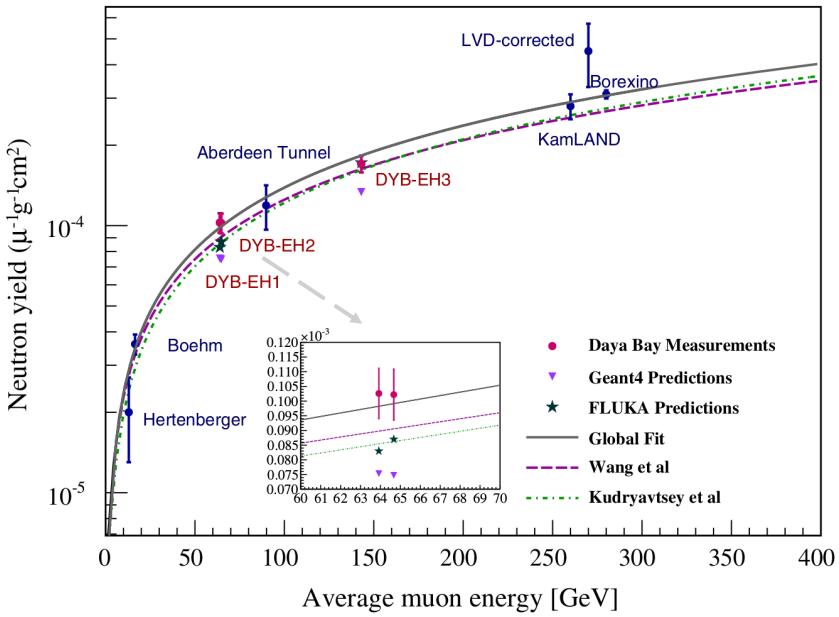

Figure 3.5: The theoretical neutron yield is contrasted against measurements from other collaborations. Taken from [13], Monte Carlo simulations from FLUKA and GEANT4 are included. The FLUKA predictions demonstrate a strong dependence on the muon energy. The dashed line and dash-dotted lines are predictions from Wang [27] and Kudryavtsey [28]. The solid line is a global fit that incorporates measurements from Hertenberger [29], Boehm [30], Aberdeen Tunnel [31], KamLAND [32] and Borexino [33]. The results from the three experimental halls from Daya Bay [13] are also included.

Using the global fit parameters summarized in table 3.3, the expected yield may be determined. With an assumed average muon energy of 4 GeV, the predicted neutron yield at the surface is calculated from the parameterization provided by the Daya Bay collaboration [13]. The expected yield in the PROSPECT experiment is $(11.63 \pm 2.00) \times 10^{-6}\ \mu^{-1}\mathrm{g}^{-1}\mathrm{cm}^2$.

Chapter 4

Monte Carlo Simulations

Named after the popular casino town in Monaco, the Monte Carlo method is an advantageous tool in particle physics. Invented by John von Neumann and Stanislaw Ulam [59], the Monte Carlo method can, in principle, predict the outcome of any probabilistic measurement. Since the problem of particle transport through matter contains many correlated degrees of freedom, it is often used to replicate the behavior of particle detectors.

The Monte Carlo method has 3 steps:

1. Construct the predictive model describing both the dependant and independent variables. These are often referred to as the input and predictor variables.

2. Using a well established probability distribution, generate the inputs over the possible domain. The probability distribution is defined using either historical observations of similar processes or a known mathematical model.

3. Perform a deterministic computation over the inputs and tabulate the results. This must be performed repeatedly in order to generate a representative sample.

If the simulation accurately replicates the behavior of the experiment, Monte Carlo methods may be used to define the particle identification criteria for observational measurements. Thus, this section focuses on the simulations used to identify muons and their correlated secondaries. It will begin by briefly describing the GEANT4 package including the cosmic ray and neutron generators. The cosmic ray generator is benchmarked against predictive muon flux models before the selection criteria are defined.

4.1 GEANT4

The Geant4 Monte Carlo simulation packages was developed by the European Organization for Nuclear Research (CERN) [18]. This toolkit provides an object-oriented framework for analyzers to replicate a variety of different physical mechanisms. Since its inception, GEANT4 has found far reaching applications in both the high-energy and nuclear physics community as well as astronomy and medicine.

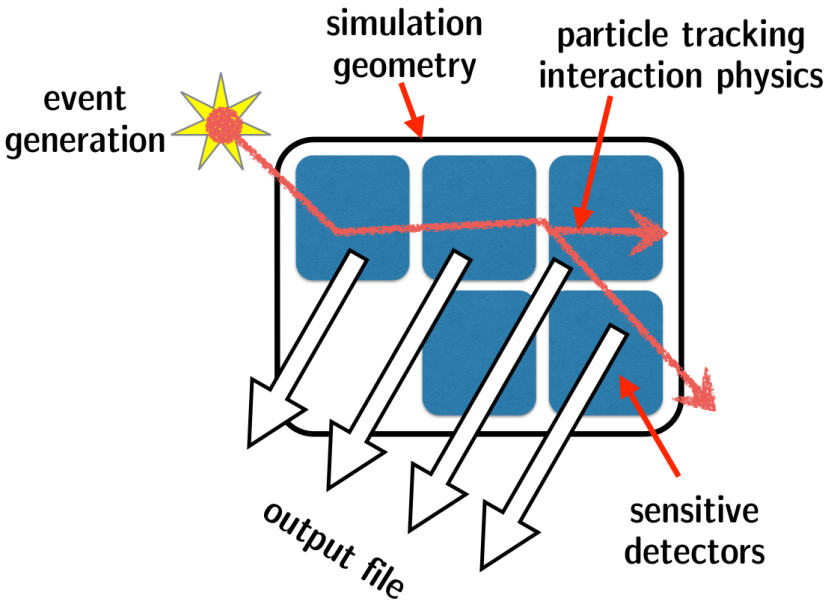

Figure 4.1: This GEANT4 analysis pipeline schematic is taken from [17].

GEANT4 uses a Runge Kutta integration method to solve the particle transport through the simulated volume. The particle track is projected into the next volumetric pixel by a predefined step size, and it is accepted if both the momentum and position are within a set threshold. At each step, a sampling computation determines if the current particle state vector should be modified. Thus, GEANT4 expects 3 inputs:

1. An appropriate particle generator,
2. A detailed geometric model of the active volume,
3. And a list of physical models that reflect the desired interactions.

The physics models used by the PROSPECT collaboration replicate the energy loss of charged particles through matter by bremsstrahlung and spallation. Electromagnetic interactions, as well as elastic and inelastic scattering on heavy isotopes, are also included in the model. Lastly, the decay of unstable particles and isotopes must be included in order to reflect the interactions of cosmic events. The detector geometry is generated to reflect the final PROSPECT antineutrino detector. Logical volumes describing all 154 segments and PMT housings, as well as support pinwheels and shielding, were generated. Additional information describing the simulated geometry and physics models can be found in [60].

4.2 Particle Generators

Originally benchmarked against observations from Rastin [19, 61], the Cosmic ray generator (CRY) is capable of replicating the low-energy component of the cosmic background spectrum. It, however, under predicts the cosmic neutron flux from external interactions near the PROSPECT detector. To compensate for this, the PROSPECT collaboration has developed a cosmic neutron generator derived from first principles. In this section, both generators will be described.

4.2.1 Muon Generator

CRY is a particle physics software library developed by Lawrence Livermore National Laboratory (LLNL). It relies on pre-computed data tables from a more complete MCNPX physics package to generate its cosmic flux [19]. Thus, a cosmic background spectrum containing kinetic energies and directions can be tabulated through GEANT4.

The CRY generator is capable of replicating the solar sunspot cycle and geomagnetic deflections. This is implemented by introducing a weighted sub-spectra [19]. Within the configuration file, the geographical and temporal settings were adjusted to replicate the conditions of HFIR at the beginning of the experiment. Using the enclosed PROSPECT geometry, a large simulation of 160 000 000 cosmic muons was generated to replicate the conditions of March 16, 2018. An elevation of 0 m above sea level with at latitude of 36° was used to generate particle cascade. The resulting simulated exposure time was approximately 3553.03 s. This simulation is recycled for later justification of the muon selection and tracking routines.

Although the generated spectrum has been benchmarked by Hagmann, Lange and Wright [19], further validation is necessary before CRY may be applied for event selec-

tion. Since the Monte Carlo method is used to test different particle selection and tracking methods at PROSPECT, the generator must be contrasted against a well established cosmic spectrum. A common muon intensity parameterization is given by Gaisser [38]. This model was, however, motivated using the meson interactions that dominate near the top of the atmosphere. As a result, it is only valid for high-energy muons with $E_\mu > 100\,\text{GeV}$ and with measured zenith angles near the vertical $\vartheta < 60°$ [1].

$$\frac{dN}{dE_\mu d\Omega}(E_\mu, \vartheta) = 0.14 E_\mu^{-2.7} \left(\frac{1}{1 + \frac{1.1 E_\mu cos\vartheta}{115 GeV}} + \frac{0.054}{1 + \frac{1.1 E_\mu cos\vartheta}{850 GeV}} \right) \text{cm}^{-2}\text{sr}^{-1}\text{s}^{-1}\text{GeV}^{-1} \tag{4.1}$$

Instead the Rena parameterization is used to validate the cosmic generator. Originally proposed by Bugaev [37], this model incorporates the total particle cascade throughout the atmosphere. The original parameterization describes the vertical muon intensity at Earth's surface and at shallow depths. The vertical muon intensity $I_v(E_\mu) = I_\mu(E_\mu, \vartheta = 0°)$ is well documented and has been experimentally validated by a variety of detectors since the 1980s [37]. Recently, Reyna [34] has extended this paremeterization to other incident angles by introducing a cubic angular dependent scaling factor. The parameterization is given in equation 4.2.

$$\begin{aligned} I_\mu(E_\mu, \vartheta) &= (\cos^3 \vartheta) I_v(E_\mu) \\ I_v(E_\mu) &= c_1 E_\mu^{-\left(c_2 + c_3 \log_{10}(E_\mu) + c_4 \log_{10}^2(E_\mu) + c_5 \log_{10}^3(E_\mu)\right)} \end{aligned} \tag{4.2}$$

Fit Parameter	Value
c_1	0.00253
c_2	0.2455
c_3	1.288
c_4	-0.2555
c_5	0.0209

Table 4.1: The fit parameters for the Reyna model [34] are summarized.

The cosmic ray generator is also contrasted against the phenomenological model proposed by Smith and Duller [35]. Inspired by Barrett's explanation of decay and absorption phenomena at high altitudes [63], Smith and Duller constructed their phenomenological

[1] By incorporating the Earth's curvature, the Gaisser model has been extended to lower energies [62].

muon intensity model [35] from pion interactions in the upper atmosphere[2]. It calculates the number of cosmic muons produced at energy E_μ per solid angle measured at atmospheric depth y_0 and density ρ_0. Since it only includes interactions from pions with absorption mean free path λ_π, rest mass m_π, and lifetime τ_0, it is expressed in terms of the pion energy E_π[3]. Their phenomenological model is given in equation 4.3.

$$\frac{dN}{dE_\mu d\Omega}(E_\mu, \vartheta) = \left(\frac{AE_\pi^{-\gamma} P_\mu \lambda_\pi b j_\pi}{E_\pi \cos\vartheta + b j_\pi}\right) \text{cm}^{-2}\text{sr}^{-1}\text{s}^{-1}\text{GeV}^{-1} \tag{4.3}$$

Unlike the Rena parameterization, this model has only 2 fitting parameters. The fitting parameters are the spectral amplitude $A \sim 2.5 \times 10^{-3}$ and the differential spectral index $\gamma \sim 2.7$. The factor P_μ is the survival probability that a muon, with zenith angle ϑ reaches the ground. Since the atmosphere is approximated as an isothermol exponentially decaying body, the parameters $b = 0.771$ and $j_\pi = y_0 m_\pi c/\tau_0 \rho_0$ are introduced to correct for atmospheric distortions at high elevations.

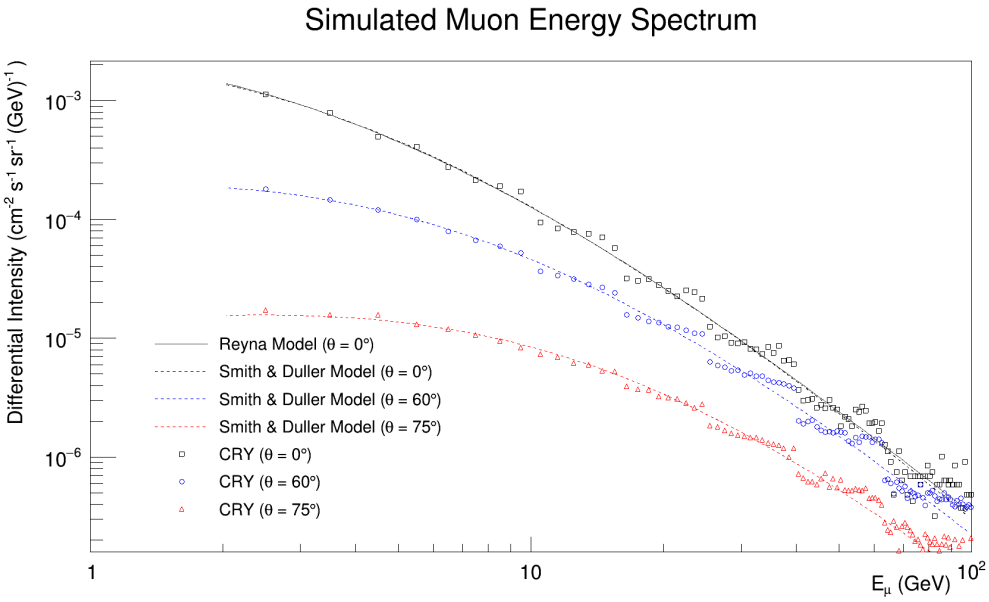

Figure 4.2: A simulation of the cosmic muon spectrum observed at ground level was generated using CRY. Different angles were selected using the generated primary event table, and generated spectrum was fit to the Reyna [34] and phenomenological model [35].

[2] As introduced in section 3.1.2, the production of muons is related to the decay time of its parent.

[3] The Smith and Duller model has since been extended to incorporate muon production from kaons [61].

Figure 4.2 displays the resulting spectrum from events within 5° of various angles measured from the vertical. Since the simulation also provides tracking information through the active volume, the appropriate normalization constants were computed. A method of least squares was used to fit the simulated spectrum to the Reyna and phenomenological model. The results are summarized in table 4.2 and 4.3 respectively.

Parameter	Theoretical Value	Fit Result
c_1	0.0025	$(2.18 \pm 0.01) \times 10^{-3}$
c_2	0.2455	0.35 ± 0.05
c_3	1.288	0.95 ± 0.07
c_4	-0.2555	-0.16 ± 0.43
c_5	0.0209	-0.03 ± 0.01

Table 4.2: The Results of the least squares fitting method between the vertical muon spectrum and Reyna model [34, 37] are contrasted.

Despite the fit parameters having similar orders of magnitude with the expected result, the Reyna parameterization is only partially successful in reflecting the simulated spectrum. The original parameterization from Bugaev [37] was determined over different energy ranges, Reyna argues that their improved parameterization should be appropriate for events within $1\,\text{GeV} < E_\mu < 2000\,\text{GeV}$. This fit yields a χ^2/ndf of 808.109/93. The poor fit quality may be due to the relatively small simulated energy domain. Alternatively, PG4 only records primary events if they interact with the active volume during their transport. The cosmic background spectrum is attenuated by the geometrical properties of both the shielding and the active volume; therefore, the rectangular shape of the detector may be introducing edge effects. Thus, the resulting steps in the energy spectrum degrade the quality of the fit at high energies.

Angle	χ^2/ndf	Fit Results	
		$A \times 10^{-3}$	γ
0°	821.674/96	2.285 ± 0.035	2.638 ± 0.006
60°	2598.15/96	2.195 ± 0.022	2.732 ± 0.003
75°	581.295/96	2.503 ± 0.077	2.944 ± 0.009

Table 4.3: The Results of the least squares fitting method between the simulated muon spectrum and phenomenological model [35] are contrasted.

The Smith and Duller model possesses similar behavior across the three chosen angles. The minor deviations in amplitude may be the result of improperly constructed flux and solid angles; however, the deviating behavior at large angles is not surprising. The parameterizations at shallow angles is expected to break down since the original model does not consider the curvature of the Earth. In addition, the geometrical distortions are more apparent in the 60° measurements than the others, resulting in a $\chi^2/\text{ndf} > 10$. This distortion is expected to increase for more edge sensitive measurements closer to 45°. For further model validations, these geometrical distortions may be removed by replacing the PROSPECT geometry with a perfect sphere or disk.

The vertical muon flux is more accurately described by the Reyna model than the Smith and Duller model. Unfortunately, the lack of statistics beyond 100 GeV, as well as the geometrical distortions, complicates this comparison. Since radiative effects dominate the energy loss of charged particles at large energies, this may also explain the apparent lack of neutron statistics produced by CRY.

Regardless, the fit parameters suggest that, within the limited resolution of the experiment, CRY may be used as a cosmic event generator. Since PROSPECT does not measure the kinetic energy of incident particles directly, additional benchmarking may be performed using other energy sensitive distributions. A comparison between the rate of stopped muons and correlated high-energy betas using simulations and early data provided by the PROSPECT collaboration is found in section 6.4.1 and 6.4.4 respectively. A comparison between the observed angular distributions is provided in section 5.3.1.

4.2.2 Neutron Generator

Since CRY underestimates the cosmic neutron yield, the PROSPECT collaboration has developed their own unique cosmic neutron generator. This generator more accurately reflects the behavior of fast neutrons measured at HFIR. Events are generated in the upper atmosphere with a $\cos^{2.5}\vartheta$ weighted *quasi-Lambertian* angular distribution. Moreover, it has been extensively tested against the proposed Goldhagen spectrum [64]. In this analysis, the neutron generator is used to determine the cosmic neutron selection efficiency.

4.3 PROSPECT-G4 Simulation Pipeline

The PROSPECT collaboration has developed a method to match observed data with a simulated response in order to determine the appropriate energy and pulse shape. It

is also used to convert simulations into representations of physical data. The complete routine, called PROSPECT-G4 (PG4), groups the output in the hdf5 table into a format that mimics real measurements. Thus, the simulations can be analysed using the same methods as measured data. The complete analysis pipeline will now be described.

After GEANT4 has sampled from the desired probability distributions, events are sorted into 3 categories in the output table. The first table describes the primary events produced from the particle generator. The other two describe ionizing events or neutron recoil events. These tables, referred to as *truth tables*, contain information about the particle transport. It also contains information about the logical volume that contained the event. The two most important quantities in these tables are, however, the particle identification tag (PID) and the event number. The later is propagated thought the entire analysis pipeline; therefore, it is used to determine correlations between the observed response and the primary events. On the other hand, the PID is used to determine the particle species within a cluster of events[4].

Next, PG4 must apply the appropriate detector response to each event. This is done by assigning the appropriate signal-to-energy conversion and PSD scaling. The energy lost by the events at each tracked step is converted to a detector response through Birks' Law [65]. This non-linear relationship between deposited energy and light production reflects the behavior of the liquid scintillator. Additional information about light yield simulations and detector response functions can be found in [60].

Figure 4.3 demonstrates how PG4 attempts to replicate the behaviour of observed data. It even replicates the clipping behavior observed beyond 20 MeV. The upper edge of the curve reflects the position dependant clipping behavior of the near PMT, while the lower edge reflects the far PMT. The simulation, however, does not capture the smeared behavior near 30 MeV in 4.3b. These events do not occur in the simulation; therefore, they are either independent of incident cosmic muons or require the inclusion of more complex spallation theory to replicate them appropriately. Regardless, this response is sufficient for the resolution of the PROSPECT experiment despite its imperfections.

Once the detector response has been generated, the simulation can be treated like real data. In this work, this procedure is used to contrast the simulated behavior of the muon selection and tracking routine against observed data. The muon tracker borrows techniques from computer vision, and it must be validated before it can be applied to real observations. Further details on PROSPECT's muon tracking capabilities are describes in section 5. The muon and correlated events selection criteria are described in section 4.4.

[4]Anti-matter equivalent events are identified using the sign of the PID. Positrons and anti-muons have PID tags of +11 and +13 respectively.

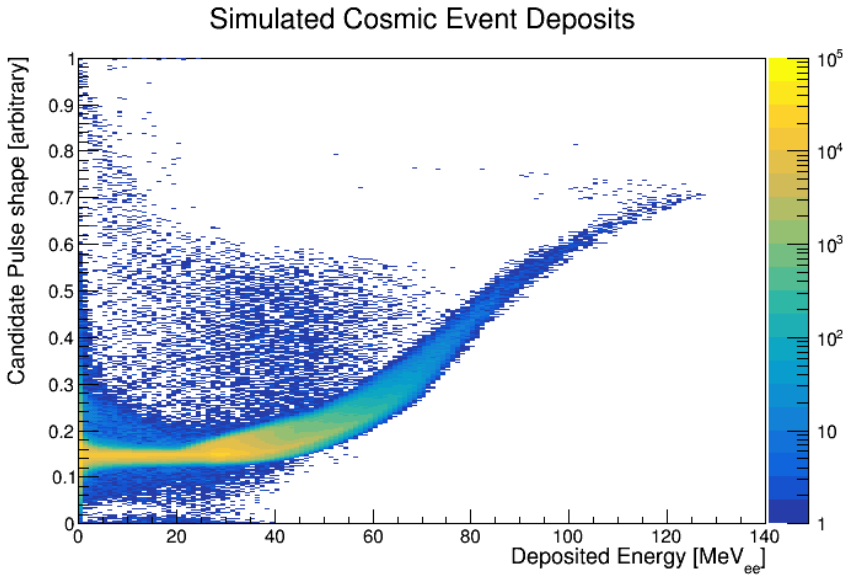

(a)

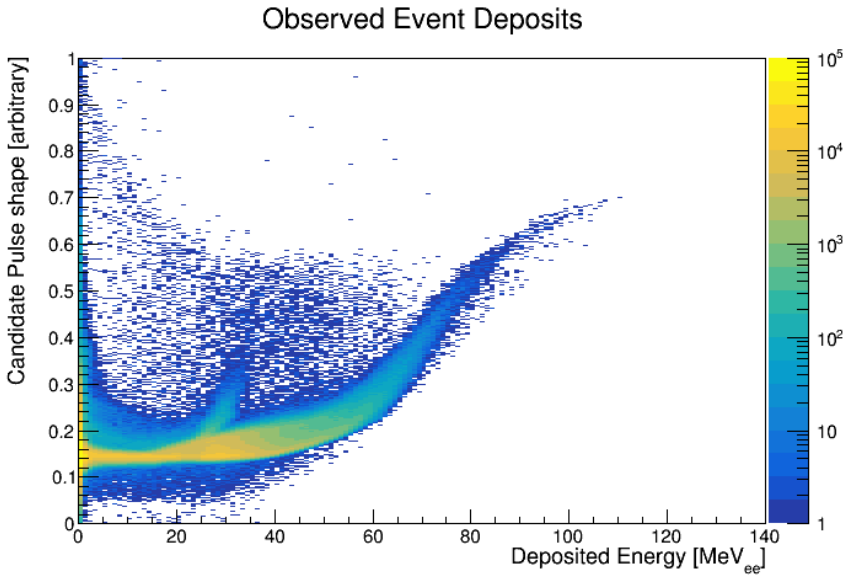

(b)

Figure 4.3: The detector response has been applied to a simulation of cosmic muons in 4.3a and calibrated PROSPECT data from early March 2018 during a reactor-off period in 4.3b. Both simulation and data have an approximate exposure time of about 1 hour.

4.4 Event Selection

Simulations may be used to prototype analyses and event selection criteria if they are accurate representations of the data. This is done by matching the post detector response clusters to the events in the truth table. The detector response clustering is handled through the analysis pipeline; however, events in the generated truth tables were reconstructed in a post processing routine.

Within the generated truth tables, ionizing and neutron recoil events are grouped together using their event numbers. Additionally, grouped events must be within 20 ns of each other. Once events are clustered together, they are matched to their PG4 response counterparts using their average arrival time and event numbers. Events with fictitious volume indices are ignored, and the particle species is assigned using the PID tags. Events with PID tags of ± 13 are of particular interest to this analysis; if this value is found among the cluster, it is labeled as a muon. Otherwise, it is either a beta or neutron recoil event.

This matching routine is, however, imprecise. It assumes that all events within a cluster originate from the same primary event. This does not accurately reflect the behavior of data observed by the PROSPECT collaboration where uncorrelated events may accidentally become clustered together. Furthermore, if multiple simulated clusters are generated with the same event number, it becomes difficult to match them with there detector response counterparts. In this case, the relative time between the clusters is used. As a result, some clusters cannot be associated with a particle species.

Figure 4.4 depicts the calibrated energy deposits of different events within simulated cosmic showers. In addition tabulated number of events is given in table 4.4. The green curve depicts the deposited energy of correlated betas, and it is consistent with the kinematics of muon decay. The red curve in figure 4.4a shows the calibrated energy of neutron events distributed around the two prominent capture peaks in PROSPECT.

Particle species	Tabulated Amount	
	Counts	Percentage
Muons:	173611	86.86%
Betas:	19103	9.54%
Neutrons:	511	0.26%
Missing Events:	7062	3.53%

Table 4.4: The amount of events identified in the simulations is summarized.

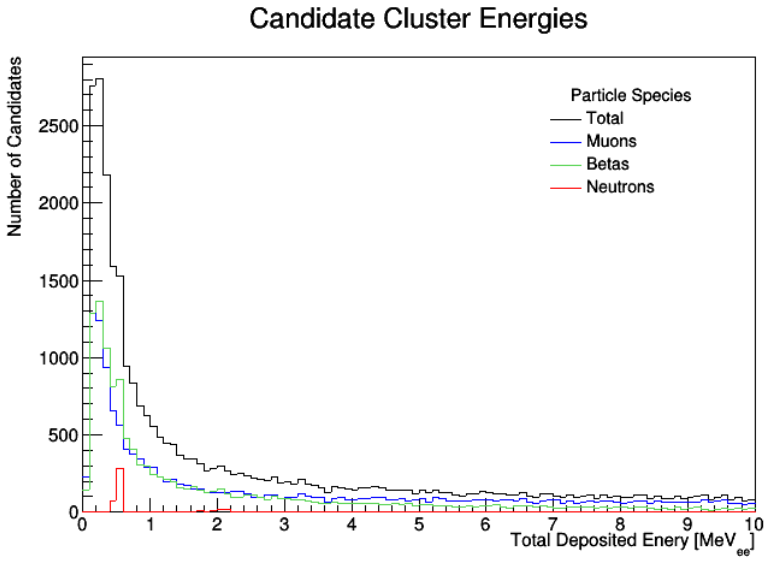

(a)

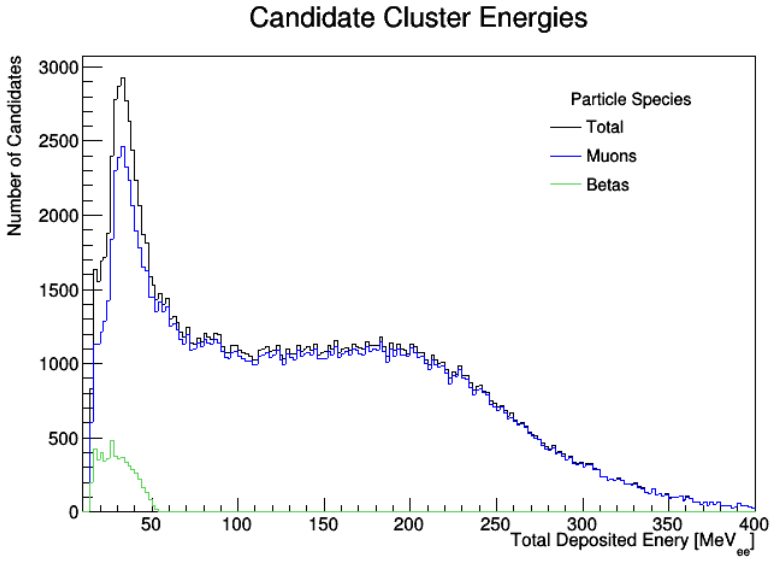

(b)

Figure 4.4: The detector response of simulated cosmic air showers is divided between low-energy (a) and high-energy events (b). The muon decay products (green) are distributed between 0 and 60 MeV. The clipping effect dominates the muon events (blue) beyond 40 MeV. The majority of the low-energy neutron events (red) are distributed around the lithium capture peak (0.55 MeV) and the hydrogen capture peak (2.2 MeV).

4.4.1 Muon Selection Criteria

In order to successfully identify correlations between the prompt muon and their secondaries, the appropriate subset of the data must be isolated. In this case, the muon may traverse multiple segments and create a trail of ion de-excitation. For this analysis, at least 3 distinct cell deposits are required if the trajectory of the muon is desired. The muon is expected to deposit a large amount of energy into the detector unless it traverses the edge of the segments. Thus, this analysis will be concerned with the vetoing muons. These high-energy muons are more likely to result in local shower events; therefore, the muon will likely generate correlated neutrons.

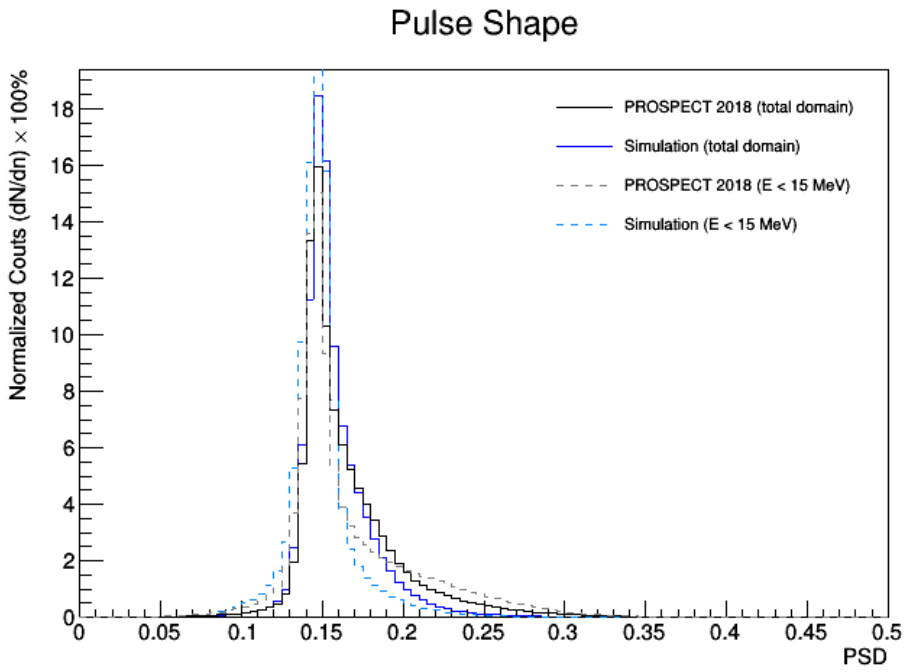

Figure 4.5: The PSD of the muon simulation (MC) is contrasted against measured data from early March of 2018 The behaviour above and below the clipping threshold is presented using solid and dashed lines respectfully. Below the 15 MeV threshold, a tail above the gamma band is visible. These are nuclear recoil events that must be removed.

Figure 4.5 contrasts the pulse shape parameter between simulations and measured data taken in early March 2018. These distributions are normalized to an area of 1 to allow for easier comparison. As mentioned in section 2.3.5, the pulse shape resolution between

neutron recoil and electron recoil events breaks down at large energies. A constraint on PSD can only be performed if fewer than 15 MeV is deposited into a single detector segment. This does not disrupt the primary IBD analysis; however, it will limit the detector's sensitivity to high-energy events. If a single energy deposit is fewer than 15 MeV, and it's within 2.5σ of the gamma band, it is considered for further analysis.

The energy of each cell deposition is highly correlated with position. If an event is centered inside a segment, a significantly greater amount of energy is deposited than events near the edges. As displayed in figure 4.6, the measurements are dominated by low-energy events. The data was taken during a reactor-off period; therefore, these are most likely cosmic secondaries. Theses low-energy events are distinct from the simulated muon sample; therefore, pulses below 0.2 MeV are ignored.

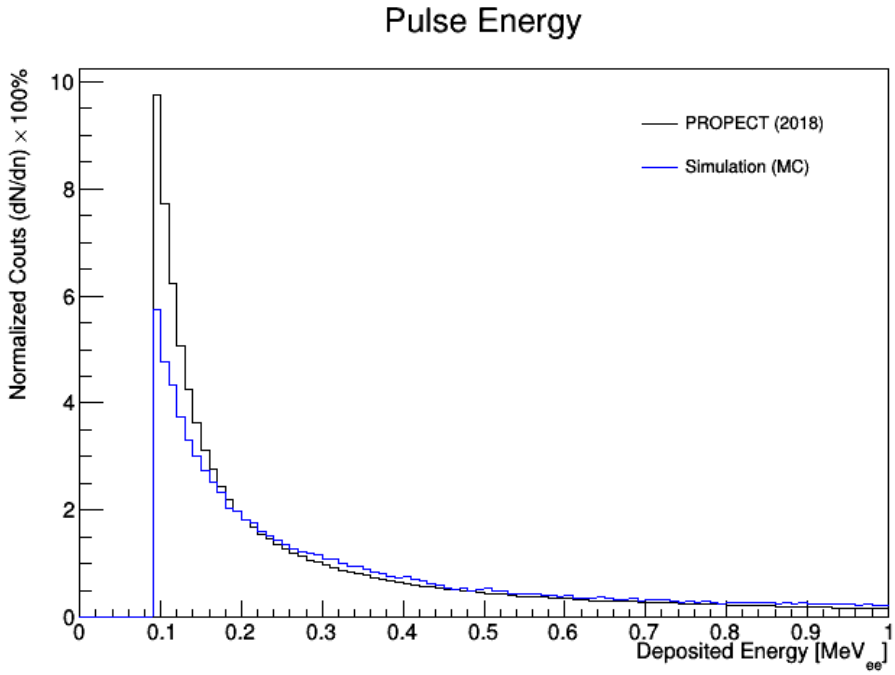

Figure 4.6: The energy deposits of pulses are contrasted between simulation and measurement. The observed data is dominated by events below 0.2 MeV.

Lastly, the position along the length of the segment is considered. Despite the total length of the PROSPECT detector exceeding 2.66 m, the active volume is constrained to 1.17 m. The remaining width is composed of the photo-multiplying tubes. Events that

occur inside the PMT housing have the potential to trigger short electromagnetic showers within the mineral oil. These events must be removed.

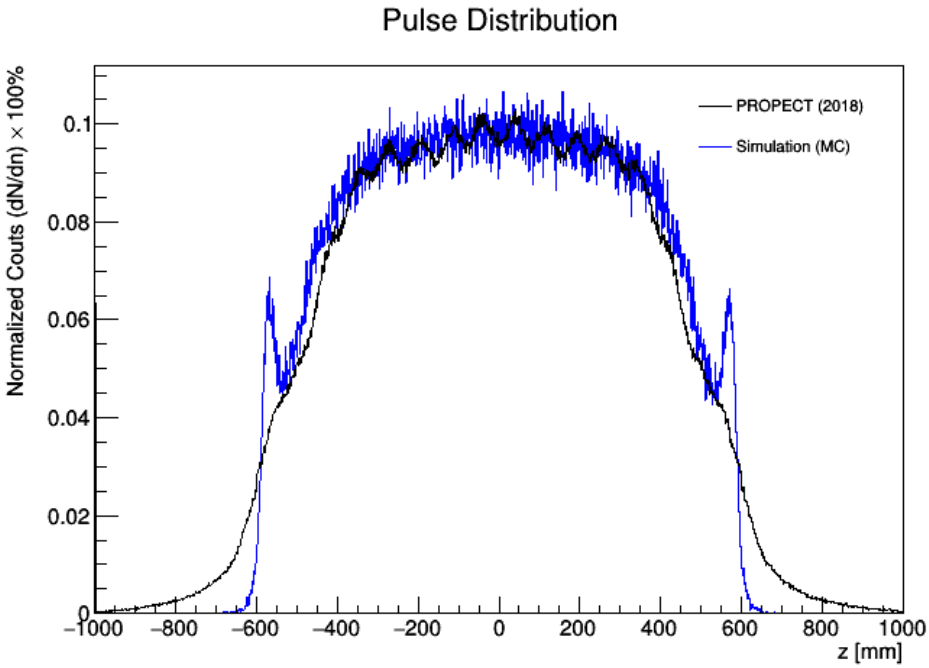

Figure 4.7: The position distribution of each cell deposit is contrasted between Monte Carlo simulations (blue) and measurements taken in early March of 2018 (black). The oscillation is the result of the light attenuation properties varying across the segment due to the support tabs. The sharp shoulders are caused by the acrylic boundary.

The position along the length of the segment is plotted in figure 4.7. Two important features are visible in both the simulated and measured data. Given the large observed statistics, a position dependant oscillation is observed. This is the characteristic Hobbes effect caused by the variable light attenuation properties introduced by the support rods. This was described previously in section 2.3.4. Two shoulders are visible near the edge of the segment at $\pm 600\,\text{mm}$. This feature is more prominent in the simulation; however, it is easily explained using the behavior of charged particles through matter. Materials with high electron density absorb more energy from charged particles than other materials. Thus, a muon is more likely to deposit energy near the PMT's acrylic housing or mineral oil than in the LiLS.

Cut Description	Data type	Events retained	Cumulative events retained
$E_{tot} \geq 15$	muons (MC)	156120	156120 (89.93%)
	not muons (MC)	5533	5533 (28.96%)
	measured data	1821441	1821441 (30.69%)
Size ≥ 3 events	muons (MC)	125523	123306 (71.02%)
	not muons (MC)	5418	3057 (16.00%)
	measured data	1851995	1538029 (25.91%)
PSD within 2.5σ	muons (MC)	123823	122174 (70.37%)
	not muons (MC)	4333	2632 (13.78%)
	measured data	1668765	1471320 (24.79%)
$E_{pulse} \geq 0.2MeV$	muons (MC)	122375	121034 (69.72%)
	not muons (MC)	3505	2193 (11.48%)
	measured data	1565921	1430949 (24.11%)
$\|z\| \leq 600$	muons (MC)	120042	120623 (69.47%)
	not muons (MC)	5375	2179 (11.41%)
	measured data	1728994	1391156 (23.44%)

Table 4.5: The amount of events retained by each cut is listed above.

The Monte Carlo simulation contains approximately 173611 identified muon events and 19103 events that are distinctively not muons. In contrast, a single calibration file can contain millions of clusters. This particular file contains 5935900 events. Table 4.5 outlines the behavior of each cut. The first column describes the behavior of that cut independent of the others, and the right column lists the cumulative events retained after each cut. This suggests that 23% of the total clusters measured by PROSPECT are retained through these cuts. Unfortunately, the simulations suggest that, for some representative sample of cosmic betas, 11.4% will pass these cuts. This may be reduced by introducing topological constraints on the cluster.

4.4.2 Neutron Selection Criteria

The procedure for identifying neutron captures on ^{6}Li follows the primary oscillation and spectrum analysis. The cluster must exist within 1.8σ of the nuclear recoil band with a deposited energy within 3σ of the lithium capture peak. Using a simulation of cosmic neutrons, the number of events that pass these cuts is listed in table 4.6. This simulation suggests that the cuts successfully identify 88.97% of nLi events.

Capture Target	Total Counts	Passed Cuts
All	29081	13760
Li	15438	13638
H	3661	69
C	8721	44
Other	1261	9

Table 4.6: The neutron capture events retained by the selection criteria is summarized.

4.4.3 Beta Selection Criteria

The derived selection criteria for correlated beta events will now be discussed. Beginning with a sample of 19103 non-muon events, cuts are applied in order to isolate beta samples. The results are expressed below in table 4.7.

Cut description	Data type	Events retained	Cumulative events retained
IBD-like prompt	not muons (MC)	18193	18193 (95.24%)
	measured data	5685011	5685011 (95.77%)
$E_{tot} \leq 60MeV$	not muons (MC)	19085	18173 (95.13%)
	measured data	4638841	4423671 (74.53%)
$E_{tot} \geq 5MeV$	not muons (MC)	8120	7688 (40.25%)
	measured data	1963330	549768 (9.26%)

Table 4.7: The amount of events retained by each Michel electron cut is listed above.

The cut labeled IBD-like prompt is used in the primary IBD analysis. It checks for a well defined event in the active volume with a PSD within 2.5σ of the gamma band. The 5 MeV cut removes events produced by inverse-beta decay.

4.4.4 Simulated Correlations

The simulation may also be used to identify expected relationships between events. The time between the primary and secondary event, as well as the radial distance between them, can be determined by inspecting the event tables. Using the initial time, vertex and direction of the primary, the correlations were determined.

These correlations are visualized in figure 4.8; furthermore, their colour labels are assigned by how the primary muon behaves in the active volume. Every back data point describes the correlations between all possible primaries and their secondaries. The blue points, however, describe the subset of muons that are visible within the active volume. If a muon passes the vetoing criteria, it is labeled in red. These muons have deposited more than 15 MeV into the active volume.

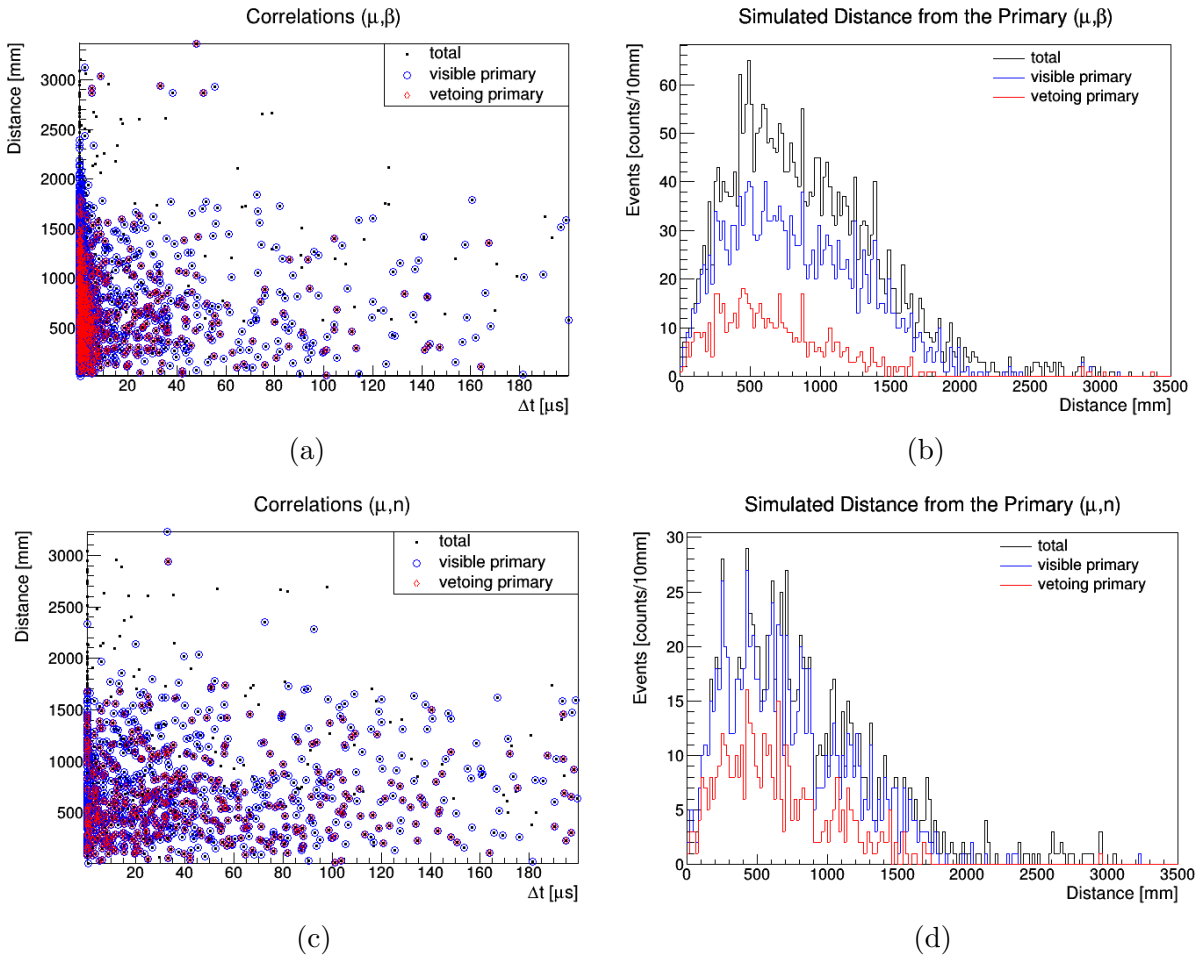

Figure 4.8: Correlations between simulated muons and their secondaries are displayed. Figure 4.8a and 4.8b describe the time of the decay products since the prompt event as well as its radial distance away from the muon. Furthermore, correlations between muons and neutrons are depicted in 4.8c and 4.8d.

The dense region in figure 4.8a reflects muon decay. It is expected that the decay products, on average, do not travel beyond 20 cm from the primary. A similar conclusion is observed between muons and neutrons in figure 4.8c and 4.8d; however, these conclusions can only be justified if the simulation is accurately reflecting the behavior of physical events. As discussed previously, the simulation does not accurately reflect the number of fast neutrons produced through muon spallation.

Chapter 5

Muon Track Reconstruction at PROSPECT

After a potential muon candidate is identified, it is subjected to the tracking procedure. Ideally, the routine produces a direction, origin, and speed for each candidate; however, accidentally processed and impure candidates yielded anomalous measurements.

These reconstruction errors, described in section 5.1 promoted the development for a more robust tracking routine. The final tracking routine is separated into two components. The *standard* tracking routine utilises a 4-dimensional principal component analysis (PCA) routine in order to arrive at an initial guess for the track parameters. If an analysis requires a more accurate estimate, the *precision* routine uses this initial guess as an input for a 6-dimensional Kalman filter. As an added benefit, the precision tracker isolates the muon track from anomalous measurements for additional analyses.

This section will describe the standard tracking routine in detail. The precision tracker, and future improvements, are suggested in appendix A. It will begin by describing the potential challenges that the PROSPECT's antineutrino detector introduces before describing the global PCA routine. This section concludes by contrasting the reconstructed trajectories between Monte Carlo simulations and measured data.

5.1 Muon Tracking Challenges

A segmented liquid scintillator introduces its own unique particle tracking challenges. Unlike other antineutrino detectors that incorporate water-based muon detection systems into

their background suppression strategies [12, 32, 36], the PROSPECT experiment cannot exploit the light profile produced from Cherenkov radiation. Since the PMTs are only capable of measuring a particle's location along the length of the segment, the x and y coordinate resolution is limited by the width of each segment. Furthermore, many segments are excluded from this analysis due to their variability in optical properties PMT electronic instabilities. This potentially introduces missing observations within the clusters. Consequentially, the muon tracking methods implemented for the PROSPECT collaboration are fundamentally different from the likelihood methods used in Daya Bay [12] and Double Chooz [36].

In PROSPECT, many identified muon candidates contain anomalous measurements. Most anomalous measurements arise from reconstruction errors; however, correlated events may be erroneously clustered within the muon candidate. For example, the inclusion of

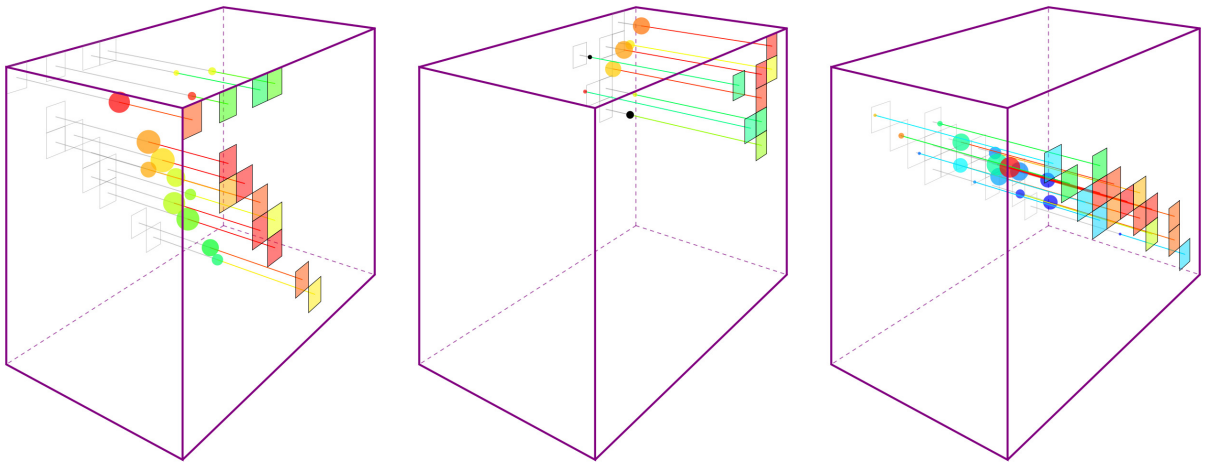

(a) Anomalies are introduced from correlated events.

(b) Anomalies are introduced from reconstruction errors.

(c) A false muon candidate.

Figure 5.1: Three examples of contaminated candidates are displayed. The time ordered sequence of pulsed data is visualized using coloured spheres. Red represents the earliest measurement, and dark blue represents the latest. The size of the sphere reflects the pulse shape parameter. Larger spheres represent electron recoil events, and smaller spheres represent nuclear recoil events. The deposited energy is illustrated by the projected cell colour. High-energy events tend towards red, while low-energy events tend towards blue. The black spheres represent improperly reconstructed neutron-like signals from neighbouring candidates.

proton recoil pulses from fast neutrons is likely to occur in high-energy muon clusters, and showering events may combinatorically result in false muon candidates. In addition, due to the clipping effect described in section 2.3.5, events that deposit a large amount of energy are poorly reconstructed in both pulse shape and time.

If the cluster's contamination is too high, the trajectory may be poorly defined. The resulting trajectory may appear non-relativistic or even traveling in an incorrect direction. The stopped muon in figure 5.1b, for example, contains a clipped event at the end of its trajectory. If an event is clipped, the reconstructed time and energy are expected to reduce from their proper values. Consequentially, the small red sphere is easily recognized as a clipped event. Additionally, high-energy events, such as the localized Michel electron in 5.1c, may accidentally contribute to the overall muon statistics. The electron cluster contains a random distribution of pulses; therefore, the reconstructed linear trajectory is non-physical. It is unclear if a minimally contaminated candidate, such as the cluster depicted in 5.1a, will have a poor fit quality; however, the secondaries introduced by the shielding may be removed through additional topological restrictions.

5.2 Tracking Geometry

Particle tracking quantifies the trajectory of charged particles through the LiLS by constructing a set of parameters that define its state of motion. Using these parameters, simulations of cosmic background events, as well as their underlying physical models, can be validated. In addition, these parameters are used to identify correlations between cosmic primary events and delayed secondaries.

If the desired particle is a relativistic muon, the tracking parameters should describe a line in $\mathbb{R}^3$. The lack of external magnetic fields implies that the trajectory will neither curve nor deflect, and the muon's time of flight through the detector is sufficiently small[1]. The desired parameterization is given in equation 5.1.

$$\mathbf{r}(t) = \mathbf{v}t + \mathbf{r}_0 \tag{5.1}$$

Using the vector components of the reconstructed entrance point $\mathbf{r}_0$ and direction $\mathbf{v}$, angle and distance correlations can be determined. The magnitude of $\mathbf{v}$ is somewhat insignificant unless more complected energy dependant correlations are studied. Otherwise, it is more appropriate to transform the 3-dimensional direction vector into its angular components.

[1]For relativistic muons, the travel duration through the active volume is at most 10 ns.

With the origin centered within the detector, the left-handed Cartesian system is constructed to reflect increasing segment indices. The x component increases from left to right, while y increases vertically. The z component increases along the length of the segment. This configuration is illustrated in figure 5.2. In spherical coordinates, the zenith and azimuth angles θ and ϕ point in the direction of travel. The azimuth angle has been defined to reflect the segmented design so that $\phi = \pm\pi/2$ is parallel to the segments. In addition, the angular coordinates (θ, ϕ) directed towards the reactor core is $(\frac{3}{4}\pi, \pm\pi)$.

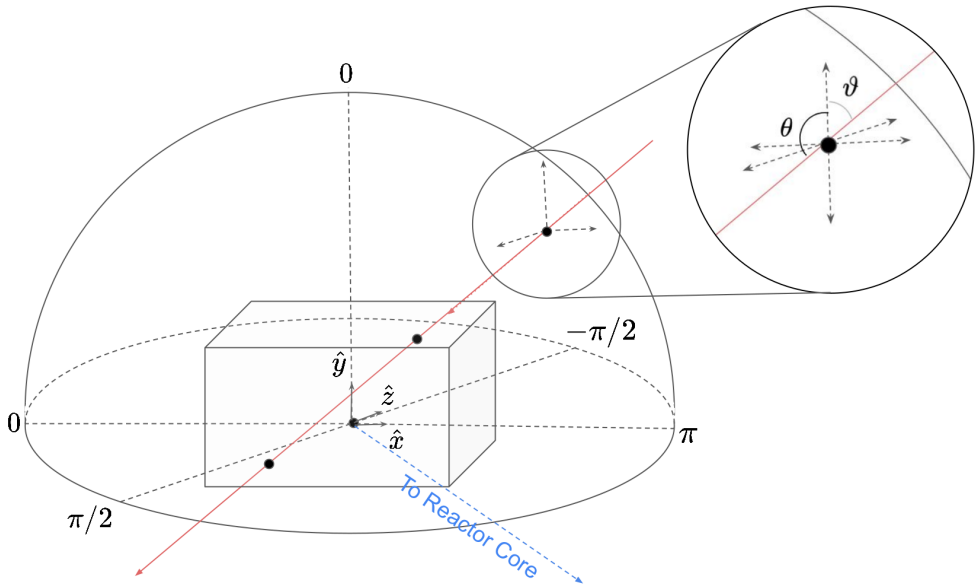

Figure 5.2: The Cartesian and spherical geometries used throughout the particle tracking routine is illustrated. A linear trajectory has been drawn through the active volume to illustrate the desired tracking parameters. The measured angles differ from the world coordinates ϑ used in simulations and theoretical calculations. World geometries are often defined relative to the direction of arrival such that $\vartheta + \theta = \pi$.

5.3 Muon Tracking Methods

In order to decide if a muon candidate is statistically viable, global trends are extracted from each cluster. Since the entire candidate is analysed simultaneously, the standard muon tracking routine borrows techniques from global pattern recognition algorithms. Due to the large quantity of statistics accumulated by the PROSPECT experiment, computational

efficiency is a major design limitation. Thus, within the overwhelming selection of data processing algorithms, principal component analysis (PCA) is an obvious choice. This analysis technique can extract features from each muon candidate necessary for particle tracking.

5.3.1 Principal Component Analysis

Principal component analysis (PCA) is a dimensional reduction strategy used in computational data analysis. Originally developed independently by Pearson [66] and Hotelling [67], it has found widespread use as a fundamental machine learning technique. Most commonly used in facial recognition software, PCA has been applied to far reaching and diverse fields from neuroscience to quantitative finance.

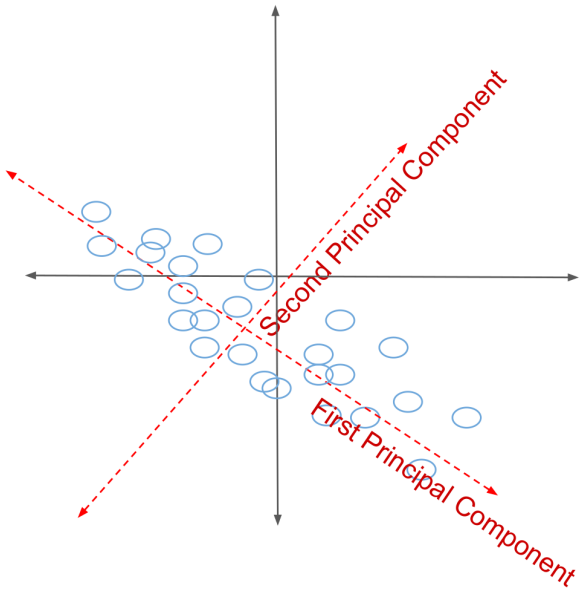

Figure 5.3: A 2-dimensional PCA construction is illustrated.

The linear PCA routine constructs a transformation from the vector space of measurements to a flat affine linear subspace. Within this new pattern space, the most relevant features are spanned by the first principal axis. Thus, the distribution is sufficiently described using only some basis vectors within reasonable error. If the data is centered at the mean, the PCA is a rotation around the origin until the distance to the subspace is minimized. This is illustrated in figure 5.3.

The new set of basis vectors is constructed from the empirical covariance matrix. If the cluster contains m measured pulses, each with d features, the cluster is represented using an $m \times d$ data matrix. The columns of the data matrix $\mathbf{X}$ represent a different measured quantity, and each row represents a new measurement. The rows must be redefined by their difference from the average $\mathbf{X}' = \mathbf{X} - \langle \mathbf{X} \rangle$ by applying an $m \times m$ translation operator $\mathbf{P}$. This operator is defined with main diagonal elements $1 - 1/m$ and off-diagonal elements $-1/m$ so that the matrix product remains within the vector space $\mathbf{X}' = \mathbf{PX} \in \mathbb{R}^{m \times d}$. The empirical covariance matrix $\mathbf{C}$ is constructed according to equation 5.2.

$$\mathbf{C} = \frac{1}{m} \mathbf{X}' \mathbf{X}'^{T} \tag{5.2}$$

the covariance matrix is symmetric and positive semi-definite; therefore, it is decomposed using the single value decomposition. The set of eigenvectors $\{\hat{\mathbf{e}}_i\}_{i=1}^{d}$ are the desired principal axes, and their respective eigenvalues $\{\lambda_i\}_{i=1}^{d}$ are indicative of the total variance. Together, these parameters describe how the data is distributed along each direction.

$$\sum_{i=1}^{d} \lambda_i = 1 \tag{5.3}$$

When applied to linear particle tracking, the PCA routine accepts a list of measurements $x_i \in \mathbb{R}^4$ corresponding to the 4-dimensional coordinates of each pulse (x, y, z, ct). The measurements are assumed to be a time ordered sequence of events stochastically distributed in a line. Consequentially, the first principal axis describes the trajectory.

$$\hat{\mathbf{e}}_1 = [v_x, v_y, v_z, v_t]^T = [\mathbf{v}_{x,y,z}, v_t]^T$$

Using the PCA method, both the direction of travel and the data centroid are obtained. The zenith angle θ, azimuth angle ϕ, and the speed can be recovered using the components of the sub-vector $\mathbf{v}_{x,y,z}$. These parameters are computed using equation 5.4 using a left-handed coordinate system.

$$\begin{aligned} |\mathbf{v}| &= \frac{|\mathbf{v}_{x,y,z}|}{v_t} c \\ \theta &= tan^{-1}\left(\frac{\sqrt{v_x^2 + v_z^2}}{v_y}\right) \\ \phi &= tan^{-1}\left(-v_z / v_x\right) \end{aligned} \tag{5.4}$$

5.3.2 Initial Position and Time Correction

The PCA routine returns the unit vector coinciding with the first principal axis as well as the centroid of the point cloud. For the purposes of tracking charged particles, it is convenient to represent the state dynamics with respect to the entrance point. The point $\mathbf{r}_0$ and time t_0 represents a location in $\mathbb{R}^4$ along the first principal axis and on the detector's surface. The entrance point is calculated using the intersection of lines and planes while the entrance time is calculated using basic kinematics.

The PROSPECT detector geometry is an enclosed rectangular volume; therefore, 6 bounding planes are constructed. Each plane represents an exterior wall of the active volume, and are expressed in terms of a vector normal to it's surface $\hat{\mathbf{n}}$ and a point in the plane $\mathbf{p}_0$. The set of all points in the plane $\mathbf{p}$ must satisfy the following relation:

$$(\mathbf{p} - \mathbf{p}_0) \cdot \hat{\mathbf{n}} = 0 \tag{5.5}$$

The entrance point is chosen from the set of collision points determined from the parameterized trajectory and the 6 bounding planes. If a line, with starting point $\mathbf{r}_0$ and direction $\mathbf{v}$, is expressed as $\mathbf{r} = \mathbf{r}_0 + \hat{\mathbf{v}}t$, it will intersect a plane at point $\mathbf{r}_c$ with time t_c.

$$t_c = \frac{(\mathbf{p}_0 - \mathbf{r_0}) \cdot \hat{\mathbf{n}}}{\mathbf{v} \cdot \hat{\mathbf{n}}}, \quad \text{and} \quad \mathbf{r}_c = \mathbf{r}_0 + \mathbf{v}t_c \tag{5.6}$$

Using the PROSPECT geometry, the set of bounding planes $\{P_i\}_{i=1}^{6}$ is constructed. The set of collision times and intersection points are calculated and the only geometrically meaningful candidate is retained. The entrance time must be smaller than the average value obtained from PCA, and the corresponding intersection point must be on the enclosed surface. In this case, if L and w represent the length and width of a segment, the enclosed active volume is bounded by the following constraints:

$$\begin{aligned} -7.5w \leq x &\leq 7.5w \\ -5.5w \leq y &\leq 5.5w \\ -L/2 \leq z &\leq L/2 \end{aligned}$$

These bounding planes can be adjusted to incorporate the width of the shielding. An additional width dw and dh is added to the side and top planes respectively. The bottom surface is ignored due to the inclusion of fictitious upward traveling muons. Regardless, the reconstructed entrance point resides on the surface of the shielding, and the reconstructed exit point resides on the surface of the active volume.

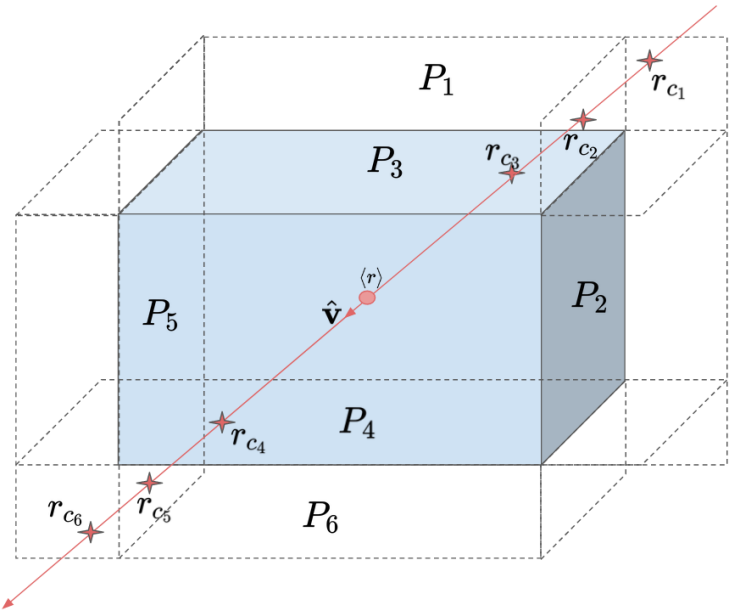

Figure 5.4: The enclosed rectangular volume containing the 6 enclosed surfaces is drawn. The set of intersection points $r_{c_i} \in \mathbb{R}^3$ is constructed such that each point lies on the line and $r_i \in P_i$. If the average point $\langle \mathbf{r} \rangle$ is measured at $\langle t \rangle = 0$, points r_{c_1}, r_{c_2}, and r_{c_3} have negative collision times. Only r_{c_3} and r_{c_4} are bounded on the surface of the active volume.

All 6 intersections and their respective boundary conditions are examined to produce a list of elements $\{t_{c,i}\}_{i=1}^{6}$. The entrance time $t_{c,\text{entrance}}$ has the smallest magnitude of the negative elements. If the candidate is assumed to exit the the active volume, the exit time $t_{c,\text{exit}}$ has the smallest magnitude of the positive elements. This argument is illustrated in figure 5.4. Using this method, both the entrance and exit points are reconstructed.

5.3.3 Data and Simulations

Monte Carlo simulations are used to test the validity of the tracking routine. By comparing the generated trajectory to the reconstruction, systematic uncertainties in the tracked angles are determined. These simulations underestimate the muon-neutron interactions expected at high energies. Furthermore, since the simulations poorly reflect the clipping effect described in section 2.3.5, comparisons between simulations and measured data highlight the problems introduced by anomalous measurements.

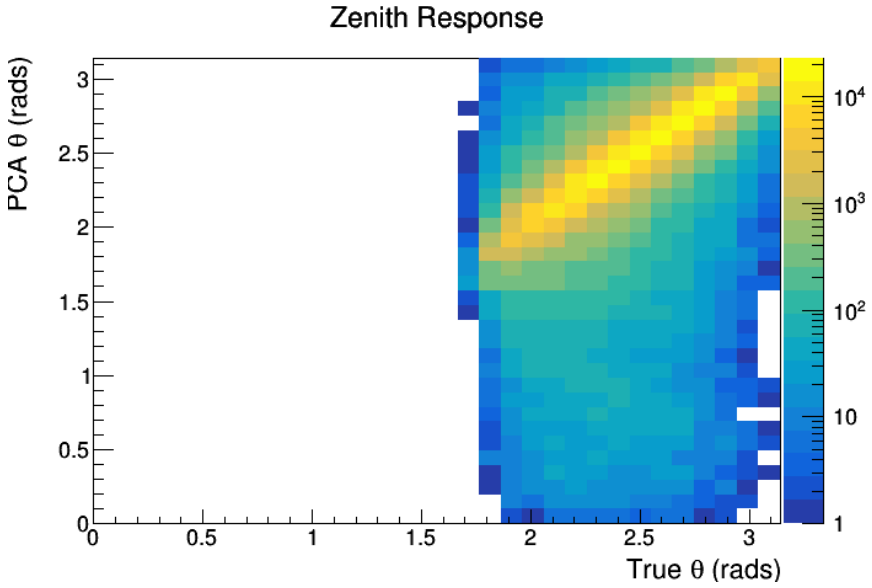

(a)

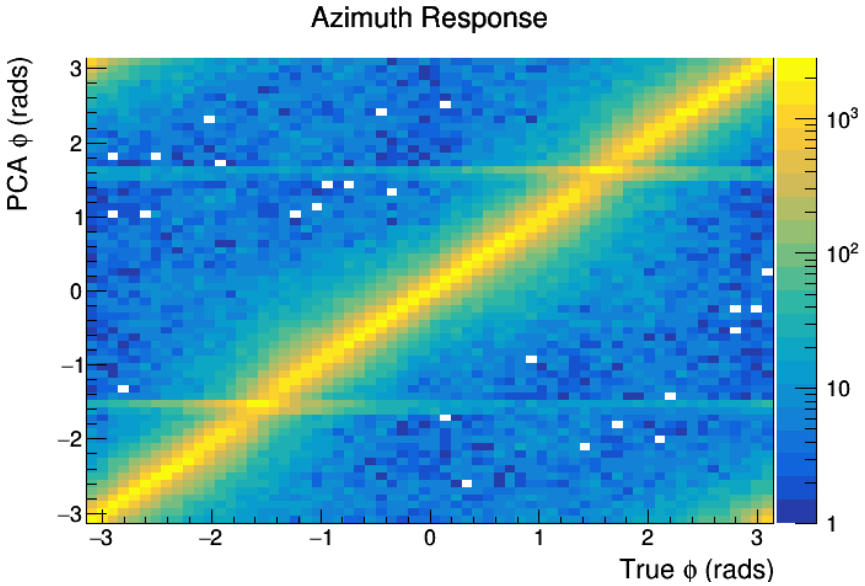

(b)

Figure 5.5: The zenith (a) and azimuth (b) response matrices are displayed. Events are recorded if the particle deposited energy inside the active volume, and the true angle generated by the simulation is matched to the reconstructed angle.

Figure 5.5 contrasts the generated trajectories against the PCA reconstructions within a simulation of cosmic muons. These detector response matrices contrast generated or *true* angle angle its reconstruction. If an angle is reconstructed properly, a diagonal bin is incremented. Consequentially, most of the generated muon candidates are reconstructed properly. Since the simulation only generates cosmic events downward, the small amount of upward-traveling muons observed in 5.5a is explained by the time perturbations of high-energy pulses. Distortions in the azimuth distributions are artifacts of segmentation. These are observed in figure in 5.5b around $\phi = \pm\pi/2$. Trajectories are likely to be reconstructed along a line parallel to $\hat{z}$ if the cluster is distributed randomly.

If a representative sample size is generated, the ratio between the true and reconstructed angle follows a Gaussian distribution where the standard deviation represents the average uncertainty in the reconstructed angle. Furthermore, each angle can be analyzed independently to determine the resolution for each direction. Figure 5.6 illustrates the standard deviations of this ratio. The left panels display how the uncertainty is determined using the entire angular acceptance range, and the right panels display the uncertainties for each angular bin. The average tracking errors, determined using the entire range of zenith and azimuth angles, are summarized in table 5.1.

As illustrated in figure 5.6b, trajectories at shallow angles have larger uncertainties than other events ($\sigma_\theta > 10\%$). Muons arriving at shallow angles are more likely to stop within the active volume; therefore, their clusters are likely to contain erroneously reconstructed pulses. Alternatively, due to segmentation, false candidates are likely to have near horizontal trajectories. The uncertainty in the reconstructed azimuth angle, illustrated in figure 5.6d, is significantly less obvious to extract due to the large tails introduced by angles near $\phi = 0$. Around this region, the Gaussian distribution widens and the simulated-to-reconstructed ratio becomes improperly defined. This does not suggest an asymmetry between muons traveling away and towards the reactor core. In fact, if the coordinate system is rotated 180°, the azimuth resolution does not change.

Measurement Type	Uncertainty
θ	2.11%
ϕ	3.92%
Total	4.45%

Table 5.1: The average uncertainties in the reconstructed angles are summarized. The total tracking uncertainty is treated as the sum of squares over both angles.

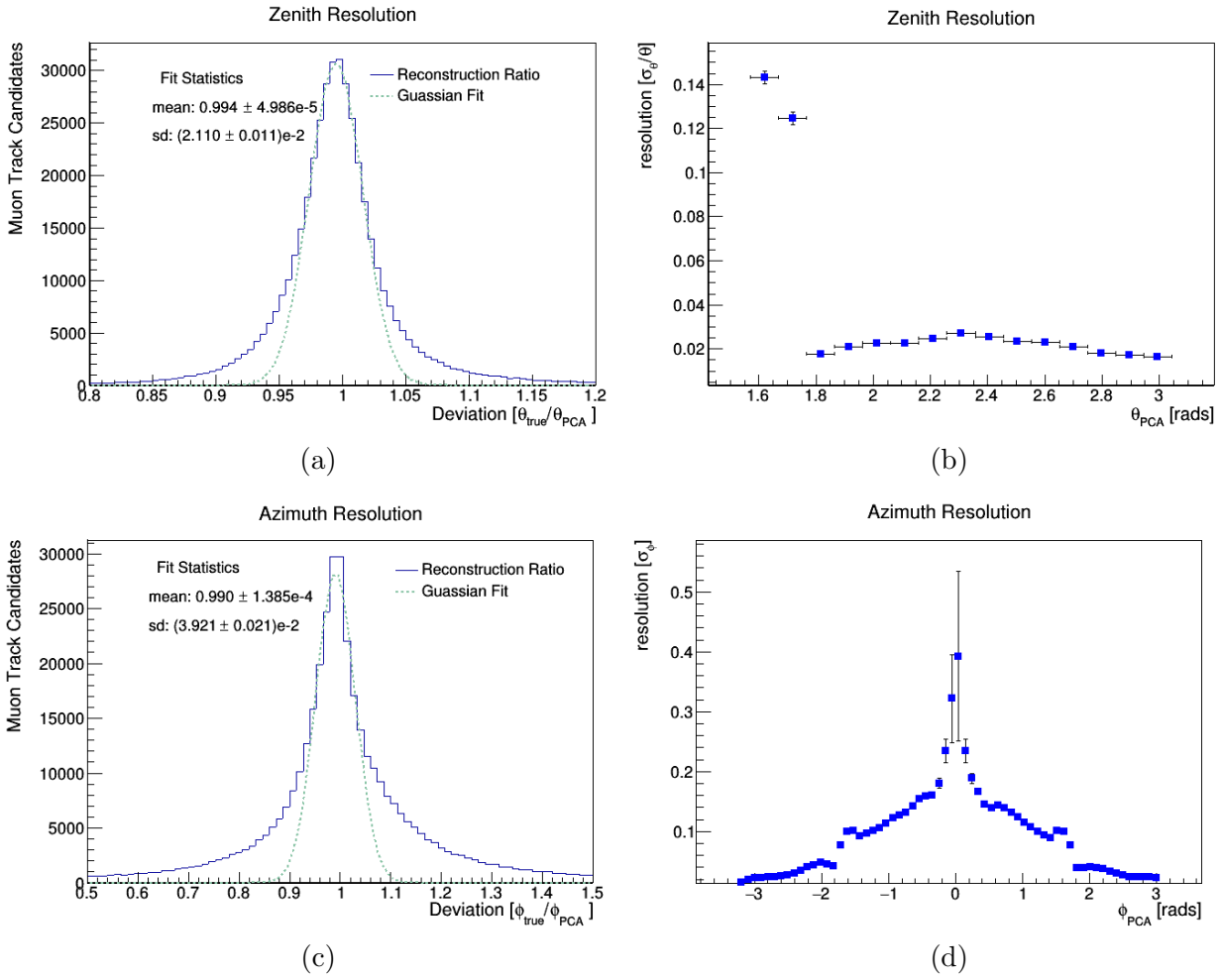

Figure 5.6: The angular resolution for each bin is determined for both zenith and azimuth reconstructions. Using a Gaussian distribution, the ratio of reconstructed to measured zenith (a) and azimuth angle (c) is used to determine the average reconstruction error. This procedure is performed over each zenith (b) and azimuth angle (d).

In addition, the simulations are contrasted against observations from PROSPECT. Figure 5.7 illustrates how the PCA tracking routine performs with calibrated data. The differences between the simulated and measured rate arises from the accidental inclusion of high-energy events not present in the simulations. In addition, the simulation does not include atmospheric conditions that influence the cosmic shower event through the atmosphere. The apparent shift in the leading edge of the measured zenith distribution towards

shallow and backwards traveling muons can be explained by the systematic inclusions of anomalous pulses within the candidates. The total number of upward traveling events is found by integrating between $0 \leq \theta \leq \pi/2$. As a result, approximately 30% of the observed trajectories appear to be traveling upwards.

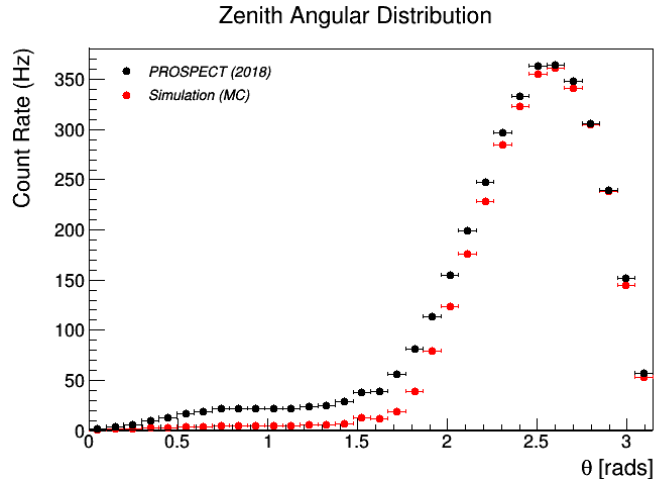

(a)

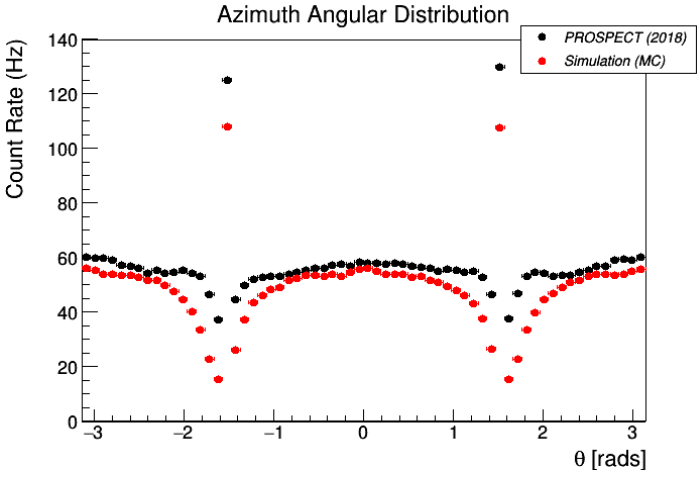

(b)

Figure 5.7: The zenith (a) and azimuth (b) distributions of measured and simulated cosmic events are contrasted. The measured events were observed using the PROSPECT detector, and both data sets represent approximately one hour of exposure time from early March of 2018.

Lastly, the reconstructed track length is investigated using measured data and simulations. The reconstructed path length is calculated as the difference between the entrance and exit points, and the muon is assumed to travel through the active volume without stopping. The entrance point reconstruction, described in section 5.3.2, includes the shielding. In addition, the distributions are contrasted against a reconstruction with 100% efficiency.

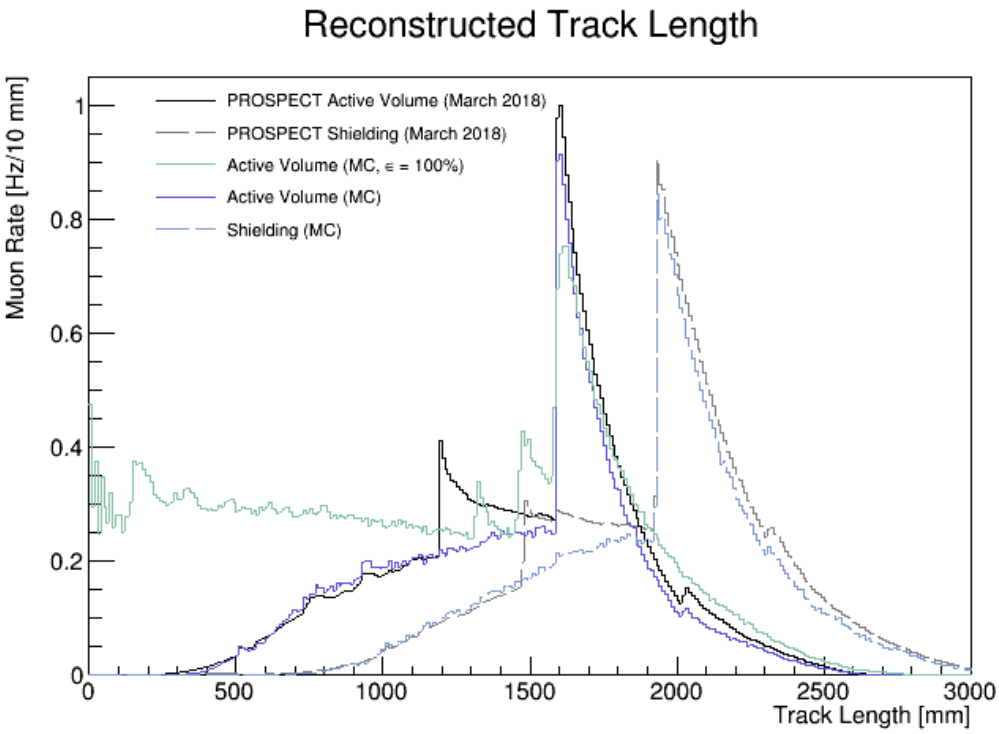

Figure 5.8: The reconstructed path length of through-going muons, determined for simulations (blue) and measured data (black), is contrasted with a simulations with 100% reconstruction efficiency (green). The reconstructed entrance point is determined with and without shielding.

As observed in figure 5.8, the shielding shifts the distribution towards larger path lengths. The thicker shielding at the top of the detector slightly stretches these distributions. In addition, geometrical feature corresponding to the detector dimensions are visible. The dominant peak at approximately 1600 mm (and 2000 mm if the shielding is included) is the result of diagonal trajectories that originate from the top of the detector. A small peak at 2000 mm (and 2300 mm) represent the candidates that travel across the

detector segments. A geometrical effect absent in simulations at 1200 mm (and 1500 mm) arises from the presence of false muon candidates with reconstructed trajectories along the length of the segments. The average path lengths are summarized in table 5.2.

Using these simulations, it is evident the the standard muon tracking routine is sufficient for resolving the directions of comic muons. The 4-dimensional PCA method is capable of reconstructing both the zenith and azimuth angles efficiently. After contrasting the measured data with simulations, it is apparent that additional work is needed to correct for the errors introduced by clipped pulses. Regardless, the average muon path length, as well as its systematic uncertainty, was successfully determined.

Tracking Candidate	Average Path Length (mm)	Uncertainty (mm)
Measured (active volume)	1489.15	66.27
Simulation (active volume)	1466.09	65.24
Measured (shielding)	1937.11	86.20
Simulation (shielding)	1931.02	85.93
Simulation ($\epsilon = 100\%$)	1130.11	50.29

Table 5.2: The average path length of the muon candidates are summarized. Reconstructed events from both Monte Carlo simulations and measured data are contrasted using truth data (efficiency $\epsilon = 100\%$). Each track length receives an approximate 2% and 4% error from the θ and ϕ reconstructions respectively. The total uncertainty in the track reconstruction is $\pm 4.45\%$

Chapter 6

Measured Cosmic Events in PROSPECT

This section describes the measured rates of cosmic events observed in PROSPECT. It begins by contrasting the observed muon rate against expected atmospheric dependencies to justify that the muon selection is independent of time varying experimental conditions. Afterwards, in order to determine the validity of the GEANT4 physics models, correlations between muons and their respective secondaries are contrasted between Monte Carlo simulations and observations performed by the PROSPECT detector. This section concludes by contrasting the measured cosmic neutron yield to theoretical predictions.

6.1 Atmospheric Muon Variations

By inspecting the theoretical meson propagation through the atmosphere, variations in the measured cosmic rates may be better understood. This applies to both underground [63, 68] and ground level [69] measurements. This method, however, can only yield average properties of the cascade and relies heavily on pre-determined assumptions determined from experimental conditions. Stochastic variations can, however, be introduced in Monte Carlo simulations on fast computers. Unfortunately, the Monte Carlo simulations used within the PROSPECT collaboration currently do not incorporate atmospheric conditions into their cosmic transport models. As a results, discrepancies between the measured and simulated muon flux is expected.

It is well documented that the interaction probability experienced by the atmospheric shower is influenced by the density profile along its trajectory [20, 37, 68]. Consequentially,

this section investigates atmospheric temperature variations and its effect on the measured muon rate. It begins by outlining how the correlations are studied for both underground detectors and for experiments located at Earth's surface before presenting the seasonal muon rate observed at PROSPECT.

6.1.1 Expected Temperature Dependence

Arising from atmospheric expansion, the mean free path length of cosmic rays are modulated by additional collisions experienced throughout their cascade. As a result, the meson is more likely to interact with neighbouring molecules at high atmospheric density. Equivalently, the interaction probability decreases with atmospheric temperature. As a result, a positive correlation between atmospheric temperature and the production of muons is expected [63, 68]. This correlation is also true for the decay products. As a result, there are two competing temperature interactions. As the temperature increases, the production of muons is expected to increase in the upper atmosphere; however, the probability that muon decays is also expected to increase in the lower atmosphere.

Temperature dependence is introduced to the meson transport through the critical energy of the meson [37, 63, 68, 69]. In this case, the critical energy $\epsilon_{n\in K,\pi,\mu}$ describes when energy losses between radiative processes and ionization are equally probable. Below this energy, the particle is likely to decay before reaching the ground.

The original atmospheric dependence was proposed by Barrett [63] and later summarized by Grashorn [68] for use in determining the atmospheric meson charge ratio. They introduce the atmospheric dependence through the atmospheric height profile $H(T)$. For an isothermal, exponentially decaying atmosphere, the atmospheric scale height as a function of temperature T is expressed as $H(T) = RT/Mg$. Here M represents the average molar mass of atmospheric particles, g is the acceleration due to gravity, and R is the ideal gas constant. The scale height, and consequentially the critical energy, can be related to the zenith angle ϑ and slant depth X along the cascade since the atmospheric density profile is $\rho(X, \vartheta) = X\cos\vartheta/H(T)$. The critical energy of the parent mesons, in terms if their mass m_n and lifetime τ_n is given in equation 6.1. This dependence suggests that energy losses from radiative processes are more prevalent at higher temperatures, and particles are likely to decay.

$$\begin{aligned} \epsilon_n(T) &= \frac{m_n c^2 H(T)}{c\tau_n} \\ \epsilon_n(X, \vartheta) &= \frac{m_n c^2 X\cos\vartheta}{c\tau_n \rho(X, \vartheta)} \end{aligned} \tag{6.1}$$

In addition, atmospheric temperature can modify the average nucleon interaction length of the particles [38]. Beginning at zero at the top of the atmosphere, the flux of pions (or kaons) reaches a maximum at about $X \approx 140(160)$ g/cm^2 before decreasing due to decay and absorption effects. The average decay height is, therefore, modified by atmospheric density. As a result, the observed muon rate is linearly correlated with atmospheric temperature and exhibits a sinusoidal variation throughout the year. In contrast to surface detectors, experiments deep underground only observe deeply penetrating cosmic events and are typically insensitive to low-energy muons. The muon variation observed underground is only influenced by meson decay; therefore, it is out of phase with surface detectors[1].

Atmospheric muon variations are measured by contrasting the seasonal muon intensity against the atmospheric temperature. A simple method is presented by Grashorn [68] with applications specific for muon variations observed underground [12, 36, 70]. This method can, however, be modified to investigate the muon flux observed at the surface [20, 69]. Grashorn argues that the deviations in muon rate away from the average I_μ^0 is proportional to the seasonal effective temperature deviations.

$$\frac{\Delta I_\mu}{I_\mu^0} = \int_0^\infty dX \alpha(X) \frac{\Delta T(X)}{T_{\text{eff}}} = \alpha_T \frac{\Delta T_{\text{eff}}}{T_{\text{eff}}} \tag{6.2}$$

The proportionality constant $\alpha(X)$ is the quantity to be measured. It contains information about which hadronic interaction contribute to the measured muon rate, and it has been used to study kaon and pion production in the upper atmosphere by both underground [12, 36, 71] and underwater detectors [70]. The effective temperature T_{eff} is defined as the temperature where no deviations are present in the muon flux.

$$\Delta I_\mu \big|_{T(X)=T_{\text{eff}}} = 0 \tag{6.3}$$

The temperature profile through the atmosphere is not uniform; therefore, the effective temperature must incorporate muon flux predictions. If the temperature profile is measured at N discrete elevations above the ground, either through satellite or a high altitude balloon, the effective temperature experienced by the cascade is the weighted average of these temperature measurements. The temperature T and weights W_n are determined at each observation level X_n.

$$T_{\text{eff}} \approx \frac{\sum_{n=0}^{N} \Delta X_n T(X_n) W_n(X_n)}{\sum_{n=0}^{N} \Delta X_n W_n(X_n)} \tag{6.4}$$

[1] Underground and surface experiments can only be compared in this manner if they are near the same geographical latitude and atmospheric conditions are expected to be equivalent.

The weights, often expressed in terms of the interaction attenuation lengths Λ, must accurately reflect the sensitivity regions of the experiment. The attenuation lengths of the parent hadrons and secondary nucleons are given in table 6.1. For surface observations, the weights may be derived using a complete muon cascade model that includes lower energy nuclear interactions. This computation was performed by Dmitrieva [69]. By using this integration method, the muon and meson components can be computed for various observation depths, angles, and threshold energies.

Particle Species	Atmospheric Attenuation Length (Λ)
Kaon K	180 g/cm^2
Pion π	160 g/cm^2
Nucleon n	120 g/cm^2

Table 6.1: The atmospheric attenuation lengths of different particles are summarized [38].

This method may, however, require complex integration techniques performed for each muon at each observation level. Furthermore, it is unclear if the telescopic resolution required for this computation is achievable with PROSPECT's segmented geometry. In addition, Dmitrieva argues that their weights are sensitive to the atmospheric muon flux model [69]. A model should reflect realistic atmospheric conditions and incorporate the decay of mesons as well as primary protons interacting with heavy atmospheric nuclei[2].

A complementary alternative is presented by de Mendonça [20]. In their report, the seasonal muon flux measurements of the global muon detector network (GMDN) is used to validate various atmospheric weight methods. The GMDN is composed of four muon telescopes located around the Earth. Their geographical coordinates are listed in table 6.2.

Name	Latitude	Longitude	Elevation
Nagoya, Japan (NGY)	35.15 °N	136.97 °E	0.077 km
Kingston, Australia (HBT)	43.0 °S	147.29 °E	0.065 km
Sao Martinho da Serra, Brazil (SMS)	29.44 °S	53.81 °W	0.488 km
Kuwait City, Kuwait (KWT)	9.37 °N	47.98 °E	0.019 km

Table 6.2: The coordinates of the global muon detector network are listed [20].

[2]Dmitrieva's muon flux model follows from a simplification of the Bugaev flux [37]. The amplitude of the parent mesons are assumed to decrease exponentially as $1/\Lambda$, and nucleon interactions are ignored.

In their investigations into atmospheric correction techniques, de Mendonça [20] found that a modification to the effective temperature $T_{\text{eff}-\text{M}}$ was in good agreement with observations. This method is used to validate the muon selection criteria in this work. The effective temperature and its modification are expressed in equation 6.5 and 6.6 respectively. Both methods, taken from [20], attempt to replicate the muon flux observed across the GMDN network. For experiments located deep underground, higher weights should be awarded near the top of the atmosphere because neither pions nor kaons are likely to survive to shallower altitudes [63]. This is not appropriate for surface detectors because contributions from muon decay is ignored. In fact, the negative correlation from muon decay is negligible below 1600 m.w.e. Instead, higher weights should be assigned near the average decay altitude. The effective temperature and its modification are summarized in equation 6.5 and 6.6 respectively.

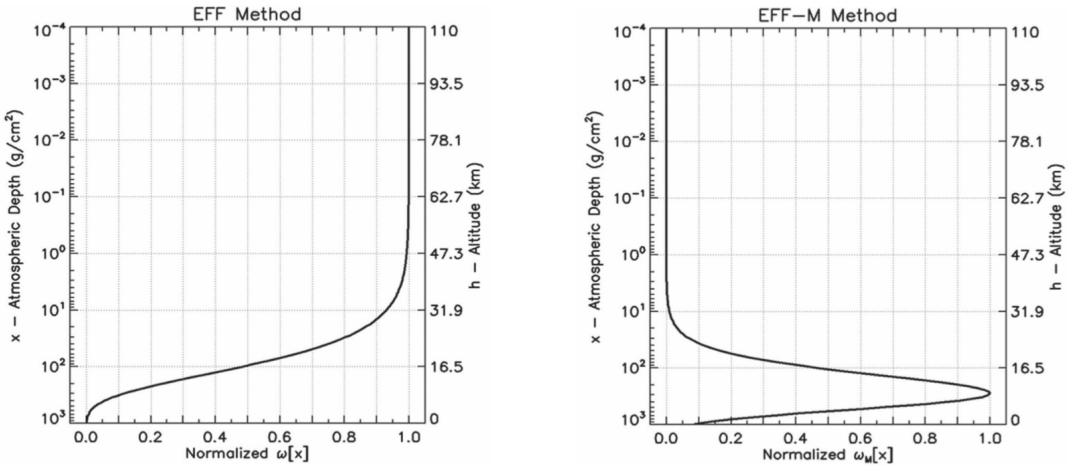

(a) (b)

Figure 6.1: Taken from [20], the effective temperature weights in 6.1a are contrasted against the modified weights in 6.1a. Each distribution is normalized by their maximum value.

1. **Effective Temperature:** Borrowing from underground detectors, the effective temperature weights are modified to include the attenuation lengths of the hadrons and nucleons. As before, the effective temperature is a weighted average over the measurements altitudes. In this case, the temperature and weights only depend on atmospheric depth x.

$$T_{\text{eff}} = \frac{\int_0^{x_{grd}} w[x]T[x]dx}{\int_0^{x_{grd}} w[x]dx} \qquad w[x] = \frac{1}{x}\left(e^{-x/\Lambda_\pi} - e^{-x/\Lambda_n}\right) \tag{6.5}$$

2. **Modified Effective Temperature:** Qualitatively, an adjustment to the effective temperature weights is introduced in order to replicate the expected behaviour in warmer months.

$$T_{\text{eff}-\text{M}} = \frac{\int_0^{x_{grd}} w_M[x]T[x]dx}{\int_0^{x_{grd}} w_M[x]dx} \qquad w_M[x] = x\left(e^{-x/\Lambda_\pi} - e^{-x/\Lambda_n}\right) \tag{6.6}$$

de Mendonça [20] argues that the modification to the effective temperature more accurately reflects the atmospheric profile of muons observed at the ground. Due to the $1/x$ dependence, the effective temperature assigns stronger weights to elevations above 30 km. This is illustrated in figure 6.1a. de Mendonça also illustrates that, since there is an anti-phase between the seasonal temperature variation at the top of the atmosphere and the ground, surface detectors should expect a decrease in the muon intensity during the summer. This is a result of the increase in the atmospheric expansion associated with the ground temperature.

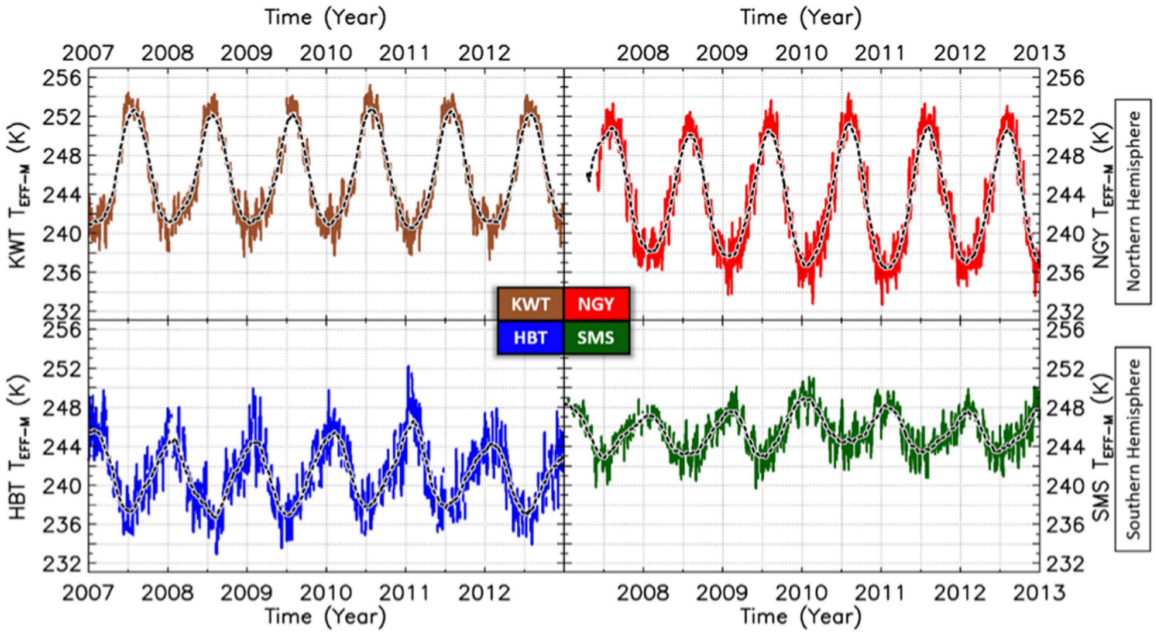

Figure 6.2: The seasonal variations of the modified effective temperature is contrasted over the four observation sites within of the GMDN [20].

The seasonal temperature variation observed at each detector is presented in figure 6.2. A clear sinusoidal variation in observed at all four detectors; moreover, the variations

observed in the northern hemisphere are out of phase from the observations performed in the southern hemisphere. This is most noticeable between the rates from Brazil (SMS) and Japan (NGY). These variations are contrasted against the measured muon rate in figure 6.3. Due to the similarities in lateral elevation from the equator, measurements performed at PROSPECT will be contrasted against the observations from Kuwait City (KWT).

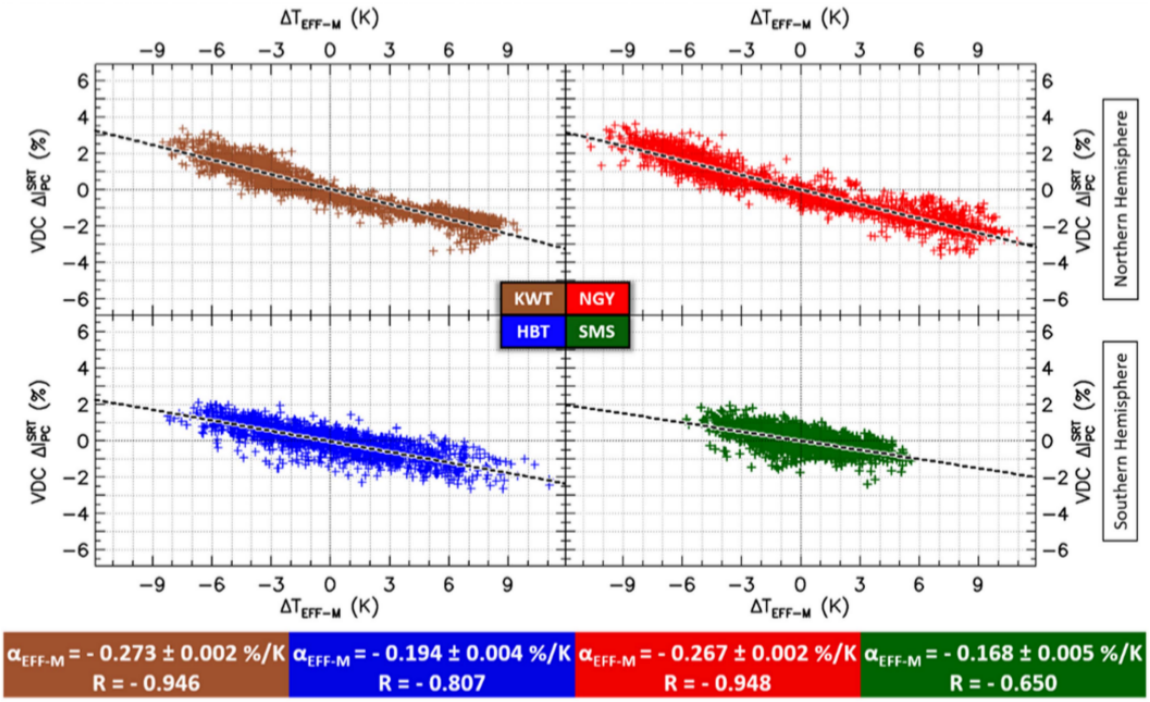

Figure 6.3: The modified effective temperature is contrasted against the seasonal muon rate at the four observation sites of the GMDN [20]. The correlation quality is illustrated by the Pearson's coefficient R.

6.2 Measured Atmospheric Muon Rate

As described in section 6.1.1, since the decay point of both the muon and its parent are not deterministic, the probability that a muon is detected at the ground is strongly correlated with atmospheric conditions. Thus, in order to determine if the muon selection criteria is independent of the drifting optical properties of the detector, the seasonal muon rate is contrasted against expected temperature variations.

This study contrasts two well defined muon samples observed in PROSPECT. The first muon sample is isolated using a simple energy threshold above 15 MeV. This data set, referred to as the vetoing muons, is used in the primary spectrum and oscillation analysis to separate cosmic backgrounds from the IBD candidates. The sample labeled tracked muons represents the candidates identified using the selection criteria throughout this analysis. The selection criteria are defined in section 4.4.1.

In collaboration with [22], the modified-effective atmospheric temperature is contrasted against the measured muon rate. The temperature data is provided by the Integrated Global Radiosonde Archive (IGRA) from the National Centers for Environmental Information [21]. Furthermore, their Nashville station is chosen due to its proximity to Oak Ridge. During the experiment, a high altitude balloon was launched from this national weather station every day at 6 am and 6 pm (0:00 and 12:00 UTC) unless extreme weather conditions arise. The balloon acquired the relevant pressure and temperature data needed to perform the atmospheric weighted averages at well defined elevations.

The balloon's flight pattern is, however, not uniform. Due to its variability in elevation, reaching its maximum elevation between 36 000 m and 37 000 m above the ground, measurements exceeding an atmospheric pressure of 10 000 mbar are removed. In addition, since the temperature data near the Nashville station may not accurately reflect the atmospheric conditions near Oak Ridge, the IGRA data was contrasted against measurements at ground level. Information about this temperature validation strategy, as well as the averaging method, is found in [22].

The averaged muon rates and mass-weighted effective temperature are determined over PROSPECT's entire lifetime. If no temperature variations are present, the measured muon rate is assumed to reflect the average. In addition, the results are contrasted against Monte Carlo simulations using the same set of cuts. The simulations do not replicate atmospheric interactions and are used to estimate the purity of the sample. Furthermore, since the total exposure time does not reflect a full 12 months, the average temperature and rate may not reflect the appropriate values. The results are presented in table 6.3.

Parameter	Units	Measured Average	Simulated Average
$T_{\text{eff}-\text{M}}$	K	246.10 ± 3.87	(-)
Vetoing Muon Rate	Hz	480.52 ± 7.55	470.437 ± 0.45 %
Tracked Muon Rate	Hz	389.35 ± 6.12	386.340 ± 0.09 %

Table 6.3: The average muon rate and mass weighted atmospheric temperature is listed.

Figure 6.4 displays the observed muon rate and atmospheric temperature variation across the detector's entire operation cycle. As expected, a sinusoidal variation is observed with a minimum muon rate occurring in warmer months. Due to the purity of the samples, the tracked muon set has a visibly steeper variation than the set of vetoing muons. The sample purity, defined as the fraction of false muon candidates within the sample, is estimated using table 4.5 in section 4.4.1. The vetoing and tracking sample removes approximately 70% and 90% of muon secondaries respectively; therefore, the final samples are estimated to contain 3.43% and 1.77% accidental events.

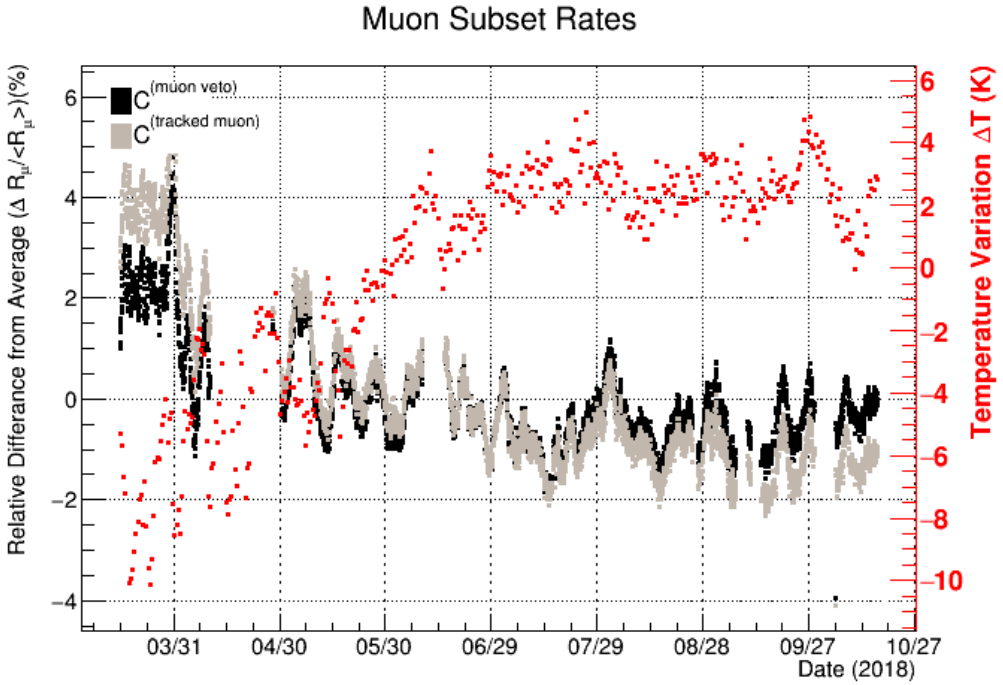

Figure 6.4: The seasonal variation in the observed muon rate is contrasted against the mass-weighted atmospheric temperature.

Temperature correlations are explored further in figure 6.5. Since the atmospheric muon rate is linearly correlated to the atmospheric temperature, the deviations are plotted against each other. The temperature constant α_T is determined from the linear relation.

$$\frac{\Delta R_\mu}{\langle R_\mu \rangle} = \alpha_T \Delta T_{\text{eff}-\text{M}} \tag{6.7}$$

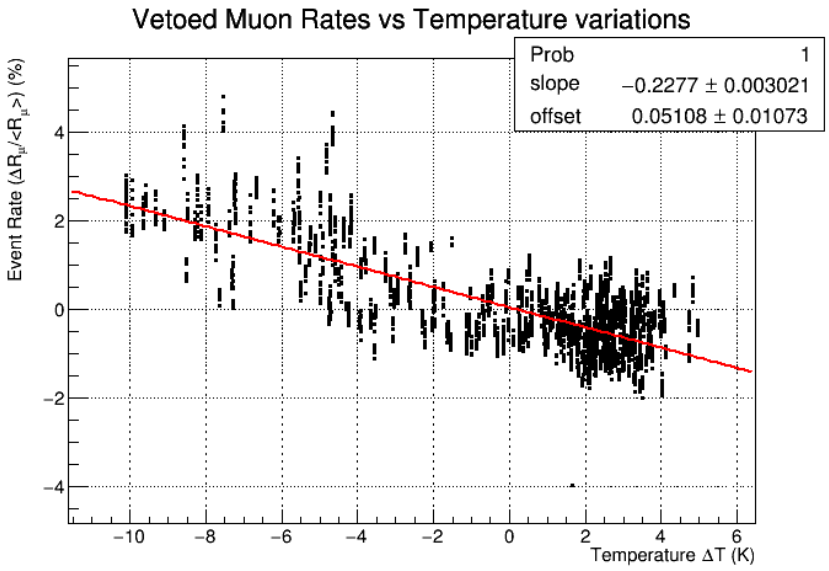

(a)

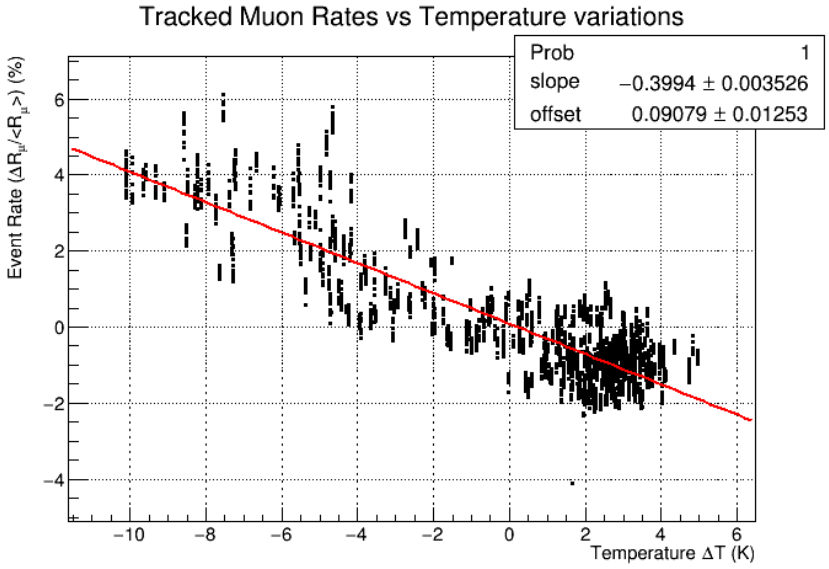

(b)

Figure 6.5: The atmospheric temperature constant is investigated using the set of vetoing muons (a) and the set of tracked muons (b).

The fit results are summarized in table 6.4. The disagreement between the two data sets taken from the PROSPECT experiment must be addressed. Since the uncertainties are taken from the fitting results, they do not incorporate the purity of the samples. The inclusion of particles that are anti-correlated with temperature, such as pions and kaons, will reduce the temperature coefficient. Alternatively, events that are positively correlated with temperature, such as muon secondaries, will increase the temperature coefficient. Consequentially, a refined sample will give the appropriate temperature coefficient.

Data Set	α_T (%/K)
Vetoing Muons	-0.228 ± 0.003
Tracked Muons	-0.399 ± 0.004
Kuwait City (GMDN) [20]	-0.273 ± 0.002

Table 6.4: The mass weighted temperature constants are listed.

This analysis is intended to address the variation in muon rate observed in PROSPECT. Since this variation relies heavily on atmospheric conditions above the detector, these observations are not expected to agree with other measurements perform at different climates. As a result, the temperature constant from the vetoing and the tracked muon samples do not agree with the results from [20]. A more physically motivated atmospheric averaging method, such as the one suggested in [69], may elucidate a deeper understanding of atmospheric muon interactions. Their method utilises the trajectory of each muon; therefore, additional refinement in both the cut selection and muon path reconstruction should be explored.

6.3 Methods for the Correlation Studies

Much like the primary spectrum and oscillation experiment, correlated events are identified using prompt and delayed signals. In this case, the prompt event is a cosmic muon, and the delayed event is either a high-energy Michel electron arising through muon decay, or a neutron that captures on ^{6}Li.

These events are identified by imposing constraints on their total deposited energies and PSD parameters. The optimised selection criteria ϵ_E, determined through Monte Carlo Methods, are described in section 4.4. Furthermore, the systematic uncertainty in the selection criteria arises from underlying processes not properly replicated by the simulations. As a result, the uncertainty is approximated by the relative difference in simulated

and measured rates. The cut selection efficiencies and their respective uncertainties are listed in table 6.5.

$$\frac{\sigma_{\epsilon_E}}{\epsilon_E} \approx \frac{R_{MC} - R_{data}}{R_{data}} \tag{6.8}$$

Particle Species	$\epsilon_E \times 10^{-2}$	$\sigma_{\epsilon_E} \times 10^{-2}$
μ	69.47	8.46
β	40.25	4.89
n	88.97	13.56

Table 6.5: The cut selection efficiencies for each particle species is recorded.

Additional constraints must be introduced between the prompt and delayed events. If the detector is sufficiently large, a distance criteria could be introduced. This, however, would couple the selection of the secondaries to the muon tracing efficiency. Instead, only a time constraint is imposed. This introduces its own efficiency correction ϵ_τ.

The time correction is easily determined using a distribution of elapsed time since the prompt event. Since the probability that a secondary is correlated with a primary event decreases with time, the distribution is expected to follow an exponential trend $R(t)$ with time constant $-\tau$ and initial value R_0. The distribution is written in equation 6.9.

$$R(t) = R_0 e^{-t/\tau} \tag{6.9}$$

The efficiency, defined as the ratio of observed events N_{Obs} within the desired time window to the total number of events N_{tot}, is determined by integrating the distribution. If events are identified between $t_i \leq t \leq t_f$, the observed and expected number of events are defined using equation 6.10.

$$N_{tot} = \int_0^\infty R(t)dt = R_0\tau, \qquad N_{Obs} = \int_{t_i}^{t_f} R(t)dt = R_0\tau\left(e^{-t_i/\tau} - e^{-t_f/\tau}\right) \tag{6.10}$$

The efficiency, and its variance, are easily computed using the ratio between the observed and total events using equation 6.11.

$$\epsilon_\tau = \frac{N_{Obs}}{N_{tot}} = e^{-t_i/\tau} - e^{-t_f/\tau}, \qquad \sigma^2_{\epsilon_\tau} \approx \left|\frac{\partial \epsilon_\tau}{\partial \tau}\right|^2 \sigma^2_\tau \tag{6.11}$$

The final goal is to contrast the corrected rate of secondaries against Monte Carlo simulations. As a result, the observed number of correlated events must be adjusted by the appropriate selection efficiencies. The observed rate is determined by tabulating the candidates that fall within the time window.

6.4 Correlated Betas

In this section, muon decay and the produced Michel electrons are carefully examined in order to validate the simulations. Betas are identified using the selection criteria defined in section 4.4.3; however, additional correlations with the prompt muon are introduced. A delayed beta event must be between 0.75 and 10 μs of the prompt muon. The final rate, and any resulting distributions, are scaled by the events that fall within an accidental time window between 0.75 and 10 000 μs before the prompt beta. Since a time constraint is introduced, the total rate of observed Michel electron must be scaled by both the cut efficiency ϵ_{E_β} and the decay time efficiency ϵ_{τ_μ}.

$$N_\beta = \frac{N_{\beta,Obs}}{\epsilon_{E_\beta}\epsilon_{\tau_\mu}} \tag{6.12}$$

Using basic geometrical observations, this section begins by investigating muons that stop inside the active volume. The muon lifetime and efficiency are determined, and the final rate is predicted. This section concludes by contrasting the total deposited energy and rate of Michel electrons between simulations and observed in PROSPECT.

6.4.1 Stopped Muons

The degradation of the detector's optical performance lead to the exclusion of a number of LiLS segments from the final analysis. As a result, many pulses within muon clusters are not observed, and the identification of stopped muons becomes somewhat abstract. Regardless, a stopped muon is identified if the final time ordered pulse within the cluster is far from the edges of the detector. If it is within the 2 outermost segment rows or columns, or within 10 cm of a PMT housing, it is considered a through-going muon.

Muon Candidate	Observation Type	Rate (Hz)	Uncertainty (stat)
Total muon rate	Measured	433.49	0.04 %
	Simulated	386.340	0.09 %
Stopped muon rate	Measured	55.45	0.02 %
	Simulated	45.16	0.24 %
Decayed muon rate	Measured	4.94	0.04 %
	Simulated	4.40	0.79 %

Table 6.6: The observed muon rate $N_{\mu,Obs}$ is contrasted between simulation and data.

Table 6.6 summarizes the muon count rate between simulations and data taken early in the detector's lifetime before the optical degradation became problematic. The simulated exposure time is approximately one hour, and the experiment lifetime spans 14.9 days. Furthermore, the observed rate of decayed muons is summarized. These are identified if a high-energy beta event occurs within 10 μs after a stopped muon. If these cuts successfully identified both stopped and decayed muons with 100% efficiency, the remainder of the stopped muon sample would be populated by muons capture events.

To determine the proper muon count rate, the observed muon rate is scaled by the cut efficiency. Summarized in table 6.5, the simulated and measured count rates are scaled by $\epsilon_{E_\mu} = 0.6947 \pm 0.084$. The total expected muon rate is given in table 6.7.

Observation Type	Expected Rate (Hz)
Measured	621.52 ± 0.25 (stat) ± 9.19 (syst)
Simulated	553.92 ± 0.50 (stat) ± 8.19 (syst)

Table 6.7: The expected muon rate N_μ is summarized.

The expected muon count rates, determined using simulations and measured data, do not agree within uncertainty. In fact, the most extreme estimates differ by approximately 8%. This is easily explained by understanding what effects are excluded from the simulations or accidentally included in the data. The CRY generator does not accurately capture the effects of high-energy muons; furthermore, atmospheric interactions are omitted. As discussed in section 6.2, the measured muon rate is expected to deviate away from the average by at most 6% throughout the year.

6.4.2 Michel Electron Time Correlations

The time difference between the prompt muon and the delayed beta is plotted in figure 6.6. To determine the average lifetime of the muon, theses distributions are fit to a decaying exponential function displayed in equation 6.13. The fit parameters are the offset C, amplitude N_0 and time constant τ. At this time scale, the offset is expected to be constant.

$$f(t) = C + N_0 \exp\left(-\frac{t}{\tau}\right) \tag{6.13}$$

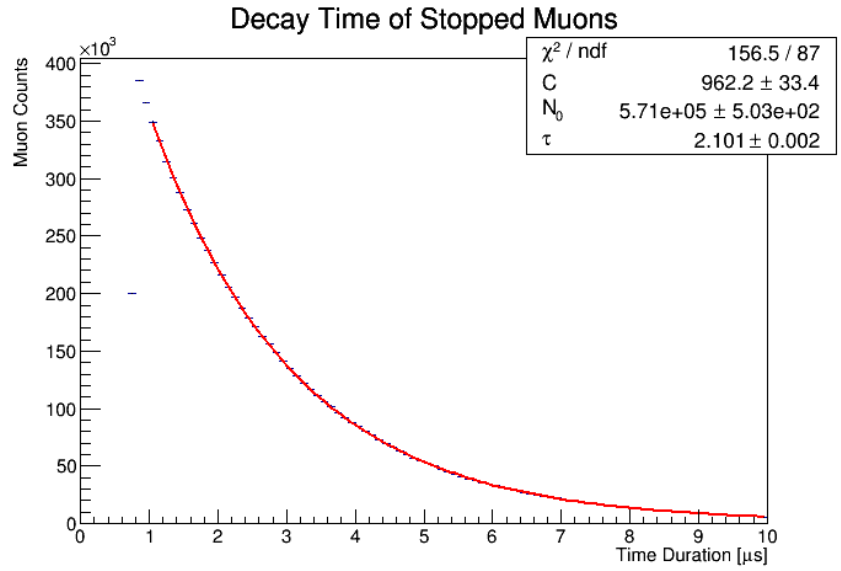

(a)

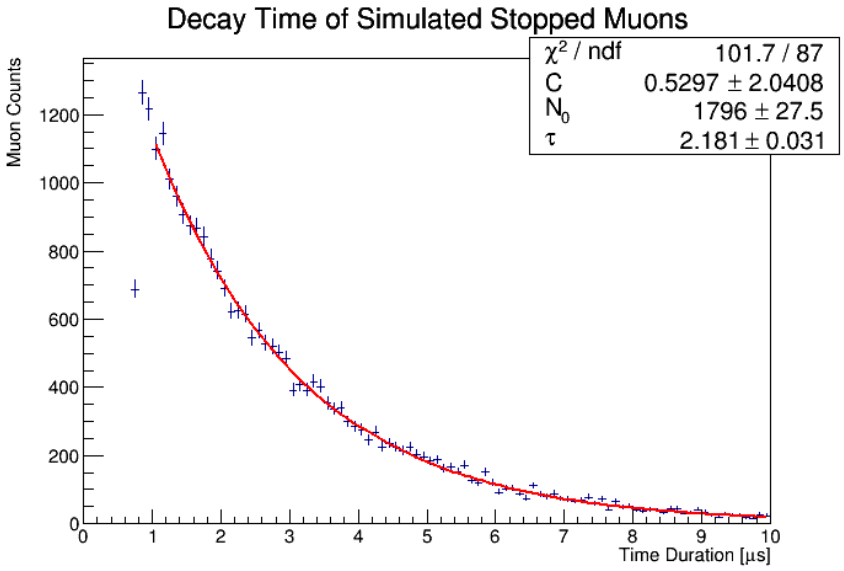

(b)

Figure 6.6: The time between the identified prompt muon and delayed beta events are plotted. Measurements observed using the PROSPECT experiment (a) are contrasted against Monte Carlo simulations (b).

The decay efficiencies are determined by integrating the distributions over the acceptance window, and are summarized in table 6.8 along with the muon lifetimes. Since the distribution produced by the PROSPECT measurements is expected to contain distortions from captured muons, the measured decay time ($2.101 \pm 0.002\,\mu$s) does not agree with the accepted μ^+ lifetime from TRIUMF experiment ($2.197033 \pm 0.000038\,\mu$s). Alternatively, the decay constant determined through simulations does agree within error. With a value of $2.181 \pm 0.035\,\mu$s, the disagreement between simulations and measured data suggests that the molecular interactions within the PG4 simulation are too simple to accurately reflect the production of muonic atoms and their respective decay and capture processes.

Parameter	Symbol	Value	
		Measured	Simulated
Muon Lifetime (μs)	τ_μ	2.101 ± 0.002	2.181 ± 0.045
Efficiency $\times 10^{-2}$	ϵ_{τ_μ}	69.12 ± 0.02	69.88 ± 0.41

Table 6.8: The calculated muon lifetime and efficiency is summarized.

6.4.3 Michel Electron Distance Correlations

The radial distance between the prompt muon and delayed candidate is studied using the tracking parameters. Since the tracking information gives the entrance point and direction of the prompt muon, the distance between these events is interpreted using the geometry of lines and points in $\mathbb{R}^3$.

The distribution, calculated using both measured and simulated data, is presented in figure 6.7. Due to systematic contamination in the measured data, a discrepancy is observed between the standard tracking procedure (black) and the simulated data (red). Fortunately, at the expense of computational efficiency, the newest iteration of the muon tracking procedure attempts to isolate a pure sample of muon pulses in an otherwise contaminated cluster. This results is a tighter, more accurate distance distribution around the muon track (dotted). Furthermore, geometrical features of the detector are observed at 145 mm. This segmentation artifact reflects the width of the LiLS housing. Additional information about the precise tracking routine is given in appendix A.

The ESTAR database from the National Institute of Standards and Technology [72] contains the stopping power and rage tables for a verity of elements and compounds. By approximating the LiLS as a block of polyethylene, the expected radial distance is determined. They report that, for electrons with kinetic energy near 60 MeV, the expected

range into the material is $23.10\,\mathrm{g/cm^2}$. The electron travel distance is calculated using the molecular density of the segments. Thus, high-energy electrons are expected to travel a maximum of $23.61 \pm 0.02\,\mathrm{cm}$ from the prompt muon.

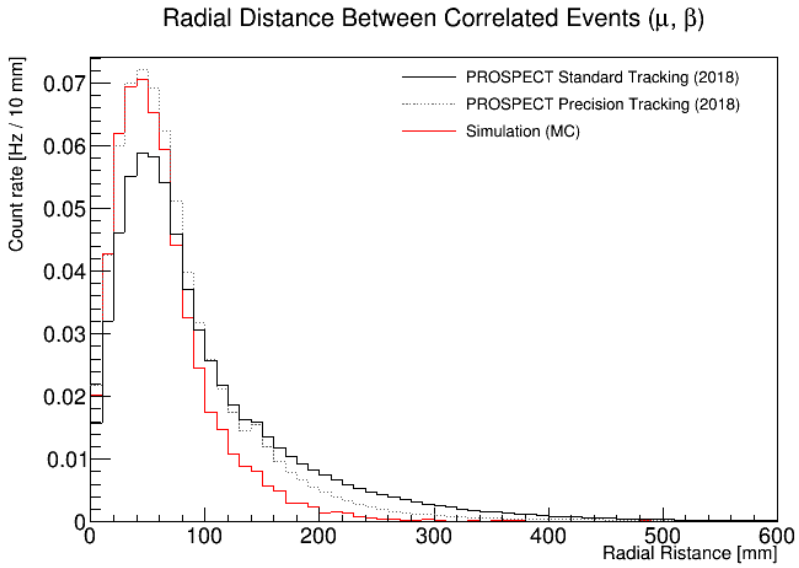

Figure 6.7: The radial distance between the prompt muon and electron is plotted.

6.4.4 Michel Electron Rate

Each beta event produces scintillating light into the active volume. This deposited energy is, however, quenched through the optical properties of the LiLS. Furthermore, the simulated quenching may differ from the measured events at large energies. Regardless, the deposited energy observed by the PMTs, expressed in electron equivalence, is tabulated for each correlated beta event.

The accumulated Michel electron spectrum, using both Monte Carlo simulations and measured data, is presented in figure 6.8. The differences between the simulated and measured distributions arise from discrepancies in the detector response and the relatively small sample size produced by the simulations. These distributions are integrated to determine the total observed rate $N_{\beta,Obs}$. Using equation 6.12, the expected rate N_β is scaled by both the cut selection and time correlation efficiencies. The results are summarized in table 6.9.

Since the expected Michel electron rates agree within uncertainty, the Monte Carlo simulations accurately reflect the behavior of muon decay in flight. The differences in mea-

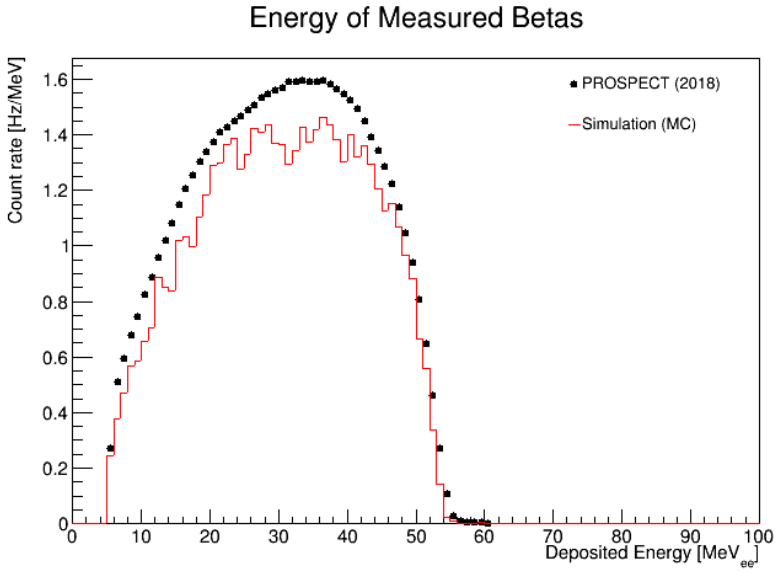

Figure 6.8: The measured and simulated Michel energy spectrum are contrasted.

sured and simulated decay times, however, suggest that these simulations may be further refined in order to accurately reflect muon captures within PROSPECT. The majority of the systematic uncertainty is introduced from the cut efficiency which may be improved by investigating clipped pulses and its effect on energy and pulse shape.

Observation type	Observed Rate $N_{\beta,Obs}$ (Hz)	Expected Rate N_{β} (Hz)
Measured	6.57 ± 0.05 % (stat)	23.62 ± 0.01 (stat) ± 2.87 (syst)
Simulated	5.73 ± 0.68 % (stat)	20.37 ± 0.14 (stat) ± 2.46 (syst)

Table 6.9: The observed and expected Michel electron rates are presented.

6.5 Correlated Neutrons

In this section, the correlations between prompt muons and delayed neutrons is explored. Due to the poor simulation statistics, a discussion comparing the simulations to data is omitted. Instead, this work is contrasted against the expected capture time and efficiency predicted by the PROSPECT collaboration [7].

Using the cuts defined in section 4.4.2, neutron events that capture on ^{6}Li are identified with an efficiency of $\epsilon_{E_n} = 0.8897 \pm 0.1358$ and a capture fraction of $\epsilon_{Li} = 0.744 \pm 0.007$. These efficiencies are used to predict the expected cosmic neutron rate.

$$N_n = \frac{N_{n,Obs}}{\epsilon_{E_n}\epsilon_{\tau_n}\epsilon_{Li}} \tag{6.14}$$

The neutron capture efficiency ϵ_{τ_n} is determined using the method outlined in section 6.4.2. For a neutron to be considered correlated with a prompt muon, it must occur between 2 and 300 μs after the muon. Convexly, the sample used for accidental subtractions is between 2 and 30 000 μs before the prompt event.

6.5.1 Neutron Capture Time

The time between the delayed neutron capture and prompt muon is plotted in figure 6.9. In addition, the multiplicity, defined as the number of identified neutrons for each muon, is also tabulated. The low multiplicity suggests that, since the average muon energy observed at the surface is assumed to be 4 GeV, the majority of correlated neutrons are not from local showering events.

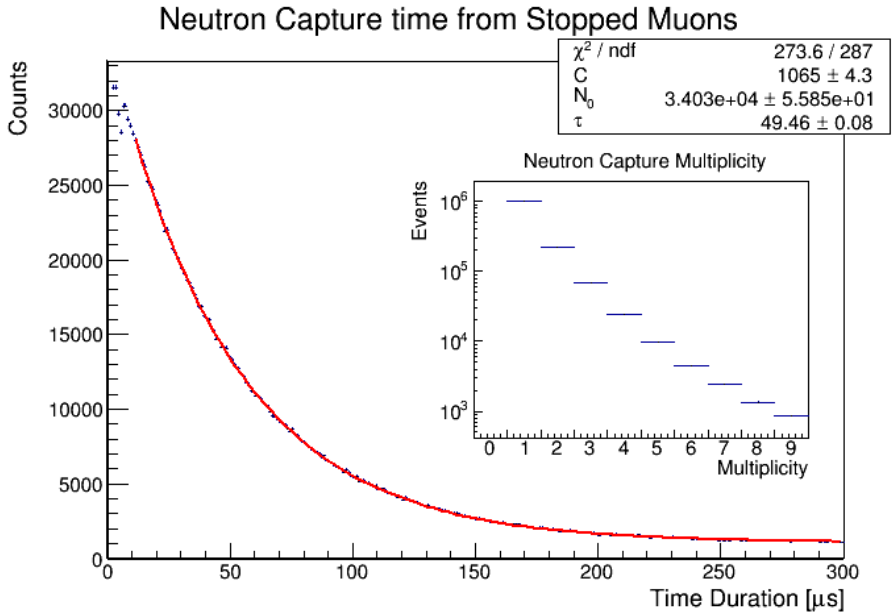

Figure 6.9: The time between a prompt muon and a delayed nLi capture event is plotted.

Table 6.10 contrasts the neutron capture time and efficiency determined using these selection criteria against previous studies. The capture time is determined by fitting the distribution to an exponential function. The disagreements between the results arise from the variations in the detectors optical properties. Furthermore, the cosmic neutron selection time window differs from the widow used in the IBD analysis. In the spectrum and oscillation studies, the correlated neutron is expected to occur within 120 μs of the prompt beta. The different limits of integration results in different capture time and efficiencies.

Parameter	Symbol	Value	
		This Work	Expected [7]
Neutron Capture time	τ_n	$49.46 \pm 0.08 \mu$s	$49.83 \pm 0.05 \mu$s
Efficiency $\times 10^{-2}$	ϵ_{τ_n}	95.80 ± 0.01	89.14 ± 0.03

Table 6.10: The neutron capture time on ^{6}Li and efficiency is contrasted between previous studies perform within the PROSPECT collaboration and this work.

Using the neutron selection criteria, the observed neutron rate is tabulated by counting the number of clusters that fall within the time window. The expected neutron rate follows from equation 6.14. As a result, if 1.073 ± 0.093 % neutron capture events are observed every second, the expected rate is 1.69 ± 0.002 (stat) ± 0.26 (syst) Hz. The cosmic neutron yield can now be computed.

6.5.2 Neutron Yield

The cosmic neutron yield represents the average number of neutrons produced at some observation depth. In this work, the yield is calculated using observations performed at the surface. Using the expected neutron and muon rate, the molecular density of the LiLS segments, and the average path length of the muon through the detector, the cosmic neuron yield is calculated. The parameters used in this calculation are listed in table 6.11.

Parameter	Units	Symbol	Value
Neutron Rate	Hz	N_n	1.69 ± 0.002 (stat) ± 0.26 (syst)
Muon Rate	Hz	N_μ	621.52 ± 0.25 (stat) ± 9.19 (syst)
Average Path Length	cm	L	193.71 ± 8.62 (syst)
Molecular Density	g/mL	ρ	0.9781 ± 0.0008 (syst)

Table 6.11: The parameters needed to determine the cosmic neutron yield is summarized.

The calculated and expected cosmic neutron yield are contrasted in table 6.12, and the neutron yield is calculated using equation 6.15. The expected yield, discussed previously in section 3.4.5, is calculated use a parameterized model extracted from measurements performed at different depths underground [13]. The expected and measured neutron yields agree within error. This demonstrates that, in spite of the large quantity of backgrounds observed at the surface and the systematic issues introduced by the clipped waveform signals, the PROSPECT detector is successfully capable of isolating the required prompt and delayed signals.

$$Y_n = \frac{1}{\rho \overline{L}} \frac{N_n}{N_\mu} \tag{6.15}$$

	Neutron Yield ($\times 10^{-6}$ μ^{-1} $\mathrm{g}^{-1}\mathrm{cm}^2$)
Expected	11.63 ± 2.00
Calculated	14.41 ± 2.30

Table 6.12: The calculated and expected cosmic neutron yield are summarized.

The error in the calculated yield can be reduced through careful optimizations of the muon identification and tracking routine. Arguably, the most critical and sensitive computation is the average path length. Since the tracking procedure relies an a 4-dimensional PCA deconstruction, any anomalous pulses may distort the reconstruction. Furthermore, the muon sample is contaminated by other high-energy events such as locally induced hadron showers and Michel electrons. These events may be removed by exploiting the geometrical features of the muon signal. Lastly, the time window between the prompt muon and delayed secondary can be optimized in order to remove accidental events.

Regardless, the cosmic neutron yield measured in this work is in agreement with the underground experiments introduced in section 3.4.5. This is illustrated in figure 6.10 where the PROSPECT measurement resides at an assumed average muon energy of 4 GeV. The neighbouring measurement is taken from Hertenberger [29] and the Palo Verde neutrino detector [30]. These experiments reach a depth of 20 and 32 m.w.e respectively. The other measurements are taken from Aberdeen Tunnel [31], KamLAND [32], and Daya Bay [13]. Together, these measurements are parameterized by equation 6.16.

$$Y_n\left(\overline{E}_\mu\right) = a\overline{E}_\mu{}^b \tag{6.16}$$

Without the new PROSPECT measurement, the parameters are $a = (4.0 \pm 0.6) \times 10^{-6}$ and $b = 0.77 \pm 0.03$. The parameterization does not change significantly by including the

new PROSPECT measurement. The new fit scale factor a becomes $(3.92 \pm 0.62) \times 10^{-6}$ while b remains unchanged.

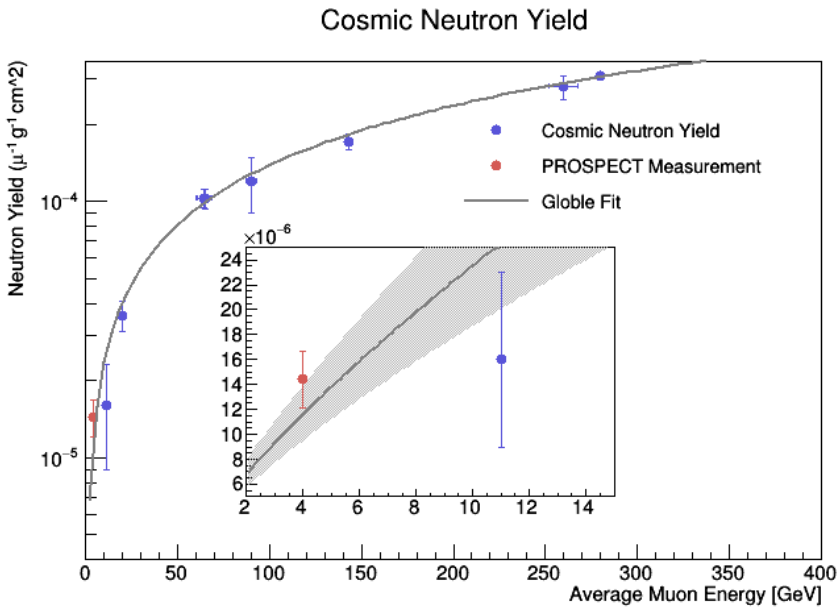

Figure 6.10: The neutron yield determined in this work is contrasted against the results from previous studies and the global fit from the Daya Bay collaboration [13].

This cosmic neutron yield measurement demonstrates PROSPECT's efficient particle identification and tracking techniques. By exploiting its PSD and energy identification strategy, muon-induced neutrons were selected with high efficiency. Furthermore, the muon tracking routine, as well as the high flux of cosmic muons, allowed for an appropriate estimate of the average muon path length through the detector. As a result, the average number of neutrons produced at the Earth's surface through muon interactions was accurately determined.

Chapter 7

Conclusions

Current reactor neutrino experiments have prompted deeper investigations into fundamental physics beyond the Standard Model. Using its segmented design, the PROSPECT antineutrino experiment has performed an unbiased measurement of the neutrino spectrum produced through the fission of ^{235}U. Its segmented design allows for a unique investigation into neutrino oscillations at short baselines. The development of the next generation of experiments, and possible detector upgrades, is currently underway to ensure that PROSPECT continues to remain at the forefront of reactor neutrino physics.

Unlike similar experiments, PROSPECT is located on Earth's surface with minimal overburden. As a result, the detector is constantly flooded with cosmic background events. Despite this, the collaboration has successfully developed a remarkable suppression strategy by introducing a series of vetoes and reactor-off subtractions. Its layered shielding prevents reactor backgrounds, such as gamma-rays and thermalized neutrinos, from contaminating the active volume. Additionally, its pulse shaped discrimination strategy, developed using the optical properties of ^{6}Li-load liquid scintillators, can separate nuclear and electron recoil events. Additionally, PROSPECT is exposed to low-energy cosmic events that are mostly unobserved by subterranean experiments. Moreover, most backgrounds observed at PROSPECT are introduced through cosmic neutrons. This prompted a deeper investigation into these interactions.

Originally envisioned to aid with optical calibration, a dedicated muon tracking routine has been implemented. Limited by the spacial resolution of each scintillator, the program was designed with the knowledge that individual high-energy events are poorly reconstructed at PROSPECT. As a result, the muon sample is contaminated with improperly identified candidates some containing erroneously reconstructed pulses with incorrect

energies and times. Even with these limitations, the entrance point and direction through the detector were accurately reconstructed.

This work further demonstrates the capabilities of the novel scintillators by investigating the correlations between cosmic events. A measurement of the cosmic neutron yield produced by muons at Earth's surface was performed by exploiting PROSPECT's efficient neutron detection strategy. Furthermore, it agreed with similar measurements from underground detectors.

The accuracy of these measurements can, however, be further improved by optimizing the muon detection and tracking strategy. Since these events are contaminated by accidental candidates as well as reconstruction errors from clipped waveforms, additional work is needed to isolate pure muon candidates. These limitations are largely responsible for the missed opportunity to study cosmic-induced radioisotopes. If an anomalous proton recoil event can be identified within a muon candidate, this yield study can be extended to include βn-emitting decay chains. Fortunately, the muon selection criteria can be refined by exploiting the underlying topology of the cluster. In addition, a more accurate estimation of the candidate's speed naturally arises if the time reconstruction errors are resolved. This could permit for more advanced tracking routines that corrects for variations in momentum along the trajectory. If the muon's kinetic energy is successfully reconstructed, a deeper investigation into atmospheric interactions could be performed. Regardless, this work serves as a foundation for more complicated investigation into cosmic backgrounds at Earth's surface.

Letters of Copyright Permission

SciPris Scientific Publishing and Remittance Integration services

APS physics

Rights and Permissions Request Details

Article Information

Title:	Measurement of the Reactor Antineutrino Flux and Spectrum at Daya Bay
Author:	F. P. An et al. (Daya Bay Collaboration)
Publication:	Physical Review Letters
DOI:	10.1103/PhysRevLett.116.061801
Publisher:	American Physical Society
Date:	15-Sep-2021

Reuse Information

Reuse Category:	Reuse in a thesis/dissertation
Reuse By:	Student
Items for Reuse:	Figures/Tables
Number of figures/tables:	1
Figures and tables description:	figure 2, the Daya Bay inverse beta decay spectrum
Format for Reuse:	Electronic

Reuse Information

Reuse Category:	Reuse in a thesis/dissertation
Reuse By:	Student
Items for Reuse:	Figures/Tables
Number of figures/tables:	1
Figures and tables description:	figure 2, the Daya Bay inverse beta decay spectrum
Format for Reuse:	Electronic

Information about New Publication

Does your reuse require significant modifications of the original content?: No

University/Publisher	University of Waterloo
Title of dissertation/thesis	Statistical Muon Tracking: A Study of Cosmic Backgrounds in the PROSPECT Experiment
Expected completion date	Sep. 2021
Author(s)	Austin Woolverton
Specify intended distribution locations:	United States,Canada

License Requester Information

Name:	Austin Woolverton
Email ID:	adwoolve@uwaterloo.ca
Country:	Canada
Request Id:	RNP/21/SEP/044559

Rights and Permissions request status

Status:	Complete

Please acknowledge the Terms and Conditions to download your license.

CCC | RightsLink®

My Orders | My Library | My Profile | Welcome adwoolve@uwaterloo.ca | Log out | Help | FAQ

My Orders > Orders > All Orders

License Details

This Agreement between Mr. Austin Woolverton ("You") and Elsevier ("Elsevier") consists of your license details and the terms and conditions provided by Elsevier and Copyright Clearance Center.

Print | Copy

License Number	5150440523061
License date	Sep 15, 2021
Licensed Content Publisher	Elsevier
Licensed Content Publication	Nuclear Instruments and Methods in Physics Research Section A: Accelerators, Spectrometers, Detectors and Associated Equipment
Licensed Content Title	The PROSPECT reactor antineutrino experiment
Licensed Content Author	J. Ashenfelter,A.B. Balantekin,C. Baldenegro,H.R. Band,C.D. Bass,D.E. Bergeron,D. Berish,L.J. Bignell,N.S. Bowden,J. Boyle,J. Bricco,J.P. Brodsky,C.D. Bryan,A. Bykadorova Telles,J.J. Cherwinka,T. Classen,K. Commeford,A.J. Conant,A.A. Cox,D. Davee et al.
Licensed Content Date	Apr 1, 2019
Licensed Content Volume	922
Licensed Content Issue	n/a
Licensed Content Pages	23
Type of Use	reuse in a thesis/dissertation
Portion	figures/tables/illustrations
Number of figures/tables/illustrations	3
Format	electronic
Are you the author of this Elsevier article?	No
Will you be translating?	No
Title	Statistical Muon Tracking: A Study of Cosmic Backgrounds in the PROSPECT Experiment
Institution name	University of Waterloo
Expected presentation date	Sep 2021
Portions	Figures 8, 9, and 12
Requestor Location	Mr. Austin Woolverton [redacted] [redacted] Attn: Mr. Austin Woolverton
Publisher Tax ID	GB 494 6272 12
Total	**0.00 CAD**

BACK

Re: permissions for a thesis

Permissions <permissions@ioppublishing.org>
Mon 2021-09-20 3:43 AM
To: Austin David Woolverton
Cc: jinst-eo <jinst-eo@jinst.sissa.it>

Dear Austin,

Thank you for your request to reproduce material published by IOP Publishing *in your thesis,* ***"Statistical Muon Tracking: A study of Cosmic Backgrounds in the PROSPECT Experiment"*** *to be published by* ***University of Waterloo***

Regarding:

- ***Figure 10*** *from* ***"Performance of a segmented 6Li-loaded liquid scintillator detector for the PROSPECT experiment"***

We are happy to grant permission for the use you request on the terms set out below.

License to publish material published by IOP Publishing

Please provide the below to your new publisher as proof of permission.

Conditions

Non-exclusive, non-transferrable, revocable, worldwide, permission to use the material in print and electronic form will be granted **subject to the following conditions:**

- Permission will be cancelled without notice if you fail to fulfil any of the conditions of this letter.
- You will make reasonable efforts to contact the author(s) to seek consent for your intended use. Contacting one author acting expressly as authorised agent for their co-authors is acceptable.
- You will reproduce the following prominently alongside the material:
  - the source of the material, including author, article title, title of journal, volume number, issue number (if relevant), page range (or first page if this is the only information available) and date of first publication. This information can be contained in a footnote or reference note; or
  - a link back to the article (via DOI); and
  - ***if practical and IN ALL CASES for works published under any of the Creative Commons licences the words "© IOP Publishing Ltd and Sissa Medialab. Reproduced by permission of IOP Publishing. All rights reserved"***
- The material will not, without the express permission of the author(s), be used in any way which, in the opinion of IOP Publishing, could distort or alter the author(s)' original intention(s) and meaning, be prejudicial to the honour or reputation of the author(s) and/or imply endorsement by the author(s) and/or IOP Publishing and/or Sissa Medialab.
- Payment of £0 is received in full by IOP Publishing prior to use.

This permission does not apply to any material/figure which is credited to another source in our publication or has been obtained from a third party. Express permission for such materials/figures must be obtained from the copyright owner.

Kind regards,

Sophie
Copyright & Permissions Team
Sophie Brittain - Rights & Permissions Assistant
Cameron Wood - Legal & Rights Adviser
Contact Details
E-mail: permissions@ioppublishing.org

For further information about copyright and how to request permission: https://publishingsupport.iopscience.iop.org/copyright-journals/
See also: https://publishingsupport.iopscience.iop.org/
Please see our Author Rights Policy https://publishingsupport.iopscience.iop.org/author-rights-policies/
Please note: We do not provide signed permission forms as a separate attachment. Please print this email and provide it to your publisher as proof of permission. **Please note**: Any statements made by IOP Publishing to the effect that authors do not need to get permission to use any content where IOP Publishing is not the publisher is not intended to constitute any sort of legal advice. Authors must make their own decisions as to the suitability of the content they are using and whether they require permission for it to be published within their article.

Re: permission to re-use material in a thesis

Permissions <permissions@ioppublishing.org>
Fri 2021-09-24 5:57 AM

To: Austin David Woolverton

Dear Austin,

Thank you for providing confirmation that you have received the consent of the authors to reproduce content from AAS journals:

Regarding:

- ***Figures 9*** *&* ***12*** *from* ***"THE TEMPERATURE EFFECT IN SECONDARY COSMIC RAYS (MUONS) OBSERVED AT THE GROUND: ANALYSIS OF THE GLOBAL MUON DETECTOR NETWORK DATA"***

I am happy to confirm that permission is granted and you need take no further action.

Please include the following alongside the material:

- the source of the material, including author, article title, title of journal, volume number, issue number (if relevant), page range (or first page if this is the only information available) and date of first publication. This material can be contained in a footnote or reference.
- for material being published electronically, a link back to the article (via DOI)
- if practical and IN ALL CASES for works published under any of the Creative Commons licences the words "© AAS. Reproduced with permission".

This permission does not apply to any material/figure which is credited to another source in the AAS publication or has been obtained from a third party. Express permission for such materials/figures must be obtained from the copyright owner.

Kind regards,

Sophie
Copyright & Permissions Team
Sophie Brittain - Rights & Permissions Assistant
Cameron Wood - Legal & Rights Adviser
Contact Details
E-mail: permissions@ioppublishing.org

For further information about copyright and how to request permission: https://publishingsupport.iopscience.iop.org/copyright-journals/
See also: https://publishingsupport.iopscience.iop.org/
Please see our Author Rights Policy https://publishingsupport.iopscience.iop.org/author-rights-policies/
Please note: We do not provide signed permission forms as a separate attachment. Please print this email and provide it to your publisher as proof of permission. **Please note**: Any statements made by IOP Publishing to the effect that authors do not need to get permission to use any content where IOP Publishing is not the publisher is not intended to constitute any sort of legal advice. Authors must make their own decisions as to the suitability of the content they are using and whether they require permission for it to be published within their article.

References

[1] F. An *et al.*, "Measurement of the reactor antineutrino flux and spectrum at Daya Bay," *Physical review letters*, vol. 116, no. 6, Feb. 2016, doi: https://doi.org/10.1103/PhysRevLett.116.061801.

[2] S. H. Seo *et al.*, "Spectral measurement of the electron antineutrino oscillation amplitude and frequency using 500 live days of RENO data," *Physical Review D*, vol. 98, no. 1, May 2018, doi: https://doi.org/10.1103/PhysRevD.98.012002.

[3] D. Adey *et al.*, "Improved measurement of the reactor antineutrino flux at Daya Bay," *Physical Review D.*, vol. 100, no. 5, Sep. 2019, doi: https://doi.org/10.1103/PhysRevD.100.052004.

[4] M. Andriamirado *et al.*, "Improved short-baseline neutrino oscillation search and energy spectrum measurement with the PROSPECT experiment at HFIR," *Physical Review D*, vol. 103, no. 3, Feb. 2021, doi: https://doi.org/10.1103/PhysRevD.103.032001.

[5] R. Rosero, "Pulse shape discriminating ^{6}Li-doped liquid scintillator for the PROSPECT experiment," presented at the April APS 2018, Columbus, Ohio, USA, April 14–17, 2018.

[6] J. Ashenfelter *et al.*, "Performance of a segmented ^{6}Li-loaded liquid scintillator detector for the PROSPECT experiment," *Journal of Instrumentation*, vol. 13, no. 06, June 2018, doi: https://doi.org/10.1088/1748-0221/13/06/P06023.

[7] A. Hansell, "A new measurement of the neuton multiplicity emitted in ^{252}Cf spontaneous fission," Ph.D. dissertation, Dept. Physics, Temple University, Philadelphia, PA, US, 2020, https://prospect.yale.edu/talkspublications/theses.

[8] J. Ashenfelter *et al.*, "The PROSPECT reactor antineutrino experiment," *Nuclear Instruments and Methods in Physics Research Section A: Accelerators, Spectrometers,*

Detectors and Associated Equipment, vol. 922, p. 287–309, April 2019, doi: https://doi.org/10.1016/j.nima.2018.12.079.

[9] D. Groom and S. Klein, "Passage of particles through matter," in *Review of Particle Physics*, P. A. Zyla *et al.* (Particle Data Group), Prog. Theor. Exp. Phys. 2020, pp. 546, doi: https://doi.org/10.1093/ptep/ptaa104.

[10] D. F. Measday, "The nuclear physics of muon capture," *Physics Reports*, vol. 345, no. 4-5, pp. 243–409, Nov. 2001, doi: https://doi.org/10.1016/S0370-1573(01)00012-6.

[11] The University of Adelaide, "Air shower illustration," *School of Chemistry and Physics: High Energy Astrophysics*. Adelaide, Australia, 2005, [Online]. Available: http://www.physics.adelaide.edu.au/astrophysics/hires/uhecr.html, Accessed on: March, 4, 2021.

[12] F. P. An *et al.*, "Seasonal variation of the underground cosmic muon flux observed at Daya Bay," *Journal of Cosmology and Astroparticle Physics*, vol. 2018, no. 1, Jan. 2018, doi: https://doi.org/10.1088/1475-7516/2018/01/001.

[13] ——, "Cosmogenic neutron production at Daya Bay," *Physical Review D - Particles, Fields, Gravitation and Cosmology*, vol. 97, no. 5, March 2018, doi: https://doi.org/10.1103/PhysRevD.97.052009.

[14] H. de Kerret *et al.*, "Yields and production rates of cosmogenic ^{9}Li and ^{8}He measured with the Double Chooz near and far detectors," *Journal of High Energy Physics*, vol. 53, Nov. 2018, doi: https://doi.org/10.1007/JHEP11(2018)053.

[15] W. Yu-Cheng *et al.*, "Measurement of cosmic ray flux in china JinPing underground laboratory," *Chinese Physics C*, vol. 37, no. 8, p. 086001, May 2013, doi: https://doi.org/10.1088/1674-1137/37/1/016001.

[16] D. Jaffe, "Estimate of ^{9}Li background rate in PROSPECT," *PROSPECT Internal Documentation*, July, 2015.

[17] M. Mendenhall, "PROSPECT-G4 workflow tutorial," *PROSPECT Internal Documentation*, July, 2015.

[18] S. Agostinelli *et al.*, "GEANT4-a simulation toolkit," *Nuclear Instruments and Methods in Physics Research Section A: Accelerators, Spectrometers, Detectors and Associated Equipment*, vol. 506, no. 3, pp. 250–303, Feb. 2003, doi: https://doi.org/10.1016/S0168-9002(03)01368-8.

[19] C. Hagmann, D. Lange, and D. Wright, "Cosmic-ray shower generator (CRY) for Monte Carlo transport codes," *IEEE Nuclear Science Symposium Conference Record*, vol. 2, pp. 1143–1146, Nov. 2007, doi: https://doi.org/10.1038/10.1109/NSSMIC.2007.4437209.

[20] R. R. S. Mendonça *et al.*, "The temperature effect in secondary cosmic rays (muons) observed at the ground: Analysis of the global muon detector network data," *The Astrophysical Journal*, vol. 830, no. 2, p. 88, Oct. 2016, doi: https://doi.org/10.3847/0004-637x/830/2/88.

[21] NCEI, "Integrated global radiosonde archive," https://www.ncdc.noaa.gov/data-access/weather-balloon/integrated-global-radiosonde-archive.

[22] O. Kyzylova, "Characterization of time-varying backgrounds in the PROSPECT experiment," Ph.D. dissertation, Dept. Physics, Drexel University, Philadelphia, PA, US, 2021, https://prospect.yale.edu/talkspublications/theses.

[23] P. Torr and A. Zisserman, "MLESAC: A new robust estimator with application to estimating image geometry," *Computer Vision and Image Understanding*, vol. 78, pp. 138–156, April 2000, doi: https://doi.org/10.1006/cviu.1999.0832.

[24] C. Feng and Y. Hung, "A robust method for estimating the fundamental matrix," *Digital Image Computing: Techniques and Applications*, pp. 633–642, Dec. 2003.

[25] Q. Zheng *et al.*, "Development of a 6D Kalman filter for charged particle tracking in time projection chamber without magnetic field," *Radiation Detection Technology and Methods*, vol. 4, no. 1, pp. 70–74, 2020, doi: https://doi.org/10.1007/s41605-019-0151-x.

[26] R. Frühwirth, "Application of Kalman filtering to track and vertex fitting," *Nuclear Instruments and Methods in Physics Research*, vol. 262, no. 2-3, pp. 444–450, Dec. 1987, doi: https://doi.org/10.1016/0168-9002(87)90887-4.

[27] Y. Wang, V. Balic, G. Gratta, A. Fasso, S. Roesler, and A. Ferrari, "Predicting neutron production from cosmic-ray muons," *Physical Review D*, vol. 64, no. 1, June 2001, doi: https://doi.org/10.1103/PhysRevD.64.013012.

[28] V. A. Kudryavtsev, N. J. C. Spooner, and J. E. McMillan, "Simulations of muon-induced neutron flux at large depths underground," *Nuclear Instruments and Methods in Physics*, vol. 505, no. 3, pp. 688–698, June 2003, doi: https://doi.org/10.1016/S0168-9002(03)00983-5.

[29] R. Hertenberger, M. Chen, and B. L. Dougherty, "Muon-induced neutron and pion production in an organic liquid scintillator at a shallow depth," *Physical Review C*, vol. 52, no. 6, pp. 3449–3459, Dec. 1995, doi: https://doi.org/10.1103/PhysRevC.52.3449.

[30] F. Boehm *et al.*, "Neutron production by cosmic-ray muons at shallow depth," *Physical Review D*, vol. 62, no. 9, Nov. 2000, doi: https://doi.org/10.1103/PhysRevD.62.092005.

[31] S. C. Blyth *et al.*, "Measurement of cosmic-ray muons and muon-induced neutrons in the aberdeen tunnel underground laboratory," *Physical Review D*, vol. 93, no. 7, April 2016, doi: https://doi.org/10.1103/PhysRevD.93.072005.

[32] S. Abe *et al.*, "Production of radioactive isotopes through cosmic muon spallation in KamLAND," *Physical Review C*, vol. 81, no. 2, Feb. 2010, doi: https://doi.org/10.1103/PhysRevC.81.025807.

[33] G. Bellini *et al.*, "Cosmogenic backgrounds in Borexino at 3800 m water-equivalent depth," *Journal of Cosmology and Astroparticle Physics*, vol. 8, no. 1, Aug. 2013, doi: https://doi.org/10.1088/1475-7516/2013/08/049.

[34] D. Reyna, "A simple parameterization of the cosmic-ray muon momentum spectra at the surface as a function of zenith angle," June 2000.

[35] J. Smith and N. M. Duller, "Effects of pi meson decay-absorption phenomena on the high-energy mu meson zenithal variation near sea level," *Journal of Geographical Research*, vol. 64, no. 12, Dec. 1956, doi: https://doi.org/10.1029/JZ064i012p02297.

[36] T. Abrahão *et al.*, "Cosmic-muon characterization and annual modulation measurement with Double Chooz detectors," *Journal of Cosmology and Astroparticle Physics*, vol. 2017, no. 2, Feb. 2017, doi: https://doi.org/10.1088/1475-7516/2017/02/017.

[37] E. Bugaev, A. Misaki, V. A. Naumov, T. S. Sinegovskaya, S. Sinegovsky, and N. Takahashi, "Atmospheric muon flux at sea level, underground, and underwater," *Physical Review D*, vol. 58, no. 5, July 1998, doi: https://doi.org/10.1103/PhysRevD.58.054001.

[38] T. K. Gaisser, R. Engel, and E. Resconi, "Cosmic rays in the galaxy," in *Cosmic Rays and Particle Physics*, 1st ed. Cambridge, United Kingdom: Cambridge University Press, 1990.

[39] L. M. Brown, "The idea of the neutrino," *Physics Today*, vol. 31, no. 9, p. 23, Sept 1978, doi: https://doi.org/10.1063/1.2995181.

[40] E. Fermi, "An attempt of a theory of beta radiation (1)," *Zeitschrift für Physik*, vol. 88, no. 1, pp. 161–177, March 1934, doi: https://doi.org/10.1007/BF01351864.

[41] F. Reines and C. L. Cowan, "Detection of the free neutrino," *Physical Review*, vol. 92, no. 1, p. 830–831, Nov. 1953, doi: https://doi.org/10.1103/PhysRev.92.830.

[42] G. Danby *et al.*, "Observation of high-energy neutrino reactions and the existence of two kinds of neutrinos," *Physical Review Letters*, vol. 9, no. 1, p. 36, June 1962, doi: https://doi.org/10.1103/PhysRevLett.9.36.

[43] B. T. Cleveland, T. Daily, R. Davis, J. R. Distel, K. Lande, C. K. Lee, P. S. Wildenhain, and J. Ullman, "Measurement of the solar electron neutrino flux with the homestake chlorine detector," *The Astrophysical Journal*, vol. 496, no. 1, pp. 505–526, March 1998, doi: https://doi.org/10.1086/305343.

[44] Y. Fukuda *et al.*, "Evidence for oscillation of atmospheric neutrinos," *Physical Review Letters*, vol. 81, no. 8, p. 1562, Aug. 1998, doi: https://doi.org/10.1103/PhysRevLett.81.1562.

[45] R. L. Helmer *et al.*, "First results from the sudbury neutrino observatory," *Nuclear Physics B*, vol. 111, no. 1-3, pp. 122–127, Nov 2002, doi: https://doi.org/10.1016/S0920-5632(02)01693-6.

[46] H. D. Kerry *et al.*, "Double Chooz θ_{13} measurement via total neutron capture detection," *Nature Physics*, vol. 16, p. 558–564, April 2020, doi: https://doi.org/10.1038/s41567-020-0831-y.

[47] A. C. Hayes and P. Vogel, "Reactor neutrino spectra," *Annual Review of Nuclear and Particle Science*, vol. 66, no. 1, pp. 219–244, Oct. 2016, doi: https://doi.org/10.1146/annurev-nucl-102115-044826.

[48] T. A. Mueller *et al.*, "Improved predictions of reactor antineutrino spectra," *Physical Review C*, vol. 83, no. 5, May 2011, doi: https://doi.org/10.1103/PhysRevC.83.054615.

[49] P. Huber, "Determination of antineutrino spectra from nuclear reactors," *Physical Review C*, vol. 84, no. 2, Aug. 2012, doi: https://doi.org/10.1103/PhysRevC.84.024617.

[50] B. K. Cogswell, D. J. Ernst, K. T. L. Ufheil, J. T. Gaglione, and J. M. Malave, "Neutrino oscillations: The ILL experiment revisited," *Physical Review D*, vol. 99, no. 5, March 2019, doi: https://doi.org/10.1103/PhysRevD.99.053003.

[51] G. Mention *et al.*, "Reactor antineutrino anomaly," *Physical Review D*, vol. 83, no. 7, April 2011, doi: https://doi.org/10.1103/PhysRevD.83.073006.

[52] P. Vogel, G. K. Schenter, F. M. Mann, and R. E. Schenter, "Reactor antineutrino spectra and their application to antineutrino-induced reactions. II," *Physical Review C*, vol. 24, no. 4, pp. 1543–1553, Oct 1981, doi: https://doi.org/10.1103/PhysRevC.24.1543.

[53] G. Ilas, D. Chandler, B. J. Ade, E. E. Sunny, B. R. Betzler, and D. Pinkston, "Modeling and simulations for the high flux isotope reactor cycle 400," oak Ridge National Lab. (ORNL), Oak Ridge, TN, USA, Rep. 1185903, 2015.

[54] B. R. Martin and G. Shaw, *Particle Physics*, 4th ed. Chichester, West Sussex, United Kingdom: Wiley, 2017.

[55] G. Bardin *et al.*, "A new measurement of the positive muon lifetime," *Physics Letters B*, vol. 137, no. 1-2, pp. 135–140, March 1984, doi: https://doi.org/10.1016/0370-2693(84)91121-3.

[56] A. Czarnecki, M. Dowling, X. G. i Tormo, W. J. Marciano, and R. Szafron, "Michel decay spectrum for a muon bound to a nucleus," *Physical Review D*, vol. 90, Nov. 2014, doi: https://doi.org/10.1103/PhysRevD.90.093002.

[57] A. Czarnecki, X. G. i Tormo, and W. J. Marciano, "Muon decay in orbit: Spectrum of high-energy electrons," *Physical Review D*, vol. 84, July 2011, doi: https://doi.org/10.1103/PhysRevD.84.013006.

[58] T. Luu and C. Hagmann, "Neutron production by muon spallation I: Theory," lawrence Livermore National Lab., Livermore, CA, USA, Rep. 38054998, 2006.

[59] J. von Neumann and R. D. Richtmyer, *Statistical Methods in Neutron Diffusion.* University of California Press, 2020, pp. 17-36. [Online]. Available: https://doi.org/10.1525/9780520322929-004.

[60] X. Zhang, "Energy scale study for PROSPECT's measurement of the antineutrino spectrum of ^{235}U," Ph.D. dissertation, Dept. Physics, Illinois Institute of Technology, Chicago, IL, US, 2019.

[61] B. C. Rastin, "An accurate measurement of the sea-level muon spectrum within the range 4 to 3000 gev/c," *Journal of Physics G: Nuclear Physics*, vol. 10, no. 11, pp. 1609–1628, April 1984, doi: https://doi.org/10.1088/0305-4616/10/11/017.

[62] A. Tang, G. Horton-Smith, V. Kudryavtsev, and A. Tonazzo, "Muon simulations for Super-Kamiokande, KamLAND and CHOOZ," *Physical Review D*, Sept. 2006, doi: https://doi.org/10.1103/PhysRevD.74.053007.

[63] P. H. Barrett, L. M. Bollinger, G. Cocconi, Y. Eisenberg, and K. Greisen, "Interpretation of cosmic-ray measurements far underground," *Review of Modern Physics*, vol. 24, no. 3, p. 133, July 1952, doi: https://doi.org/10.1103/RevModPhys.24.133.

[64] M. S. Gordon *et al.*, "Measurement of the flux and energy spectrum of cosmic-ray induced neutrons on the ground," *IEEE Transactions on Nuclear Science*, vol. 51, pp. 3427–3434, Dec. 2004.

[65] J. B. Birks, "Chapter 8 - organic liquid scintillators," in *The Theory and Practice of Scintillation Counting*, 1st ed. International Series of Monographs in Electronics and Instrumentation, 1964, p. 269 – 320.

[66] K. Pearson, "LIII. on lines and planes of closest fit to systems of points in space," *Philosophical Magazine*, vol. 2, no. 11, p. 559–572, Nov. 1901, doi: https://doi.org/10.1080/14786440109462720.

[67] H. Hotelling, "Analysis of a complex of statistical variables into principal components," *Journal of Educational Philosophy*, vol. 24, no. 7, 1933, doi: https://doi.org/10.1037/h0070888.

[68] E. W. Grashorn *et al.*, "The atmospheric charged kaon/pion ratio using seasonal variation methods," *Astroparticle Physics*, vol. 33, no. 3, p. 140–145, Aug. 2010, doi: https://doi.org/10.1016/j.astropartphys.2009.12.006.

[69] A. N. Dmitrieva, R. P. Kokoulin, A. A. Petrukhin, and D. A. Timashkov, "Corrections for temperature effect for ground-based muon hodoscopes," *Astroparticle Physics*, vol. 34, no. 6, pp. 401–411, Jan. 2006, doi: https://doi.org/10.1016/j.astropartphys.2010.10.013.

[70] T. K. Gaisser *et al.*, "Seasonal variations of high energy cosmic ray muons observed by the IceCube observatory as a probe of kaon/pion ratio," in *Proceedings of* 32^{nd} *International Cosmic Ray Conference(ICRC)*, Beijing, China, Aug. 11-18, 2011, pp. 78–81.

[71] A. Bouchta *et al.*, "Seasonal variation of the muon flux seen by AMANDA," in *Proceedings of the* 26^{th} *International Cosmic Ray Conference*, Salt Lake City, Utah, USA, Aug. 17-25, 1999.

[72] NIST, "ESTAR, Stopping Power and Range Tables for Electrons," https://physics.nist.gov/PhysRefData/Star/Text/ESTAR.html (accessed July 18, 2021).

[73] P. Rousseeuw, "Least median of squares regression," *Journal of the American Statistical Association*, vol. 79, no. 388, p. 871–880, Jan. 1985, doi: https://doi.org/10.1080/01621459.1984.10477105.

[74] C. Croux and A. Ruiz-Gazen, "A fast algorithm for robust principal components based on projection pursuit," in *COMPSTAT*, A. Prat, Ed. Heidelberg: Physica-Verlag HD, 1996, pp. 211–216, doi: https://doi.org/10.1007/978-3-642-46992-3_22.

[75] C. D. Lu, T. Y. Zhang, X. Z. Du, and C. P. Li, "A robust kernel pca algorithm," in *Proceedings of 2004 International Conference on Machine Learning and Cybernetics*, Shanghai, China, Aug. 26-29, 2004, pp. 3084–3087, doi: https://doi.org/10.1109/ICMLC.2004.1378562.

[76] M. Fischler and R. Bolles, "Random sample consensus: a paradigm for model fitting with applications to image analysis and automated cartography," *Communications of the ACM*, vol. 24, no. 6, p. 381–395, June 1981, doi: https://doi.org/10.1145/358669.358692.

[77] R. E. Kalman, "A new approach to linear filtering and prediction problems," *Journal of Basic Engineering*, vol. 82, no. 1, p. 35–45, Mar. 1960, doi: https://doi.org/10.1115/1.3662552.

APPENDICES

Appendix A

Precise Muon Tracking at PROSPECT

Since the PCA routine builds the empirical covariance matrix using the entire data sample, an outlying measurement may have unforeseen and adverse consequences on the track reconstruction. The principal components may be pulled away from the average distribution and distort the results. Robust variations of the PCA routine have been proposed including elliptical trimming [73], projection pursuit [74], and adaptive kernelization techniques [75]. In general, these methods assume that the measurements behave as a multivariate-Gaussian point cloud distribution. Since this is not the case, additional filtering techniques must be introduced.

Outlier purification is a computationally demanding procedure in computer vision and data processing. Furthermore, the definition of an outlier is specific to the problem. In most cases, an outlier is defined as any anomalous or corrupt measurement that does not follow the general trend or underlying model describing the data. With respect to particle tracking, a measurement is considered corrupt or anomalous if it is accidentally clustered together with a proper muon track or if the high-energy limitations of the waveform digitizers resulted in improper event reconstructions.

The current tracking routine at PROSPECT makes little distinction between a corrupt or anomalous measurement. Although an effort to improve the event reconstruction from clipped waveform is currently underway, the two classes of contamination are treated as equivalent. Whether on error occurred in position or in time is relatively meaningless if the general trend in the cluster is extracted from a pure subset.

At PROSPECT, a two stage outlier purification method is used. First, a random sam-

pling approach selects the most probable pure subset from the cluster. This subset is used to generate an initial guess for the tracking parameters. This procedure is computationally demanding and should only be applied in extreme cases. If, however, a track candidate is constructed from a purified sample, a Markovian filtering approach is applied. A 6-dimensional Kalman filter rebuilds the track and assigns the candidate a tracking score. With additional adjustments to the model, this score may be used to isolate statistically meaningful tracks from distorted samples.

A.1 Maximum Likelihood Sampling Consensus

Random sampling consensus (RANSAC) in an iterative approach to outlier detection. First published by Fischler and Bolles in 1981 [76], RANSAC, and its many variations, is a non-deterministic algorithm where the probability that it succeeds increases after each iteration. The smallest sample size m needed to construct the underlying model is uniformly sampled from the set of observations, and the best sample is retained from them. Each sample is awarded a score according to how accurate the sample mimics the model. For the standard RANSAC algorithm, the scoring metric is decided from the residual errors between the model and each measurement within the entire sample.

The score is incremented if the residuals are within a tolerance threshold. This tolerance is model specific and, if set improperly, may limit the performance of the algorithm. The scoring function may accidentally increment if it is set to low. When applied to cluster filtering, it must be wide enough to accept measurement errors and segmentation effects, while also being narrow enough to reject accidentally clustered events. Furthermore, each muon candidate follows a different model. Each candidate has a unique entrance point, speed, and direction; therefore, the tolerance is not unique. Since the break-point occurs at 50% measurement contamination, RANSAC may struggle with candidates that are largely populated with anomalous data.

Variations of RANSAC have been proposed that attempt to resolve these problems; each variation adjusts either the scoring function or sampling strategy. The variation must possess minimal computational overburden and be insensitive to the choice of hyper-parameters. Maximum likelihood sampling consensus (MLESAC) was first proposed by Torr and Zisserman [23] in 1995. It is chosen because it incorporates measurement uncertainties using a probabilistic interpretation of the cluster.

A.1.1 Parameter Estimation

After a model is generated from a randomly sampled subset, MLESAC attempts to maximize the likelihood that each measurement is consistent with the model. If the inlying measurements are assumed to be independent and identically distributed, the underlying probability density function follows a Gaussian mixture model.

$$p(\mathbf{x}_i|\mathbf{r}_0, \mathbf{v}) = \gamma\Big(\frac{1}{\sqrt{2\pi}\sigma}\Big)^d \exp\left\{-\frac{\rho(\mathbf{x}_i|\mathbf{r}_0, \mathbf{v})^2}{2\sigma^2}\right\} + \frac{(1-\gamma)}{v} \tag{A.1}$$

Equation A.1 gives the probability that, given the fit parameters $\mathbf{r}_0$ and $\mathbf{v}$, a particular measurement $\mathbf{x}_i$ agrees with the model. The residuals $\rho(\mathbf{x}_i|\mathbf{r}_0)$ of non-contaminated samples is expected to follow a $d-$dimensional Gaussian distribution with mean 0 and standard deviation σ. The parameter γ is the fraction of uncontaminated events within the cluster. The exponent d represents the number of features in each measurement. In this case, $d = 4$ since pulses includes 3 Cartesian components and 1 time component.

The probability that a measurement is an outlier is assumed to be uniform across the geometrical measurement window v. Unless *a priori* knowledge of the standard deviation σ and inlier ratio γ are known, this is the only hyper-parameter. This parameter is estimated with prior knowledge of the data distribution in order to maximize the number of successfully reconstructed trajectories. The other two parameters are unique to each candidate. In principle, the choice of v is somewhat arbitrary and should not have a major bearing on the results. If, however, the value is set too large, γ will deviate towards 100%.

$$p_{outlier}(\mathbf{x}_i|\mathbf{r}_0, \mathbf{v}) = \frac{1}{v} \tag{A.2}$$

Expectation Maximization (EM), proposed by Torr and Zisserman [23], is used to estimate the inlier ratio γ by iterating over the calculated residuals $\{e_i\}_{i=1}^n$ for that particular trial. Arguably, this usually takes around 4 or 5 iterations [23, 24]. In addition, they argue that ME introduces minimal computational overburden. It, however, relies on an existing estimate of the standard deviation σ. Instead, the method proposed by Feng and Hung is used [24]. This method estimates both σ and γ simultaneously without introducing additional overburden to the MLESAC algorithm.

The algorithm begins by initializing the parameters. The values are set to $\gamma_0 = 1/2$ and $\sigma_0^2 = median\{e_i^2\}/d$. For each residual, the prior probabilities are computed with the current iteration estimate for σ_k and γ_k.

$$p_i = \gamma_k \left(\frac{1}{\sqrt{2\pi}\sigma_k} \right)^d \exp\{-e_i^2/2\sigma_k^2\}, \qquad p_0 = \frac{1-\gamma_k}{v}$$

The final values are calculated using the supports $z_i = \frac{p_i}{p_i+p_0}$ over all n residuals.

$$\gamma_{k+1} = \frac{1}{n}\sum_i^n z_i, \qquad \sigma_{k+1} = \sqrt{\frac{\sum_i^n (z_i \cdot e_i^2)}{n\gamma_{k+1}d}}$$

With the probability density function defined, the scoring function calculates the negative log-likelihood for each sample. The "best" candidate is awarded the lowest score.

$$-L = -\sum_{i=0}^{n} log(p(\mathbf{x}_i|\mathbf{r}_0, \mathbf{v})) \tag{A.3}$$

A.1.2 Time Complexity Considerations

Since the number of muon candidates is large, time complexity must be considered a priory. RANSAC, and its variations, require the validation of all models within a candidate; therefore, it should only be necessary when other filtering methods are incapable of isolating a confirmed muon trajectory.

Additional topological cuts may be implemented to reduce the number of iterations. Since the model is generated using a PCA routine, information about the distribution of points is easily extracted. If the first eigenvalue is smaller than 0.8, than more than 20% of the the total variance is distributed along the other 3 principal components. If this occurs, the chosen subset is likely not in a linear orientation and can be ignored.

Lastly, if the sampling strategy is truly uniform, an escape criterion can be implemented [23, 76]. This escape condition triggers if the probability that a sufficient test track has been identified exceeds a threshold (typically 95%). Unfortunately, if the included number of statistics is low or if $\gamma \to 100\%$, this criterion may accidentally trigger before an appropriate trajectory has been uncovered.

The number of iterations needed to arrive at a sufficient hypothesis is derived from probability theory. Since the inlier ratio γ represents the *a priori* probability that a randomly sampled point is an inlier, and each sampling is an independent Bernoulli trial, the joint probability that k points are inliers is γ^k. The complement probability where

at least one sampled measurement is outlying is $1 - \gamma^k$. If N samples are selected, the probability that at least one sample contains no outliers is easily computed.

$$P_{pure}(\gamma, N) = 1 - (1 - \gamma^k)^N \tag{A.4}$$

This probability can be computed after each iteration. Using the current number of samples and the best estimate for the inlier ratio, RANSAC may terminate if $P_{pure}(\gamma_{best}, n) \geq 0.95$.

Alternatively, since time complexity is under strict considerations, the largest computational speedup is promised if the initial sample size is reduced. Complex filtering methods are not needed if the candidate is false or if it possesses no contamination. Thus, it is recommended that additional topological constraints are introduced in the selection criteria, and the errors introduced by clipped waveforms are resolved.

A.2 The Linear Kalman Filter Method

After a minimal track candidate has been identified, the initial guess is passed through a discrete time Kalman filter. Originally developed as a statistical estimation routine [77], the Kalman filter was first applied to the Apollo projects in the 1960s. Since then, it has been incorporated into various areas of applied physics such as guidance navigation systems, and autonomous robotics. Within the particle physics community, it has been augmented for particle tracking and vertex fitting [26]. Typically utilised to track the behavior of charged particles through magnetic fields in accelerator experiments, a 6-dimensional Kalman filter has been implemented with applications for γ-ray astronomy [25]. Here, the Kalman filter is used for both trajectory fitting and filtering simultaneously.

By updating a series of measurements taken with prior knowledge of the underlying physical dynamics, the Kalman filter better predicts the state dynamics than measurements alone. This is done in an iterative method where an *a priori* state estimate is contrasted against a measurement. In addition, the Kalman filter simultaneously provides a quality score for removing false track candidates or "Ghost Tracks." Furthermore, the Kalman filter is insensitive to anomalous data and missing observations.

The discrete Kalman filter is used if each individual measurement arrives discontinuously. The general principle, however, remains the same across all interpretations of the Kalman filter. The filter alternates between a *prediction* and *update* step in order to converge at a proper estimate of all state vectors.

A.2.1 The Discrete Time Kalman Filter

The prediction step uses the underlying linear model to predict the behavior of the state vector. Furthermore, since the dynamics are governed by Markovian processes, the predicted state depends on all previous predictions and updates. The state dynamics are modeled using the linear state translation matrix $\mathbf{F}_k$, and any stochastic variations in the model are introduced through the model covariance matrix $\mathbf{Q}_k$. Within the prediction step, these operators propagate the current state vector $\mathbf{x}_{k-1|k-1}$, as well as the current state covariance $\mathbf{P}_{k-1|k-1}$, towards the next measurement site.

$$\begin{aligned}\mathbf{x}_{k|k-1} &= \mathbf{F}_k\mathbf{x}_{k-1|k-1}\\ \mathbf{P}_{k|k-1} &= \mathbf{F}_k\mathbf{P}_{k-1|k-1}\mathbf{F}_k^T + \mathbf{Q}_k\end{aligned}$$

During the update step, the k^{th} *a priori* state vector $\mathbf{x}_{k|k-1}$ is contrasted against the k^{th} measurement $\mathbf{z}_k$. The operator $\mathbf{H}_k$ transforms the state vector into the measurement space and the pre-fit residuals are calculated. Using the measurement covariance $\mathbf{R}_k$, the error in the pre-fit residuals is adjusted, and an *a posteriori* state is estimated. The total update procedure is outlined below.

pre-fit residuals:	$\mathbf{y}_{k\|k-1} = \mathbf{z}_k - \mathbf{H}_k\mathbf{x}_{k\|k-1}$
pre-fit residual covariance:	$\mathbf{S}_{k\|k-1} = \mathbf{R}_k + \mathbf{H}_k\mathbf{P}_{k\|k-1}\mathbf{H}_k^T$
Kalman Gain:	$\mathbf{K}_k = \mathbf{P}_{k\|k-1}\mathbf{H}_k^T\mathbf{S}_{k\|k-1}^{-1}$
a postiriori state estimate:	$\mathbf{x}_{k\|k} = \mathbf{x}_{k\|k-1} + \mathbf{K}_k\mathbf{y}_{k\|k-1}$
a postiriori state covariance estimate:	$\mathbf{P}_{k\|k} = (\mathbf{I} - \mathbf{K}_k\mathbf{H}_k)\mathbf{P}_{k\|k-1}$

Additionally, metrics describing the post fit residuals and covariance are extracted. These quantities, listed below, are used in a local χ_k^2 test to remove extreme points. Moreover, a global chi squared value χ_{tot}^2 is accumulated from the local tests. This quality parameter illustrates how well the transition model, including all stochastic and deterministic effects, are reflected in the candidate.

post-fit residuals:	$\mathbf{y}_{k\|k} = \mathbf{z}_k - \mathbf{H}_k\mathbf{x}_{k\|k}$
post-fit residual covariance:	$\mathbf{S}_{k\|k} = \mathbf{R}_k - \mathbf{H}_k\mathbf{P}_{k\|k}\mathbf{H}_k^T$

The alternating updating and predicting procedure is illustrated in figure A.1. Each prediction pushes the state towards the next measurement. If no measurement is available, or if the measurement does not agree with the predicted state, a new prediction is performed.

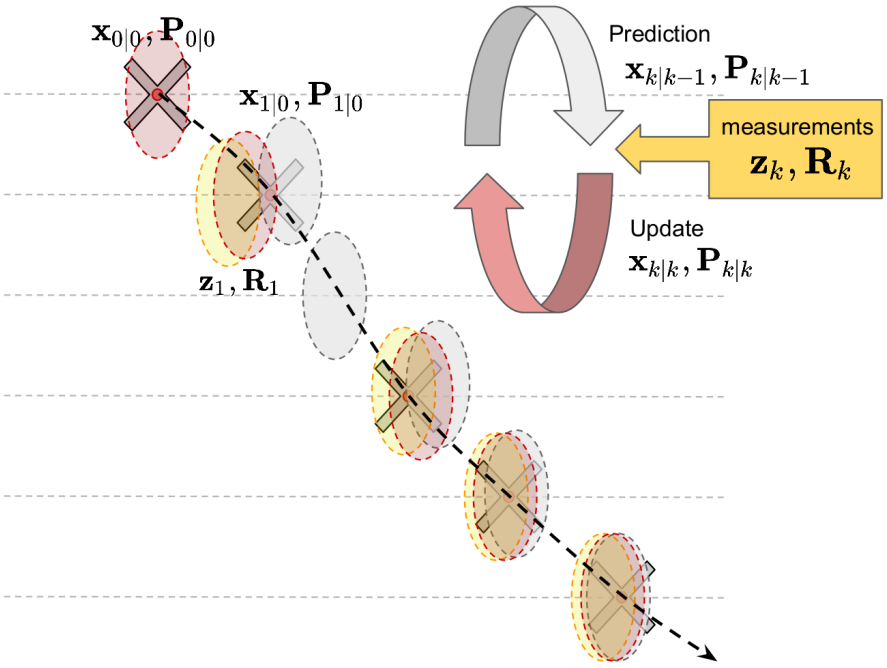

Figure A.1: This diagram illustrates how the Kalman filter alternates between predicting and updating in order to asymptotically converge at a state estimate.

Using the post-fit residuals $\mathbf{y}_{k|k}$ and covariance $\mathbf{S}_{k|k}$, the local chi squared value is the square of the Mahalanobis distance away from the average residual. The Mahalanobis distance, given in equation A.5, represents the distance between two arbitrary points $\vec{x}$ and $\vec{y}$ uncoupled from their covariace $\mathbf{\Sigma}$.

$$MD(\vec{x}, \vec{y}) = \sqrt{(\vec{x} - \vec{y})^T \mathbf{\Sigma}^{-1} (\vec{x} - \vec{y})} \tag{A.5}$$

Since the mean of the residual vector is $\vec{0}$, the chi squared metric can be calculated using the Cholesky decomposition over the post-fit residuals and covariance.

$$\chi^2_k = \mathbf{y}^T_{k|k} \mathbf{S}^{-1}_{k|k} \mathbf{y}_{k|k} \tag{A.6}$$

Since the Kalman filter is mathematically equivalent to a least squares estimate, the accumulated chi squared value also follows a chi squared distribution. If each measurement has m components, and n state updates have been performed, the total degrees of freedom is easily computed.

$$\textit{total degrees of freedom} = m * n - (\textit{the number of free parameters})$$

If the random variables entering the filter have Guassian error, the χ^2 probability may be found by integrating over the cumulative distribution function $f(\chi^2)$. This value may be used to distinguish proper muon trajectories from accidental candidates.

$$P_{\chi^2} = \int_{-\infty}^{\chi^2} f(\tilde{\chi}^2) d\tilde{\chi}^2 \tag{A.7}$$

A.2.2 The 6-Dimensional Model

Following the structure outlined in [25], a six dimensional discrete Kalman filter is implemented for PROSPECT. In this case, the 3-dimensional measurements $\mathbf{z}_k = [x_k, y_k, z_k]^T$ are contrasted against the 6-dimensional state vectors $\mathbf{x}_k = [x_k, y_k, z_k, v_{x_k}, v_{y_k}, v_{z_k}]^T$. Since the measured pulses within each cluster are expected to be time ordered, the state transition matrix propagates the state vector forwards by a small time interval Δt. Moreover, since the arrival time of each pulse is random, the discrete time layer is chosen as the least significant time measurement $\Delta t = 0.1\,\text{ns}$. The state transition and measurement transformation operators are given below.

$$\mathbf{F}_k = \begin{pmatrix} 1 & 0 & 0 & \Delta t & 0 & 0 \\ 0 & 1 & 0 & 0 & \Delta t & 0 \\ 0 & 0 & 1 & 0 & 0 & \Delta t \\ 0 & 0 & 0 & 1 & 0 & 0 \\ 0 & 0 & 0 & 0 & 1 & 0 \\ 0 & 0 & 0 & 0 & 0 & 1 \end{pmatrix}, \qquad \mathbf{H}_k = \begin{pmatrix} 1 & 0 & 0 & 0 & 0 & 0 \\ 0 & 1 & 0 & 0 & 0 & 0 \\ 0 & 0 & 1 & 0 & 0 & 0 \end{pmatrix} \tag{A.8}$$

The initial state $\mathbf{x}_0$ and covariance $\mathbf{P}_0$ is provided using the best trajectory estimate taken from the MLESAC routine. 3 points within the candidate are selected in order to construct the seeded track. These points are usually far from each other and taken in extreme detector regions. Ideally, the test track is constructed using a point near the center of the candidate and from 2 points representing the first and last points in the cluster. The initial state and time are constructed using the PCA routine outlined in section 5.3.

$$\mathbf{x}_0 = \begin{pmatrix} x_0 \\ y_0 \\ z_0 \\ v_{x_0} \\ v_{y_0} \\ v_{z_0} \end{pmatrix}, \qquad \mathbf{P}_0 = \begin{pmatrix} \sigma_x^2 & 0 & 0 & 0 & 0 & 0 \\ 0 & \sigma_y^2 & 0 & 0 & 0 & 0 \\ 0 & 0 & \sigma_z^2 & 0 & 0 & 0 \\ 0 & 0 & 0 & \sigma_{v_x}^2 & 0 & 0 \\ 0 & 0 & 0 & 0 & \sigma_{v_y}^2 & 0 \\ 0 & 0 & 0 & 0 & 0 & \sigma_{v_z}^2 \end{pmatrix} \tag{A.9}$$

The covariance matrix $\mathbf{R}_k$ reflects the systematic error in the measurements. As a result, the matrix is a 3×3 diagonal matrix that reflects the uncertainty in x, y and z. The uncertainty $\sigma_z = 46.46\,\text{mm}$ is chosen using external calibration measurements [4]. Since the measurements are limited by the resolution of the segments in the $XY-$plane, the uncertainties σ_x and σ_y are not necessarily Guassian. In this implementation, however, a smearing is applied to these coordinates to prevent the matrix inversion in the local χ^2 test from failing. Thus σ_x^2 and σ_y^2 are chosen to capture the majority of a Guassian distribution whose width is half that of the segment.

$$3\sigma_x = 3\sigma_y = \frac{w}{2}$$

The post-fit residuals are calculated at each update step, and a local χ^2 with 3 degrees of freedom is performed. If the event is not rejected using the 0.025 quantile local chi squared parameter is recorded. Figure A.2 displays every post-fit residual tabulated in every candidate. The residuals are contrasted between events measured by the PROSPECT detector and the different simulations described in section 4.2. Each candidate passed the previous muon selection criteria and filtering routines. As expected, all three distributions are distributed around the origin. It should be noted that, since the initial trajectory guess was produced from pattern recognition algorithms, the Kalman filter is more likely to generate good fit results. This may explain the symmetry observed in the neutron residuals (blue). Neutrons are not expected to have any meaningful trajectory, yet the Kalman filter selected a random collection of pulses that combinatorically form a line.

Both x and y distributions possess apparently random discontinuous jumps. These jumps, however, appear in both the calibrated measurements and the Monte Carlo data; therefore, an underlying systematic error is distorting the result. This may be the result of poor convergence for small candidates. It is expected that the estimated state vector approaches the true behavior of the particle with asymptotically infinite update steps. In practice, a muon candidate contains between 3 and 30 measured events. These observed features may, however, be removed with additional backwards-propagating smoothing procedures. In addition, a non-symmetric tail is observed in the distribution of y residuals. This may be a result of the limited kinematic model. As implemented, the model assumes that the speed of the muon is constant and does not contain any stochastic variations in the model. Stochastic and deterministic particle physics can be introduced to properly characterise muon energy loss through the scintillator.

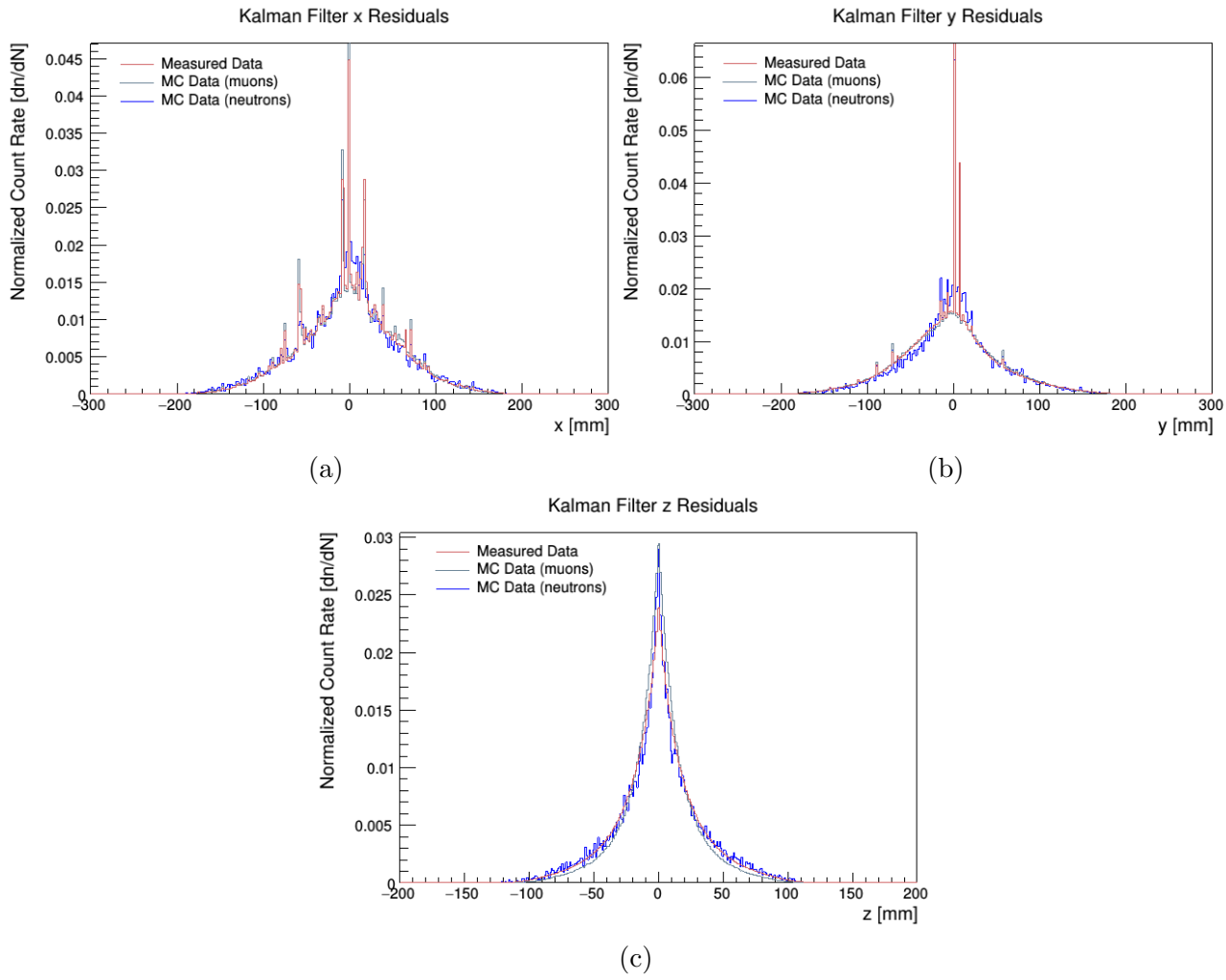

Figure A.2: The distribution of the calculated residuals between each predicted and measured state is computed for all candidates. Calibrated data from early March, 2018 is contrasted against Monte Carlo simulations.

Figure A.3 represents the fit quality for all candidates. Since pattern recognition was used to generate the initial seeded track, it is possible that the results are biased towards good candidates. Regardless an unmodeled effect results in surplus entries observed below $p < 10\%$. This is most likely introduced by ingressed edge events near the PMTs.

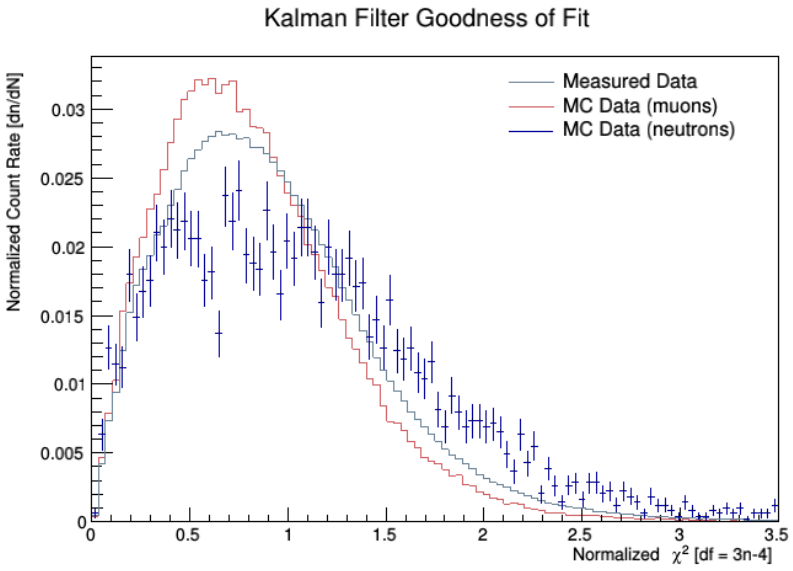

(a)

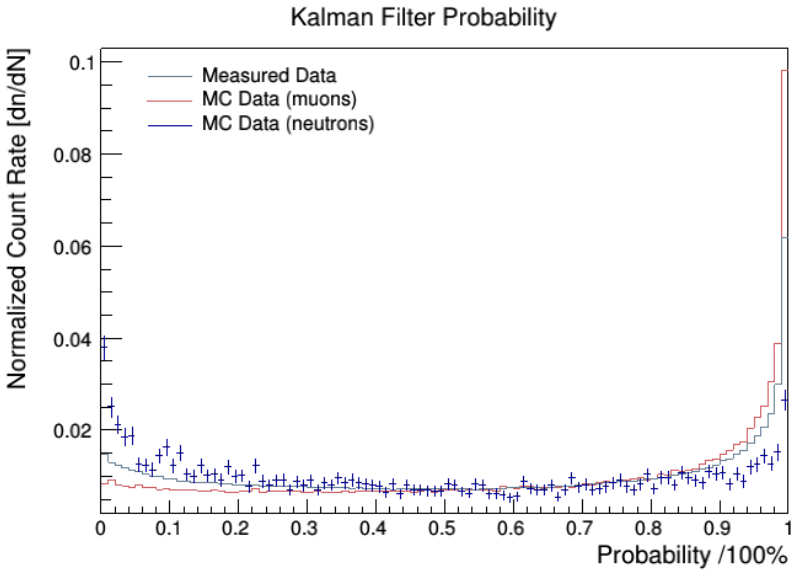

(b)

Figure A.3: The distribution of reduced global χ^2_{tot} values (a) and calculated p-vales (b) are contrasted between different classes of events. The p-values were computed using equation A.7, and the total degrees of freedom are determined from the total number of updates.

A.2.3 Additional Physics Considerations

Data taken from the PROSPECT detector is typically insensitive to stochastic variations due to its segmented design, and the current Kalman filter implementation considers measurement error as the only performance dependent parameter. Regardless, the model noise covariance $\mathbf{Q}_k$ can be constructed to capture random processes such as Coulomb scattering. In this process, the velocity components v_{x_k}, v_{y_k}, and v_{z_k} are expected to deviate with Gaussian probability. The total speed, however, is expected to remain constant.

A six dimensional Kalman filter was developed by Zheng [25]. Their treatment of coulomb scattering was modeled for charged particles in the absence of any external magnetic fields; therefore, their approach may be modified for muon tracking. In the initial theory, proposed by Moliere, the root mean squared (RMS) deviation in the trajectory is expressed in terms of the material thickness traversed by the particle per radiation length x/X_R. The quantity x is calculated by integrating the material density over the traversal length $x = \int_{r_i}^{r_f} \rho dr$. The quantities z, p, and βc represent the charge of the muon as well as its relativistic momentum and speed.

$$\theta_0 = \frac{13.6MeV/c}{\beta pc} z \sqrt{\frac{x}{X_R}} \left(1 + 0.038 \ln\left(\frac{x}{X_R}\right)\right) \tag{A.10}$$

It is assumed that multiple Coulomb scattering only perturbs the direction. Thus, if the speed is constant $\sum_{i=x,y,z} v_i^2 = |\mathbf{v}|^2$, a random vector $\boldsymbol{\omega}_k$ may be introduced to capture this behavior. If the angular deviation follows a quasi-Gaussian distribution with a mean 0 and standard deviation θ_0, the random vector is expressed in accordance with equation A.11. Furthermore, the model covariance matrix $\mathbf{Q}_k \in \mathbb{R}^{6\times 6}$ is calculated using the expectation value of $\boldsymbol{\omega}_k$. It, however, must be recalculated at each prediction step.

$$\boldsymbol{\omega}_k = \begin{pmatrix} 0 \\ 0 \\ 0 \\ \mathcal{N}\left(0, \theta_0 \sqrt{1 - \left(\frac{v_{x_k}}{|\mathbf{v}|}\right)^2}\right) \\ \mathcal{N}\left(0, \theta_0 \sqrt{1 - \left(\frac{v_{y_k}}{|\mathbf{v}|}\right)^2}\right) \\ \mathcal{N}\left(0, \theta_0 \sqrt{1 - \left(\frac{v_{z_k}}{|\mathbf{v}|}\right)^2}\right) \end{pmatrix}, \qquad \mathbf{Q}_k = \begin{pmatrix} 0 & 0 & 0 & 0 & 0 & 0 \\ 0 & 0 & 0 & 0 & 0 & 0 \\ 0 & 0 & 0 & 0 & 0 & 0 \\ 0 & 0 & 0 & \theta_0^2\left(1 - \left(\frac{v_{x_k}}{|\mathbf{v}|}\right)^2\right) & 0 & 0 \\ 0 & 0 & 0 & 0 & \theta_0^2\left(1 - \left(\frac{v_{y_k}}{|\mathbf{v}|}\right)^2\right) & 0 \\ 0 & 0 & 0 & 0 & 0 & \theta_0^2\left(1 - \left(\frac{v_{z_k}}{|\mathbf{v}|}\right)^2\right) \end{pmatrix} \tag{A.11}$$

Furthermore, additional operators can be applied to the state vector $\mathbf{x}_k$ in order to replicate deterministic physical processes. The operator $\mathbf{U}_k \in \mathbb{R}^{6,6}$ for example, may be

introduced to account for the continuous energy loss experienced by the muon through ionization processes. In this case, the total speed is expected to be reduced without perturbing the direction. An energy and momentum dependent quantity μ_k is introduced in order to reduce all three vector components equally.

$$\mathbf{F}_k \rightarrow \mathbf{U}_k \mathbf{F}_k$$

$$\mathbf{U}_k = \begin{pmatrix} 1 & 0 & 0 & 0 & 0 & 0 \\ 0 & 1 & 0 & 0 & 0 & 0 \\ 0 & 0 & 1 & 0 & 0 & 0 \\ 0 & 0 & 0 & \mu_k/m & 0 & 0 \\ 0 & 0 & 0 & 0 & \mu_k/m & 0 \\ 0 & 0 & 0 & 0 & 0 & \mu_k/m \end{pmatrix}$$

The diagonal elements μ_k/m represent the fractional loss in momentum between measurement sites divided by the muon mass $m = 105.7\,\mathrm{MeV/c^2}$. If the initial kinetic energy of the particle is known, this quantity can be determined using the amount of energy lost through ionization. The mean energy loss per unit length $\langle dE/dx \rangle$ can be interpreted using the Bethe-Bloch equation.

The average energy loss is calculated using equation 3.1. If both the density of the material ρ and the particle's traversal length l are known, the total energy loss from deterministic processes ΔE is easily calculated. If the initial energy and momentum are known, the fractional momentum loss μ_k can be calculated.

$$\mu_k = \frac{\sqrt{(E_0 - \Delta E)^2 - m_\mu^2}}{p_0} \tag{A.13}$$

Here, E_0 denotes the initial kinetic energy of the incident particle. Alternatively, it may be redefined to mean the kinetic energy of the particle at the last update step. The fractional energy lost at each measurement layer is given in equation A.14.

$$\Delta E = \left\langle \frac{dE}{dx} \right\rangle \rho l \tag{A.14}$$

Appendix B

Cosmic Backgrounds through the Reactor Cooling Pool

During reactor-off periods, the technicians at the HFIR facility performed scheduled maintenance routines. These maintenance procedures would take 3 days to complete. During this time, the water level in the reactor cooling pool was reduced from it's original height of 3 m above the experiment floor to approximately 2 m below it. Consequentially, the potential increase in IBD-like background events introduced into the PROSPECT experiment must be addressed.

If additional background events were introduced during the maintenance routines, a more complected background subtraction method would be necessary for the neutrino spectrum and oscillation study. The background scaling procedure, briefly introduced in section 2.4, assumes that all background events identified during a reactor-off interval scale equally with both time and pressure. If this is true, the background events are scaled to match the exposure time of events identified during reactor-on periods, and the two rates are subtracted. Ideally, the remainder is the desired IBD spectrum.

To address if the reduced water level affects the background scaling, two analyses where performed. The first investigated muon spallation secondaries and fast neutrons from inelastic scattering on carbon during periods when the water level was reduced. The rate of single capture events and fast neutrons was measured and compared against pressure scaling. This analysis, described in [22], found no significant increase in the background rate. The second analysis is described in this section. The rate of muons through the reactor pool was measured when the water level was full and compared to the muon rate when the water level was reduced.

B.1 Predicted Angular Phase-Space

The muon rate was expected to slightly increase when the water level in the HFIR pool is reduced. Muons that traverse the empty water pool are less likely to decay before depositing energy in the detector. Using the geometry of the HFIR experiment floor, the range of angles that contribute to the increased muon flux was easily calculated. The measured phase-space was compared to the predicted range.

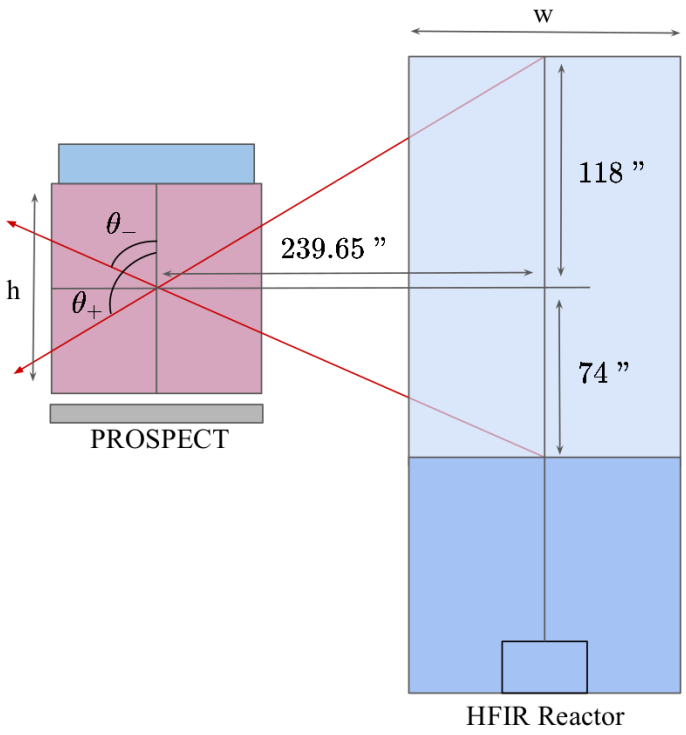

Figure B.1: A diagram of the PROSPECT active volume in relation to the water cooling pool is displayed. The dimensions are used to calculate the trajectory phase space of interest.

Using the detector's proximity to the reactor, the angular phase-space of interest was determined. The geometric measurements, illustrated in figure B.1, determine the minimum and maximum fill line below and above the experiment's central axis. Muons that traverse the vacant space in the water pool were expected to have reconstructed trajectory parameters centered at $\phi = 0$ and between θ_- and θ_+.

The phase-space of interest, in radians, is presented in equation B.1. This prediction, however, assumes that the muon traveled through the central axis of the water pool.

$$\begin{aligned} -\pi/4 \leq \phi \leq \pi/4 \\ 1.27 \pm 0.18 \leq \theta \leq 2.03 \pm 0.21 \end{aligned} \tag{B.1}$$

This introduces the uncertainty in the predicted zenith range. An incident muon may traverse the leading edge of the cooling pool before depositing energy near the bottom edge of the active volume. The uncertainties in the predicted range is half the width of the water pool $\delta x = w/2$ and half the height of the detector $\delta y = h/2$. The uncertainty was calculated using equation B.2.

$$\delta\theta = \sqrt{\left(\frac{y}{y^2+x^2}\right)^2 \delta x^2 + \left(\frac{x}{y^2+x^2}\right)^2 \delta y^2} \tag{B.2}$$

B.2 Tomographic Image of the HFIR Pool

A low resolution image of the water pool was taken by comparing the difference in muon rate. The muon rate when the water level was full was subtracted from the rate measured when it was reduced. This section describes the subtraction method before presenting the statistical significance introduced by the water deficit.

B.2.1 Muon Rate Subtraction Method

Since the water pump schedule was recorded, periods when the water level was reduced were easily identified. The muon rate when the water level was full $r_{i,j}^{high}$ was compared to the rate when the water level was reduced $r_{i,j}^{low}$. The indices i and j correspond to the tracking parameters ϕ and θ respectively. The muon rates were, therefore, compared across all possible angles between $0 \leq \theta \leq \pi$ and $-\pi \leq \phi \leq \pi$. A detailed discussion of the tracking geometry is given in section 5.2.

$$n_{i,j} = \left(\frac{r_{i,j}^{low} - r_{i,j}^{high}}{r_{i,j}^{high}}\right) \times 100\% \tag{B.3a}$$

$$\sigma_{n_{i,j}} = \frac{r_{i,j}^{low}}{r_{i,j}^{high}} \left(\left(\frac{\sigma_{i,j}^{low}}{r_{i,j}^{low}} \right)^2 + \left(\frac{\sigma_{i,j}^{high}}{r_{i,j}^{high}} \right)^2 \right)^{1/2} \times 100\% \tag{B.3b}$$

To determine the statistical significance of the subtraction, the muon rates were scaled by the bin area and the difference was scaled by the uncertainty. The percent difference is given in equation B.3a, and the uncertainty was determined using equation B.3b.

B.2.2 Results and Discussions

The statistical significance of the muon rate difference was calculated across all angular bins, and the results are displayed in figure B.2. The central bright region indicates an increase in the muon rate by approximately $30\sigma_{n_{i,j}}$. This region, consistent with the predicted water pool phase-space, is the only region that changed significantly. During time intervals when the water level is full, the total muon rate decreased by approximately 0.8%. The increase in muon rate caused by the reduction in the water level is, therefore, not significant to the overall background rate.

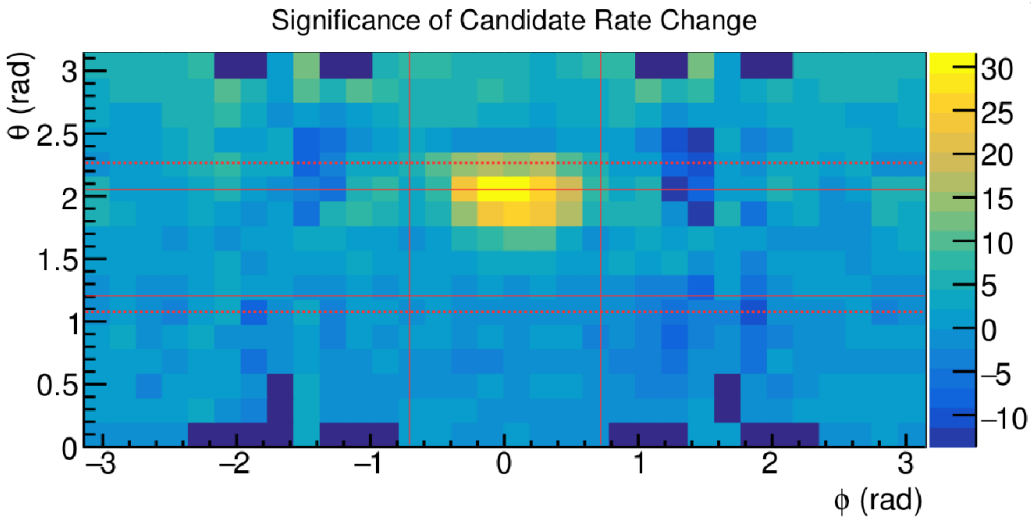

Figure B.2: The statistical significance of the muon rate difference, measured during periods of high and low water levels, is plotted across all possible angles. The bright region represents the water level deficit, and the red lines indicate the predicted muon trajectories through the HFIR cooling pool. The uncertainty is depicted by the dashed lines

The segmentation artifacts at $\phi = \pm\pi/2$ are less apparent during periods when the water level is reduced; therefore, there are more false muon candidates when the water pool is full. Furthermore, the flux of upward traveling muons is negligible; therefore, only the top half of the water pool is observed.

This analysis was, however, performed with an older tracking program then the one presented in section 5. During this study, the constraints on PSD were fixed between 0.125 and 0.14 which lead to a non-physical variation in the muon rate. This motivated investigations into advanced tracking methods and variations in the muon rate from atmospheric effects. Both of these investigations are describe in this thesis.